UNIVERSITÀ DEGLI STUDI DI MESSINA

TESI DI DOTTORATO DI RICERCA IN BIOLOGIA APPLICATA

E MEDICINA SPERIMENTALE

CURRICULUM IN BIOLOGIA APPLICATA

XXIX CICLO

SSD BIO/19

Phage Display as a Tool for Theranostic and Nanomedicine Application

Candidato:

DOTT. DOMENICO FRANCO

Relatore:

Ch.mo Prof.

SALVATORE PIETRO PAOLO GUGLIELMINO

Coordinatore:

Ch.mo Prof.

SALVATORE CUZZOCREA

ANNO ACCADEMICO 2014-2016

ABSTRACT

Theranostic nanomedicine allows co-development of different nanotechnology-based diagnostic and therapy strategies in order to combine detection, diagnosis, and treatment of disease into a single unit. Usually, constructs of multifunctional systems for theranostics include a selective probe both as diagnostic tool and as selective agent for targeted therapy.

In the present work, several proofs of concept of diagnostic and teranostic systems, based on the phage display technology, are presented. In particular, the phage display has been used for the selection of peptides specific to bacterial and tumor cellular targets.

First, phage display technology has been employed to select phage clones, expressing peptides able to bind molecular targets of pathogenic bacteria and cancer cells. Then, the whole phage structure as "biomaterial" has been evaluated with fluorchromes, beads, noble metal nanoparticles and PHA microspheres for the development of multifunctional systems for theranostics. The proofs of concept have been developed using both conventional detection methodologies (agglutination, fluorescence microscopy, PCR, and ELISA) and new optical methods, such as Raman spectrometry and SERS-Raman, which have been carefully considered in the development of some of the described methodologies.

The technical combinations and the obtained results here presented demonstrated the importance of intersections among different fields of theoretical and applied science and the need of a common language among different professionals and research teams.

INDEX

INTRODUCTION

The problem of public health expenditure and the proper allocation of economic resources is one of the main Europe's problems. The need to ensure economic and financial sustainability of public health systems is due to the increase in life expectancy that requires treatment for prolonged and continuous periods. According to Farma-factoring Foundation estimations, between 2008 and 2016, health expenditure in Italy has substantially declined in recent years (Atella and Cincotti)

In this context, research is moving to the development of diagnostic and therapy tools, at low cost and highly efficient.

Basic approach of conventional therapies is to remove diseased cells faster than healthy cells. Moreover, traditional diagnosis procedures are usually used to examine only the current disease status (discriminating between normal and disease state) and rarely give information on disease progression and therapeutic response. In this scenario, the therapeutic effects can be brought out only after an extended therapeutic treatment, with a significant delay in the implementation of a truly effective therapy and unnecessary patient exposure to serious side effects.

The rationale arose from the fact that diseases are heterogeneous, and all existing treatments are effective for only limited patient subpopulations and at selective stages of disease development (Xie *et al,* 2010).

Nanomedicine takes care of nanotechnology applications to medicine, through a conventional biochemical approach. In contrast to conventional therapies, nanomedicine attempts to use sophisticated approaches to either kill specific cells or repair them one cell by using a biosensor to detect, for example, when a drug should be released (Riehemann *et al*, 2009).

This approach has opened new opportunities in therapeutic and diagnostic fields, and new concepts as ***personalised medicine, pharmacogenetics and point-of-care*** testing have been introduced.

In recent years, there is a growing interest towards the development of ***personalized medicine***, which is defined as: “the concept which marks the expected reform in medicine that is projected to arrive at the clinic in coming decades, harnessing genomics and proteomics technologies for tailoring the most suitable pharmacotherapy for each patient; based on individual profiling, it is also projected to allow improved treatment efficacies for many diseases” (Gurwitz and Livshits, 2006). ***Pharmacogenetics*** deals with the study of variability in drug response due to heredity (Nebert, 1999). Variation within the human genome is seen about every 500±1000 bases (Roses, 2010). Although there are a number of different types of polymorphic markers, most attention recently has focused on single nucleotide polymorphisms (SNPs), and the potential for using these to determine the individual drug response profile. Since SNPs occur at a frequency of 1% or greater in the population, theoretically, this could be used to create individual SNP profiles that correlate with individual drug response (Gray *et al,* 2000). It may be possible to tailor drug prescription and drug dosage to the individual, thereby maximizing efficacy and minimizing toxicity (Roses, 2000; Wolf *et al*, 2000; Meyer, 2000). The promise of personalized medicines is also of obvious interest and importance to the pharmaceutical industry since it may allow streamlining of the drug development, drug testing and drug registration process, reducing the time from chemical synthesis to introduction into clinical practice, and therefore the cost of the drug development process (Roses, 2000).

On a technical level, broad implementation of many aspects of *personalized medicine* will require the introduction of a new class of inexpensive diagnostic instruments that do not require time-consuming sample preparation. Ideally, such instruments could be operated in a doctor's office by unskilled personnel.

Point-of-care testing (**POCT**) is an immediate, convenient, and easy-to-use medical diagnostic testing at or near the time and place of patient care (Nichols, 2003). Rapid diagnostic information permits immediate clinical management decisions to be made that will improve patient safety and clinical outcomes. Major benefits are obtained when the output of a POCT device is made available immediately within an electronic medical record. Results can be shared instantaneously with all members of the medical team through the software interface enhancing communication by decreasing turn around time (TAT). A reduction in morbidity and mortality has been associated with goal-directed therapy (GDT) techniques when used in conjunction with POCT and the electronic medical record (Rossi and Khan, 2004). POCT has become established worldwide and finds vital roles in public health (Tran and Kost, 2006).

New diagnostic systems, such as Lab-on-a-chip (LOC), can integrate multiple functions in a single miniaturized chip and allow to carry out medical diagnostic testing near the point of patient care (Nichols, 2003). Excluding economic benefits by system miniaturization, rapid diagnostic information allows immediate clinical management decisions to be made that will improve patient safety and clinical outcomes.

Nanotechnology allows combinations and co-development of different diagnostic and therapy strategies in order to obtain into single agent detection, diagnosis, and treatment of disease, principle on which is based the concept of ***theranostic nanomedicine***.

Possible constructs of multifunctional systems for theranostics include a **selective probe both as diagnostic tool and as target agent for therapy.**

In the present thesis, several proofs of concept of diagnostic and teranostic systems, based on the phage display technology, are presented. In particular, the phage display has been used for the selection of peptides specific to bacterial and tumor cellular targets, using the whole phage structure as "biomaterial" for the correct exposure of these peptides.

In such a way, biosensing and diagnostic systems, with low cost of production, more efficient and much more stable than conventional systems based on antibodies or purified peptides, have been obtained.

Simultaneously, the use of the whole phage structure allowed building metal nanoparticles-phages stable networks for use in both diagnostic and therapeutic fields.

Finally some preliminary data on a potential drug targeting system, aimed to convey and concentrate the encapsulated drug at the target site, are presented. The system is based on a complex between a biopolymer as carrier for controlled drug delivery and a phage expressing specific and selective peptide for the target of interest.

The proofs of concept have been developed using both conventional detection methodologies (agglutination, fluorescence microscopy, PCR, and ELISA) and new optical methods, such as Raman spectrometry and SERS-Raman, which have been carefully considered in the development of some of the described methodologies.

Bibliography

Atella V, Cincotti F. I conti della sanità in Italia: consuntivi e prospettive future. 2015. Quaderni della Fondazione Farmafactoring, n. 3/15.

Gray IC, Campbell DA, Spurr NK. Single nucleotide polymorphisms as tools in human genetics. 2000. Hum Mol Genet. 9, 2403–08

Gurwitz D, Livshits G. Personalized medicine Europe: health, genes and society: Tel-Aviv University, Tel-Aviv, Israel, June 19-21, 2005. 2006. Eur J Hum Genet. 14, 376-80.

Meyer UA. Pharmacogenetics and adverse drug reactions. 2000. Lancet. 356, 1667–71.

Nebert DW. Pharmacogenetics and pharmacogenomics: why is this relevant to the clinical geneticist? 1999. Clin. Genet. 56 247-58.

Nichols J. Point of Care Testing – Performance Improvement and Evidence Based Outcomes. 2003. CRC Press.

Riehemann K, Schneider SW, Luger TA, GodinB, Ferrari M, Fuchs H. Nanomedicine-Challenge and Perspectives. 2009. Angew. Chem. Int. Ed., 48, 872 – 97.

Roses AD. Pharmacogenetics and the practice of medicine. 2000. Nature 405, 857-65.

Wolf CR, Smith G, Smith RL. Science, medicine, and the future: Pharmacogenetics. 2000. Br Med J. 320, 987–90.

Rossi AF, Khan D . Point of care testing: improving pediatric outcomes. 2004. Clin. Biochem. 37, 456–61.

Tran NK, Kost GJ. Worldwide point-of-care testing: compendiums of POCT for mobile, emergency, critical, and primary care and of infectious diseases tests. 2006. Point of Care: the Journal of Near-Patient Testing & Technology. 5, 84–92.

Xie J, Lee S, Chen X. Nanoparticle-based theranostic agents. 2010. Adv Drug Deliv Rev. 62(11), 1064–79.

CHAPTER 1
Probes selection by Phage Display

Introduction

A molecular repertoire is a collection of several molecular variants of peptide or protein structures, from which it can select specific ligands against molecular targets of interest. One of the methods most commonly used in the construction of molecular repertoire is based on the use of filamentous phages that infect *Escherichia coli*, able to display amino acid sequences in a "tolerant" region of its capsid proteins. This experimental technology, called "phage display", offers the advantage to associate in the same phage particle the phenotype, represented by the protein / peptide exposed on the viral surface, to a specific genotype, that is included in the phage genome. So this technology allow to exploring, efficiently selecting and rapidly structure characterizing of very large repertoires of biological molecules by the construction of "encoded" pools (Smith, 1985; Parmley and Smith, 1988). In the mid-1980s, Dr. George Smith of the University of Missouri highlighted the link between capsid proteins expression and nucleic acid encapsulated in M13 filamentous bacteriophage. Particularly, foreign DNA, inserted into upstream of the gene for one of viral coat proteins (pIII), produced phage particles that “displayed” the protein encoded by the foreign DNA at the amino terminal portion of that coat protein (Smith, 1985). The ability to use bacteriophage as tools for the display of ligands became clearer over the next several years, after developing of methodology for fusing larger molecules, such as antibody fragments, to pIII (McCafferty *et al*, 1990; Barbas *et al*, 1991). Nowadays Phage Display has established itself as a powerful biological tool for rapid and inexpensive identification of novel ligands (e.g. receptor agonists) or mapping the interactions between two known proteins (e.g. antibody epitope mapping). In fact antibodies, enzymes, signal transduction proteins, cell surface receptors and structures, and also non-protein targets, such as carbohydrates, polymers or other surface materials, have all been successfully utilized as targets in screening experiments, and have allowed the isolation of specific molecules (Smith and Petrenko,1997; Petrenko and Sorokulova, 2004).

Phage display technology is based on the insertion of foreign nucleotide sequences into genes encoding for various bacteriophage coat proteins, resulting in heterogeneous mixtures of phages, each carrying a distinct peptide sequence (encoded by the corresponding nucleotide insert) as fusion to the coat protein. The physical link between a displayed fusion protein and the DNA encoding for it, represented by the bacteriophage particle, makes specific phage clones selectable and easily identifiable. The strength of the phage display approach results from the powerful combination of affinity selection and biological amplification. Libraries can be affinity selected with a ligate in small reaction volumes (i.e. at high concentration), so that a vast number of foreign peptides, displayed on the surface of the bacteriophage particles, can be surveyed at once for their ability to interact with a given target.

The phage particle is a thin and cylindrical shape, of size about 900 nm x 9 nm, containing a single-stranded DNA genome (6,407 base pairs) which encodes 11 genes, five of which are coat proteins. The major coat protein is the gene 8 protein (g8p), present in 2,700 copies and responsible of the phage DNA encapsulation **(Figure 1.1).** The distal end of the phage particle is capped by five copies each of gene 7 protein (g7p) and gene 9 protein (g9p). At the proximal end, four to five copies each of g6p and g3p are present. M13 bacteriophage infects male bacteria, i.e. which bear the F-plasmid, encoding for the F-pilus. Infection is mediated by the interaction between viral g3p and the F-pilus, and does not cause lysis of host cell. In fact, respect to the lytic phages T4 and T7, filamentous phages are able to replicate and are released from the cell membrane, allowing to the host cell continues to continue to grow and divide. This greatly simplifies the intermediate phage purification steps between rounds of panning, as a simple PEG precipitation step is sufficient to separate the phage from almost all contaminating cellular proteins.

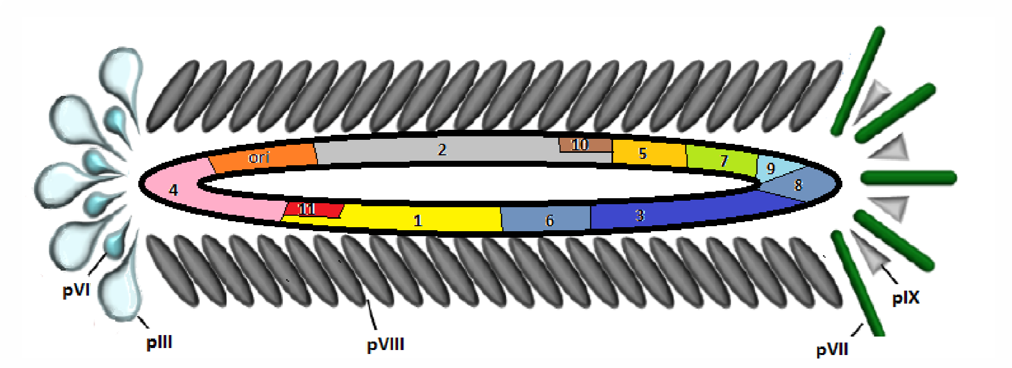

Figure 1.1 M13 phage structure.
Phage genome consists in single-stranded DNA of 6,407 base pairs which encodes 11 genes. Products of genes 1, 4 and 11 are used for genome assembling in phage capsid; genes 2 and 10 encode for a DNA endonuclease for double-stranded replicative form and DNA replication single-stranded circle; gene 5 encodes for a single-stranded DNA-binding protein; finally genes 3, 6, 7, 8 and 9 encode for capsid proteins.

Filamentous phage display systems are generally based on N-terminal fusions to the coat proteins pIII or pVIII. pIII is present at 5 copies per virion, of which all 5 can be fused to short peptides without interfering with phage infectivity. The major coat protein pVIII is present at ~2700 copies per virion, of which ~10% can be reliably fused to peptides or proteins. As a result, peptides expressed as pIII fusions are present at low valence (1-5 copies per virion), while pVIII fusions are present at high valence (~200 copies per virion). In this last case, highly multivalent display libraries can be produced by generating fusions to pVIII, usually achieved via two-gene systems that result in phage particles displaying a mixture of wild-type and recombinant proteins (Felici *et al*, 1991). The increased avidity effect of high valency pVIII display permits selection of very low affinity ligands (such as mimic and bioactive peptides), while low valency pIII display limits selection to higher affinity ligands.

The success of phage derived peptides essentially depends on the quality of the library screened.

Phage-display systems can be distinguished according to the arrangement of the coat protein genes (**Figure 1.2**; Smith, 1993; McConnell 1994).

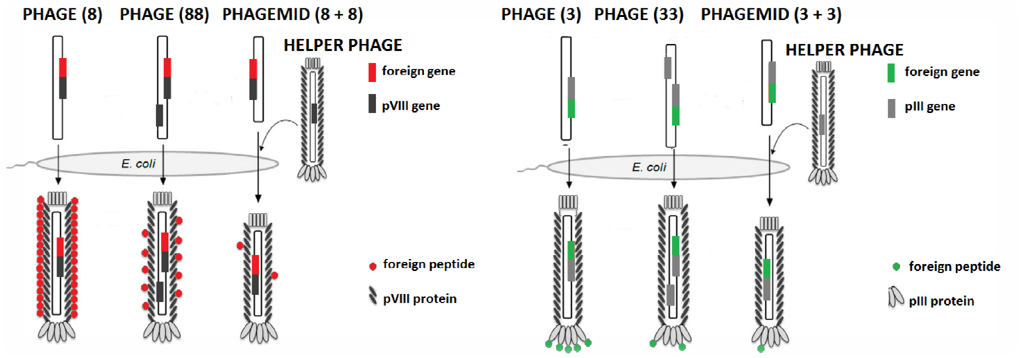

Figure 1.2 Types of phage display systems.
The line inside each virion represents the single-stranded viral DNA, the segments encoding coat proteins pVIII and pIII being designated by black and grey boxes, respectively, while red and green boxes represent foreign coding sequences spliced into a coat-protein gene. Foreign peptides displayed on pIII (green circles) are either appended to the N-terminal domain (type 3 systems) or replace the N-terminal domain (type 3+3 and most type 33 systems). In type 8 systems, the foreign peptide (red circles) is displayed on all copies of the major coat protein pVIII (2700 copies in wild-type virions), whereas in type 88 and 8+8 systems, only a minority of the pVIII copies display the foreign peptide.

In a "type 3" vector, there is a single phage chromosome, with a single gene III which accepts foreign DNA inserts and encodes for a single type of pIII peptide. Therefore, the foreign peptide is theoretically displayed on all five pIII molecules on a virion. Similarly, type 8 vectors display foreign peptides on every copy of pVIII.

Although only short foreign peptides can be displayed on every copy of pVIII, they comprise a substantial fraction of the virion's mass and can dramatically alter its physical and biological properties (Kishchenko *et al*, 1991; 1994)

Differently by type 8 vector, in a type 88 vector the phage genome bears two genes VIII, encoding two different types of pVIII molecule: one is ordinarily recombinant (i.e., bears a foreign DNA insert) and the other wild-type. The resulting virion is a mosaic of both wild-type and recombinant pVIII molecules. These vectors allow hybrid pVIII proteins with quite large foreign peptides to be displayed, since phage assembly is made possible by wild-type pVIII molecules that is the former predominating. The same property applies to a type 33 vector.

Finally, a type 8+8 system consists the two VIII genes are on several genomes, in wild-type phage, called "helper" phage, and in a special kind of plasmid, called "phagemid" (Mead *et al*, 1998; Cesareni *et al*, 1988). Phagemid carries a plasmid replication origin that allows it to replicate normally in an E. coli host, an antibiotic resistance gene for its selection and that allows a filamentous phage replication origin, which is inactive until the cell is infected with the helper phage.

By phagemid vectors, it is possible to achieve a large number of transformants (until 10^{10} clones), creating highly diverse libraries with increased size and improved performance (Ponsel *et al*, 2011). Libraries of short peptides of random sequence have been displayed on phage, and screened by antibodies or other molecules, leading to the identification of new ligands (Zwick *et al*, 1998; Rodi and Makowski, 1999; Deroo and Muller, 2001).

Ligands selected from phage-displayed random peptide libraries can be directed toward biologically relevant sites on the surface of the target protein. Consequently, they can modulate the target protein's activity, acting as delivery and targeting systems in drug design.

Selection consists of culling an initial population of phage-borne peptides to give a subpopulation with increased "fitness" according to some user-defined criterion. Generally, the input to the first round of selection consists in a very large library (10^9 clones), while a selected subpopulation, against a molecular target, is represented by a little fraction of the initial population. A subpopulation consists in a mixture of several phage clones, each with a specific affinity against the target that can be "amplified" by infecting fresh bacterial host cells, so that each individual phage clone in the subpopulation is represented by millions of copies in the amplified stock. The amplified population can then be subjected to further rounds of selection (perhaps accompanied by mutagenesis) to obtain a phage clones population with high stringency and yield, the most important parameter to enhance the efficacy of selection.

Stringency is the degree to which peptides with higher fitness are favored over peptides with lower fitness; yield is the fraction of particles with a given fitness that survive selection. The ultimate goal of selection is usually to isolate peptides with high fitness, but this does not mean that stringency should be increased without bound, since increasing stringency usually entails decreased yield. High yield of the fittest clones is of paramount importance in the very first round of selection, whose input consists of all clones in a very large initial library.

In this section, phage display technology is employed as a tool for the selection of peptides able to bind molecular targets of pathogenic bacteria and cancer cells. Moreover, it is presented a new approach for biomarkers discovery in neurodegenerative diseases by Phage Display technology. Regardless of the molecular target of interest, selection of ligands involves the sequential enrichment of specific binding phage from a large excess of nonbinding clones. This result is accomplished by multiple rounds of phage library "panning", comprising incubation with molecular target, washing to remove nonspecific phage, elution to retrieve specific binding phage, and reinfection and propagation in *Escherichia coli*. Generally three to four rounds of panning are required to enrich for specific binders.

A more detailed discussion about selections made is presented in materials and methods following subsections.

Selection of phage peptides targeting bacterial membrane receptors

Rapid, selective and sensitive detection technologies for pathogenic bacteria are critical in clinical diagnosis and disease control.

Actually, immunoselection methods based on the use of antibodies or synthetic peptides are commonly used for detection of viruses and different bacterial species in various research fields including clinical diagnosis. However, in both cases, there are some disadvantages like their sensivity to physico-chemical variations of environment such as pH, temperature, mechanical stresses and organic solvent and their extremely high production and purification costs. M13 bacteriophage, engineered to express specific and selective peptides on its capsid proteins, can be used as a good substitute for antibodies in recognition of specific targets. The viral mass consists mainly of about 2700 copies of its major coat protein pVIII, about 50% of which are engineered to display selective and specific target-binding peptides. They are easy to produce in large quantities at a relatively low cost, as their propagation on host bacterial cells is cheaper compared to both antibodies and peptides production. Furthermore, phages are structurally robust, and have a strong resistance to pH, and denaturing compounds such as urea, alcohols and other organic solvents, and events stretching (elongation) and bending without losing bacterial infectivity and/or binding capability (Petrenko and Smith, 2000; Petrenko and Vodyanoy, 2003). Bacteriophage can represent suitable surrogates of antibodies or synthethic peptides, possessing distinct advantages while achieving equivalent specificity and sensitivity (Petrenko and Vodyanoy, 2003). This section describes the selection techniques for phage clones displaying peptides capable of specific and strong binding to the cell surface of microorganisms. Particularly, the following describes the procedures for phage clones selection against *Staphylococcus epidermidis* and *Staphylococcus aureus.*

Materials and Methods

Bacteria and growth media. *S. epidermidis* ATCC 12228 and *S. aureus* ATCC 29213 obtained from the American Type Culture Collection (ATCC, LGC Promochem, Milan, Italy) were propagated in Tryptone Soya Broth (TSB) and Tryptone Soya Agar (Oxoid). *Escherichia coli* TG1 was used for propagation of phage clones. Stock organisms were maintained in LB broth (or TSB) containing 20% (v/v) glycerol at −80 °C.

Phage display libraries. The selections were performed through affinity-selection procedures described by Carnazza *et al*. (Carnazza *et al*., 2007; 2008). For the affinity selection procedures, two phage display libraries (pVIII-9aa and pVIII-12aa) were used (kind gift of Prof. F. Felici). These libraries were previously constructed (Felici *et al*., 1991) and consist of filamentous phages displaying random 9- and 12-mer peptides, respectively, fused to the major coat protein (pVIII). The nonapeptide and dodecapeptide libraries were constructed in the vector pC89 (Felici *et al*., 1991), by cloning a random DNA insert between the third and fifth codon of the mature pVIII-encoding segments of the pVIII gene (Luzzago and Felici, 1998). The relative binding of the phage clones from each round of affinity selection was estimated by ELISA assay. Then the most reactive individual phage clones were amplified and their DNA inserts were sequenced to determine the amino acid sequences of the displayed peptides.

Phage peptide selection. Library screening was performed using four rounds of affinity selection. Selection was performed by incubating 10^{12} phages with *S. epidermidis* and *S. aureus* cells (OD_{660} = 0.5) respectively, in Phosphate-Buffered Saline (PBS, 137mM NaCl, 2.7mM KCl, 10mM phosphate buffer, pH 7.4) for 60 min at Room Temperature (RT) with gentle shaking. Bacteria and phages were precipitated by spinning for 5 min at 16000 *xg*, and separated from unbound phages in solution by a series of 10 washing and centrifugation steps (16000 *xg*, 5 min) with 1ml TBS/Tween buffer (50mM Tris–HCl (pH 7.5), 150mM NaCl, 0.05% (v/v) Tween 20) each time. Bound phages were pelleted with cells and finally eluted with 200 µl of 0.2M glycine–HCl (pH 2.2) with gentle shaking at RT for 20 min, followed by neutralization with 150 µl of 1M Tris–HCl (pH 9.1). Phages eluted from the final round of affinity selection were used to infect *E. coli* TG1 cells. These cells were plated on ampicillin-containing LB agar plates to select for phage-infected bacteria. Bacterial colonies, each containing phages from a single library clone, were randomly selected and propagated for subsequent analyses.

ELISA test. Representative clones demonstrating the highest ELISA signals were investigated for their ability to preferentially interact with the select target in comparison to other potential targets.

A first ELISA test was carried out in order to verify positive reactivity of selected phage clones against bacterial target of interest. Wells of a 96-well ELISA plates were coated overnight at 4 °C with 100 µl suspensions of each bacterial strain (OD_{660} = 1) in carbonate buffer (35mM $NaHCO_3$, 15mM Na_2CO_3, pH 9.6); washed 3 times with washing buffer (0.05% w/v Tween 20 in PBS) by automatic plate washer; blocked with Blocking buffer (6% non-fat dry milk, 0.05% w/v Tween 20 in PBS) for 2 h at 37 °C; washed again; reacted with 100 µl of specific phage clone (10^{12} PFU/ml) in blocking buffer for 2 h at 37 °C with shaking; washed again; reacted with 100µl of anti-M13 peroxidase conjugate antibody (Amersham Biosciences, Buckinghamshire, UK) at a dilution of 1:2500 in Diluition Buffer (1% non-fat dry milk, 0.05% w/v Tween 20 in PBS) for 1 h at 37 °C; washed again; reacted with 100 µl of TMB (3,3,5,5-tetramethylbenzidine) liquid substrate system for ELISA for 45 min at RT and stopped with 100 µl of 1M H_2SO_4. Optical absorbance was recorded at 450 nm Multiscan FC (Thermo Scientific Type: 357). The positive clones were assayed again using a modified ELISA assay, in which Urea 4M is added to washing buffer for binding avidity and, finally, a cross-reactivity ELISA test, against other bacteria, for binding specificity.

Peptide sequence analysis. The insert DNA of phage clones was amplified by Polymerase chain reaction (PCR) and sequenced. The PCR products were purified using QIAquick PCR purification kit (Qiagen) and sequenced by the DNA sequencing service of CRIBI (University of Padova, Italy) using the M13 primer-40 (5'-GTTTTCCCAGTCACGAC-3').

Results and Discussions

9-mer and 12-mer random M13 phage display libraries were used to affinity select for peptides able to bind *S. epidermidis* and *S. aureus* cell surface epitopes. Selected phage clones were separated by centrifugation, separately amplified in *E. coli* strain TG1 and used for subsequent rounds of selection. The relative binding of the phage clones was estimated by ELISA test, using as negative control the insert-less vector pC89. In **Figure 1.3** ELISA test values of selected phage clones against *S. epidermidi* by 9-mer and 12-mer random M13 phage display libraries are showed.

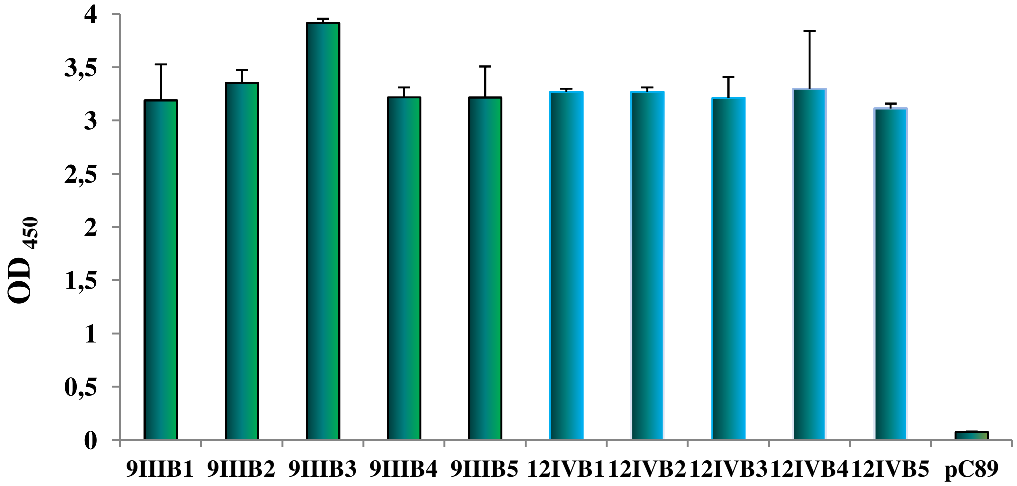

Figure 1.3 Reactivity ELISA test for clones selected against S. epidermidis. Clones named 9IIIB derive by the third round of selection of the 9-mer random M13 phage display libraries. Clones named 12IVB derive by the fourth round of selection of the 12-mer random M13 phage display libraries. A pC89 vector was used as a negative control. More details about the procedure are shown in the materials and methods section.

Data underline that all selected phage clones from both libraries had a similar reactivity. In order to determine clone binding specificity and avidity, selected clones from both libraries were investigated by means of further ELISA tests.

Below are presented selectivity results of all clones previously selected (**Figure 1.4, 1.5**).

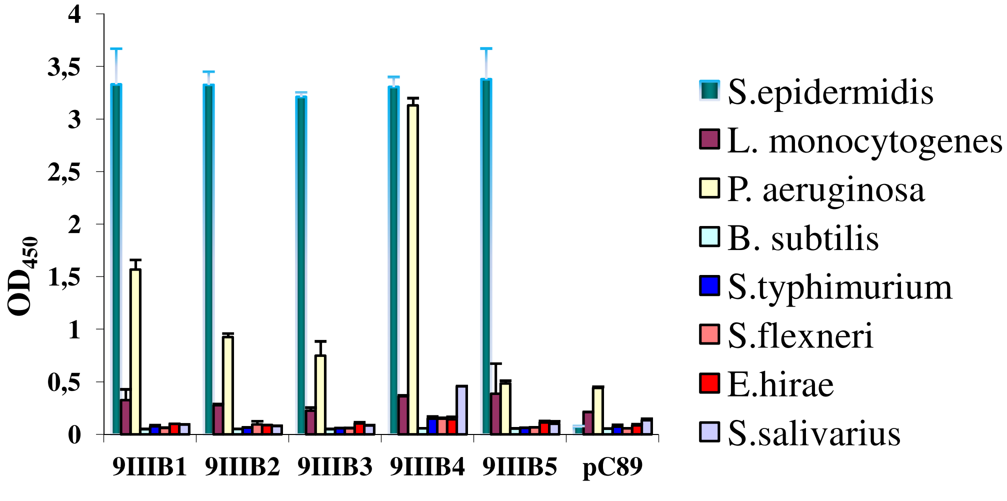

Figure 1.4 Cross-reactivity ELISA test for clones by 9-mer random M13 phage display libraries.

In these phage-capture ELISA assays, each organism was incubated with an equal amount of phage clone, and bound virions were detected by using anti-M13 peroxidase conjugate antibody and then TMB substrate colour development. More details about the procedure are shown in the materials and methods section.

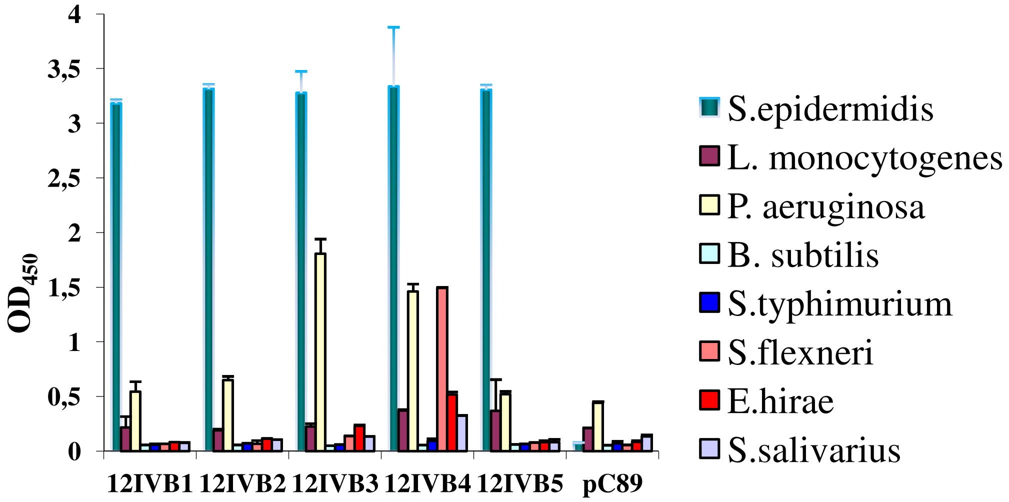

Figure 1.5 Cross-reactivity ELISA test for clones by 12-mer random M13 phage display libraries.
In these phage-capture ELISA assays, each organism was incubated with an equal amount of phage clone, and bound virions were detected by using anti-M13 peroxidase conjugate antibody and then TMB substrate colour development. More details about the procedure are shown in the materials and methods section.

9IIIB5 and 12IVB5 clones showed the highest selectivity against *S. epidermidis,* compared to other bacteria.

Below are presented the results of ELISA test about the avidity of both clones (**Figure 1.6**).

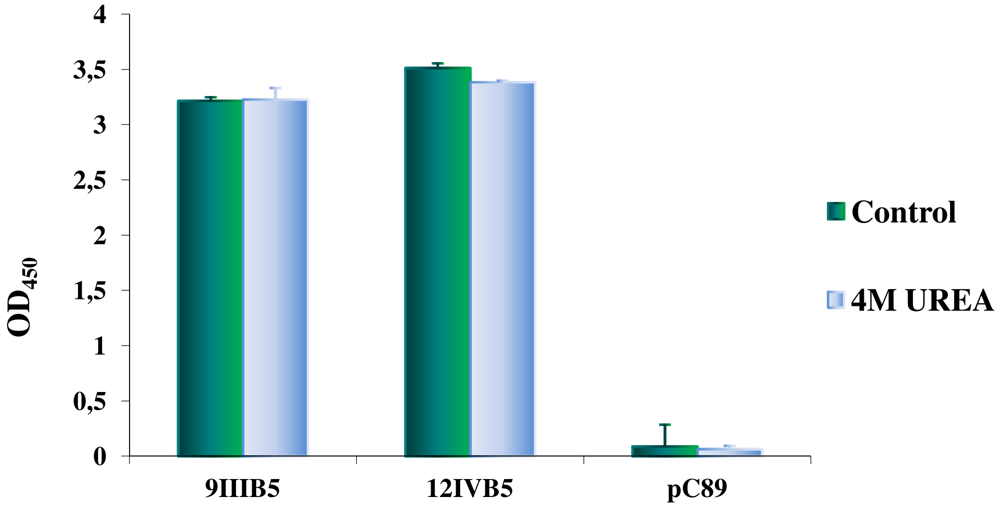

Figure 1.6 Avidity ELISA test for 9IIIB5 and 12IVB5 clones.
In these phage-capture ELISA assays, Urea 4M was added to washing buffer to verify binding avidity of selected clones. A *pC89* vector was used as a negative control. More details about the procedure are shown in the materials and methods section.

A similar procedure was carried out for the selected clones against the other bacterium of interest, namely *S. aureus.* In this case, the most reactive phage clone appeared to be arising from pVIII-9aa library, labeled as StauIVS5 **(Figure 1.7)**

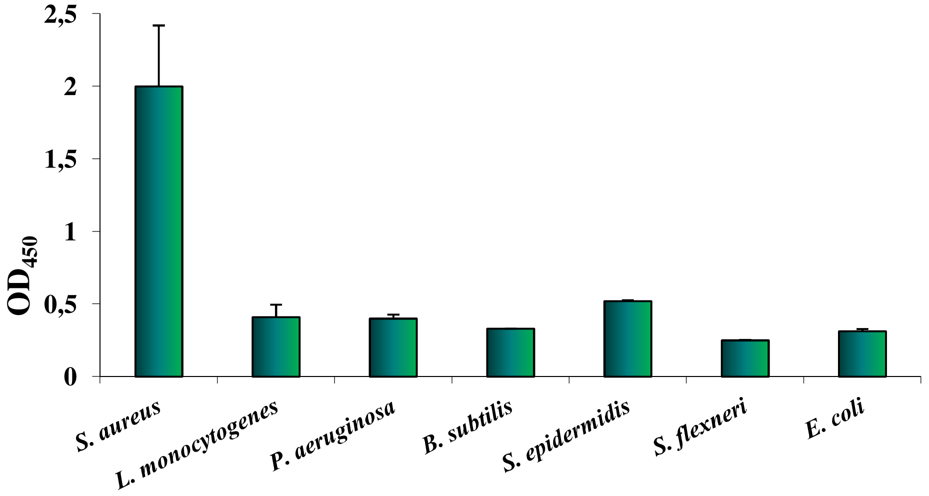

Figure 1.7 Cross-reactivity ELISA test for clone StauIVS5 by 9-mer random M13 phage display libraries.
In these phage-capture ELISA assays, each organism was incubated with an equal amount of phage clone, and bound virions were detected by using anti-M13 peroxidase conjugate antibody and then TMB substrate colour development. More details about the procedure are shown in the materials and methods section.

Moreover, ELISA test avidity, using Urea 4M, confirmed that StauIVS5 bind with high-avidity its bacterial target (**Figure 1.8**).

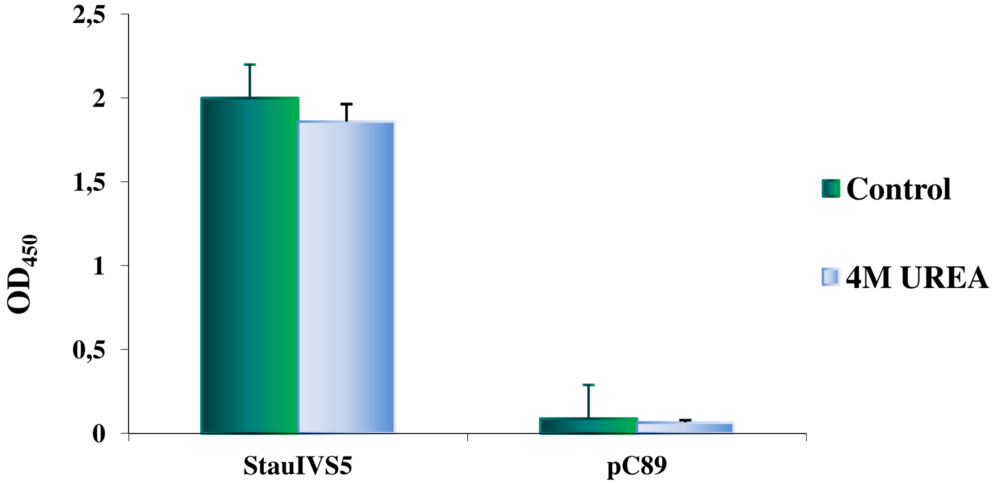

Figure 1.8 Avidity ELISA test for *StauIVS5* clone.
In these phage-capture ELISA assays, urea 4M was added to washing buffer to verify binding avidity of selected clones. A pC89 vector was used as a negative control. More details about the procedure are shown in the materials and methods section.

Selection of phage peptides targeting cancer membrane receptors

The discovery of novel approaches for the rapid and accurate detection of cell types, such as neoplastic cells, is one of the principal objectives in early-stage cancer diagnostics and monitoring of Minimal Residual Disease. Leukemia is one of the most blood malignancy affecting hematopoietic stem cells, bone marrow and lymphatic system. In this malignancy, the clonal population of neoplastic cells exhibits marked heterogeneity with respect to proliferation and differentiation (Bonnet and Dick, 1997; Reya *et al.*, 2001). The diagnostic gold standard of leukemia involves several methods, for individual treatment strategies and for the evaluation of treatment response, since there are different types of leukemia. For this reason, those strategies are often ineffective and time consuming, as well as expensive and often ineffective.

As alternative, M13 phage clones by a 9-mer pVIII display library can be used for detection and neoplastic cell imaging *in vitro*, including same advantages described in previous section. In this section a 9-mer pVIII M13 phage display library is screened against histiocytic lymphoma cell (U937) to identify peptides that selectively recognize these cells. This section describes the selection techniques for phage clones displaying peptides capable of specific and strong binding to the cell surface of U937, used as an *in vitro* model of cancer cells.

Materials and Methods

Cell line, bacteria and growth media. U937 cell line was purchased from American Type Culture Collection (ATCC® CRL-1593.2™) and maintained in RPMI 1640 with L-Glutamine (Lonza, BE12-702F) supplemented with 10% fetal bovine serum (FBS, Lonza DE14-801F), penicillin (100 units/ml) and streptomycin (100 µg/ml) at 37 °C in humidified 5% CO_2 incubator. TG1 *Escherichia coli* was used for propagation of phage clones. Stock organisms were maintained in LB broth containing 20% (v/v) glycerol at –80 °C.

Phage display libraries. A 9-mer random phage display library (kind gift of Prof. F. Felici) was constructed in the vector pC89, by cloning a random DNA insert between the third and fifth codon of the mature pVIII protein encoding segments of the pVIII gene (Felici *et al.*, 1991). This library was selected towards whole U937 cells in suspension.

Phage peptide selection. U937 cells were harvested by centrifugation at 800 rpm for 5 min, washed twice in Hank's buffered salt solution (HBSS Sigma-Aldrich pH 7.6) and resuspended at a concentration of $1 \cdot 10^6$ cells/ml. Selection procedure was according to Cao *et al.* with some modifications (Cao *et al.*, 2003). Three rounds of selection were performed and recombinant phages were identified by plating infected *E. coli* TG1 cells on LB agar added with X-Gal (5-bromo-4-chloro-3-indolyl-beta-D-galactopyranoside), IPTG (isopropyl thiogalactoside) and ampicillin. The presence of the insert was detected by X-gal which produces a characteristic blue dye when cleaved by β-galactosidase. Blue bacterial colonies, from third round of selection, were randomly selected. Each colony contained a single phage clone.

Elisa Test. The binding capacity of the thirteen phage clones to the target cells was tested in ELISA using as a negative control vector pC89.

$2.5 \cdot 10^4$ U937 cells in Phosphate-Buffered Saline (PBS) were dispensed in each well of a 96-well plate (Orange scientific) and incubated over night at 4 °C. They were fixed with methanol for 10 min at RT, washed three times with Washing Buffer (PBS + 0.05% Tween 20) and blocked with 100 µl of PBS + 5% Lactalbumin + 0.05% w/v Tween20 for 2h at 37 °C at 30 rpm. $1 \cdot 10^{10}$ phage clones, diluted in PBS + 1% Lactalbumin + 0.1% w/v Tween20, were added in each well and the plate was incubated for 1 h at 37 °C at 30 rpm. After three washing steps in Washing Buffer, cells were incubated with monoclonal anti-M13 peroxidase conjugate antibody (Amersham Biosciences, Buckinghamshire, UK) at a dilution of 1/5000 in PBS + 1% Lactalbumin + 0.1% w/v Tween20 (100 µl/well) for 1 h at 37 °C. After further three washing steps, antibody binding was detected by adding a 3,3′,5,5′-Tetramethylbenzidine (TMB) liquid substrate system for ELISA (Sigma-Aldrich), incubated for 45 min at RT and stopped with 25 µl of 1M H_2SO_4. Optical absorbance was recorded at 450 nm (MultisKan FC ThermoScientific).

Peptide sequence analysis. The insert DNA of phage clones was amplified by Polymerase chain reaction (PCR) and sequenced. The PCR products were purified using QIAquick PCR purification kit (Qiagen) and sequenced by the DNA sequencing service of CRIBI (University of Padova, Italy) using the M13 primer-40 (5'-GTTTTCCCAGTCACGAC-3'). The amino acid sequences were aligned according to their similarity by using the Clustal X 2.1 sequence alignment program using the IDENTITY series matrix (available at [http://clustalx.software.informer.com/2.1/]).

GeneDoc (available at [http://iubio.bio.indiana.edu/soft/molbio/ibmpc/genedoc-readme.html]) was used as a tool for visualizing, editing and analyzing multiple sequence alignments of the peptides (Thompson *et al*., 1994; Aiyar, 2000). Statistical analysis was performed in order to calculate amino acid frequency and diversity within the pool of peptides in the selected phage clones.

Results and Discussions

A 9-mer pVIII M13 phage display peptide library was screened against U937 cells in suspension. The most reactive phage clones showing a specific binding to U937 cells were amplified and their DNA was sequenced to determine the amino acid sequences of the displayed peptides. The deduced amino acid sequences were aligned by using CLUSTALX 2.1 software based on IDENTITY matrix, and the consensus sequence was obtained by using GENEDOC software. All sequences contained two positively charged amino acid residues (lysine and arginine) in the amino terminal region and non-polar amino acid residues in the central positions. These regions may be directly involved in the cell-target interaction. Among all peptides, EIII1 phage sequence showed the most significant similarity with consensus when all the clone sequences were re-aligned with consensus when all the clone sequences were re-aligned with this **(Figure. 1.9).**

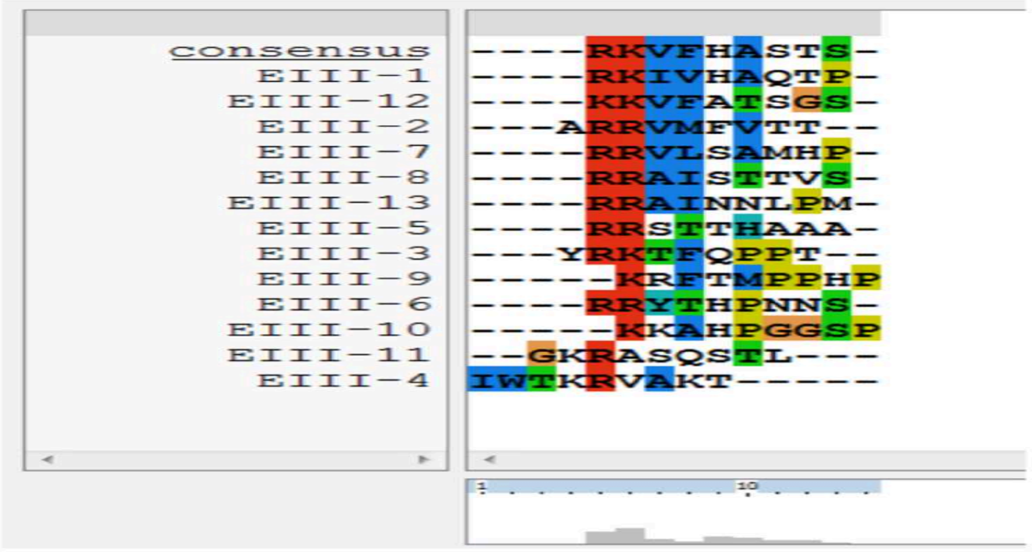

```
consensus ----RKVFHASTS-
  EIII-1  ----RKIVHAQTP-
 EIII-12  ----KKVFATSGS-
  EIII-2  ---ARRVMFVTT--
  EIII-7  ----RRVLSAMHP-
  EIII-8  ----RRAISTTVS-
 EIII-13  ----RRAINNLPM-
  EIII-5  ----RRSTTHAAA-
  EIII-3  ---YRKTFQPPT--
  EIII-9  -----KRFTMPPHP
  EIII-6  ----RRYTHPNNS-
 EIII-10  -----KKAHPGGSP
 EIII-11  --GKRASQSTL---
  EIII-4  IWTKRVAKT-----
```

Figure 1.9 Alignment of phage-displayed peptides.
The deduced amino acid sequences were aligned by using CLUSTALX 2.1 with the consensus sequence obtained by GENEDOC. Dashes indicate gaps used to maximize the alignment. This alignment shows conserved positively charged amino acid residues in the N-terminal region (K and R), flanked by nonpolar amino acids such as Valine (V), Isoleucine (I), Leucine (L) and Alanine (A). Data have been published in Biosensors and Bioelectronics (Lentini *et al*, 2015)

The relative binding of the phage clones was estimated by ELISA test, using as negative control the insertless vector pC89. The results showed that all selected phage clones had a similar reactivity and specificity for U937 cells **(Figure 1.10)**

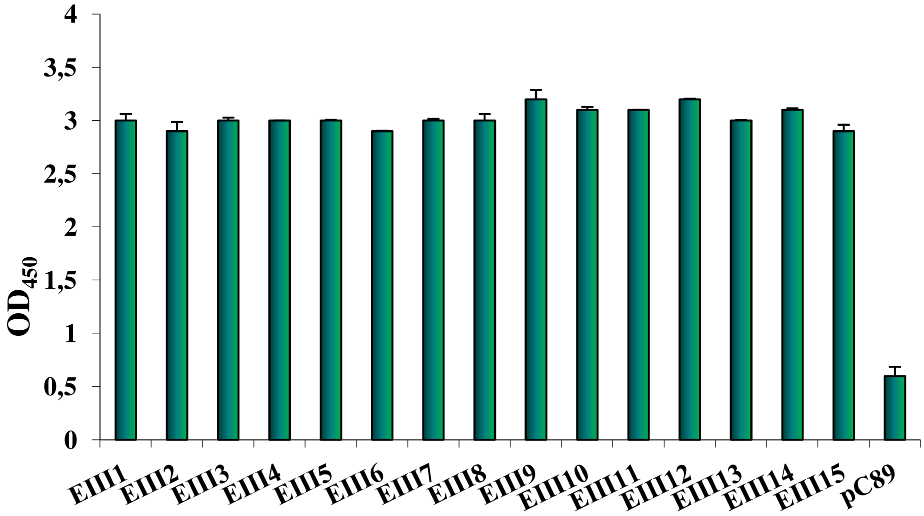

Figure 1.10 Reactivity ELISA test for clones selected against whole U937 cells
Clones named EIII derive by the third round of selection of the 9-mer random M13 phage display libraries. More details about the procedure are shown in the materials and methods section.
Data have been published in Biosensors and Bioelectronics (Lentini *et al*, 2015)

Phage-display as tool for biomarker discovery in neurodegenerative diseases

Alzheimer’s disease (AD) is a chronic neurodegenerative disorder, with a slow progression to dementia. In the past few years, the development and validation of specific tests, based on AD biomarkers detectable from serum, such as antibodies against β-amyloid (Aβ), has been the major goal of many research groups. Auto-antibodies are naturally present in human blood, in free form or complexed with Aß, both in AD patients and in healthy subjects. Although antibody levels change to disease progression, data reported about this topic are not consistent.

As proposed by some authors, it is reasonable to assume that it is unlikely that the unmodified antigens are the primary autoantigen to trigger the autoimmune response. Since the deposition of amyloids at diverse size, sequence, native structure, biological function can misfold and self-assemble, it is more plausible to assume that this could generate new epitopes (e.g.discontinuous) derived from amyloid-based aggregation. At this purpose, it is proposed a new approach to identify homologous mimotopes to Aβ42 as capture agents for diagnostically useful autoantibodies for AD (IgG-AD).

By bioinformatics tools, it has been verified a conformational homology between several Aβ42 and other proteins domains, particularly a chaperon protein (Caf1-M) of *Yersinia pestis*.

In this section a 12-mer random M13 phage display (12-mer and 12-mer cys) is used for a double binding screening against YPF19 a monoclonal antibody against the Caf1, and IgG-AD, obtained from several pools of AD sera. The selected clones were used as a probe to identify sera of AD subjects.

Materials and Methods

This section describes the selection techniques for phage clones displaying peptides able to specific and strong binding to IgG-AD.

Bioinformatic analysis . Several peptide sequences spanning the C-terminal regions of **Aβ42** protein were predicted according to hydrophilicity, exponential surface accessibility, flexibility, antigenicity and amphipathicity scales using the Protean program of DNAstar software package. Afterword 3D structures of misfolding of Aβ42, peptides and fibril forms were compared with all proteins present in PDB (Protein Data Bank), in order to identify the possible conformational mimotopes.

"Double Binding" screening. IgGs from a pool of five sera, obtained from AD cases (mean age= 77.4 years, mean MMSE value = 15.2), and mAb-YPF19, were covalently tied on paramagnetic-beads, Dynabeads®-proteinG (DYN). Biopanning of pVIII M13 phage display libraries was performed by alternating DYN-IgG-AD and DYN-mAbYPF19 (sequential double binding).

Affinity analysis. ELISA and immunoblot tests were used to select clones displaying peptides with conformational homology to Aβ42. The same were then evaluated by reactivity Elisa test.

Results and Discussions

Yersinia pestis Chaperon Protein Caf1-M (PDB ID=1p5u) showed similarity of conformational structure (**Figure 1.11**) to Aβ42, peptide (left panel) and fibril (right panel), respectively.

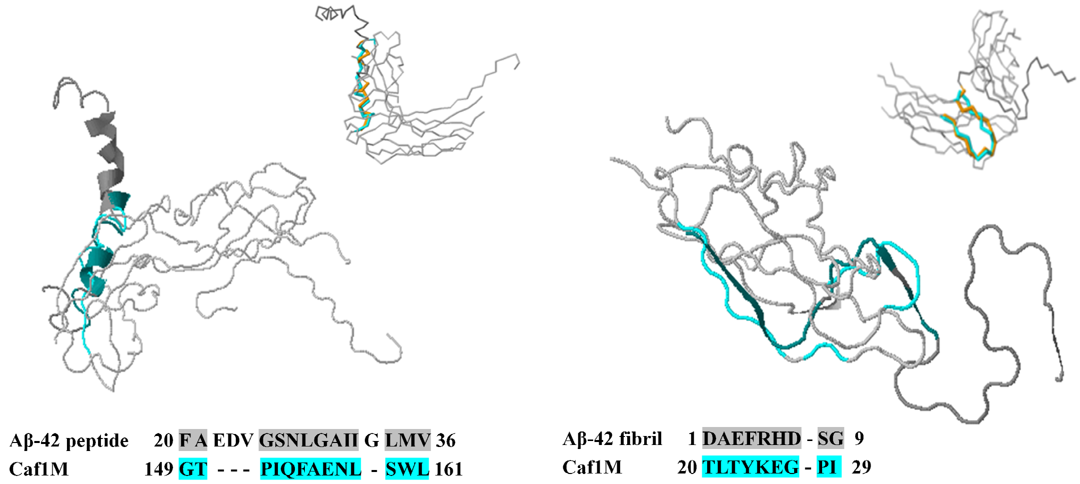

Figure 1.11 Bioinformatic analysis by PDBeFOLD tool .
Peptides (PDB ID= 1z0q) and fibril (PDB ID= 2NAO) forms were compared with all proteins present in PDB (Protein Data Bank), in order to identify the possible conformational mimotopes.

The residues that occupy an equivalent geometric shape in space were: amino acid 149-161 and 20-29 of Chaperon Protein Caf1-M (light colors) and 20-36 and 1-9 of Aβ42 (dark colors).

Figure 1.12 shows the most reactive clones against both pool of AD sera and mAb-YPF19 (left panel) and the reactivity of the same clones against both pool of AD and healthy individuals (CTR) sera (right panel).

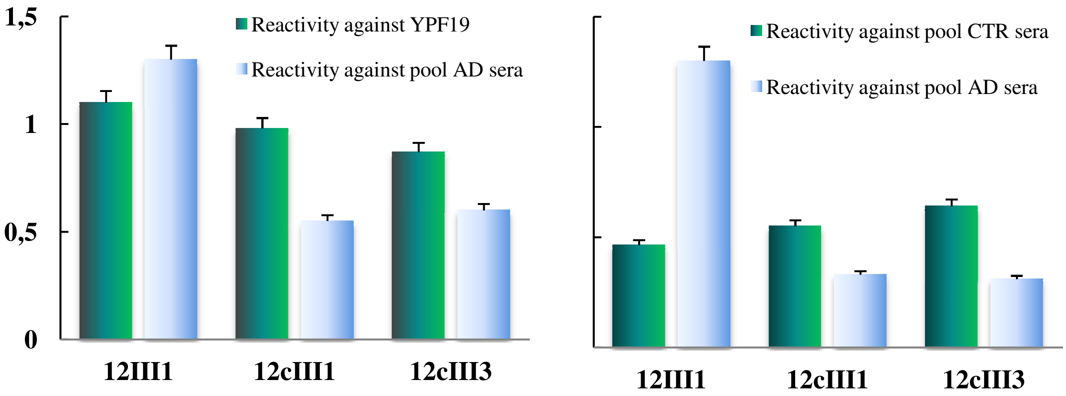

Figure 1.12 Reactivity between YPF19 and pool AD sera (left panel) and between pool AD and healthy individuals (CTR) sera (right panel).

Results by test Elisa reactivity suggest that 12III1 clone significantly discriminates levels of IgGs between AD and CTR sera, with a 95 % confidence interval (p-value = 0.03). Clone was tested in ELISA against 38 serum samples (20-AD and 18-CTR) (**Figure 1.13**).

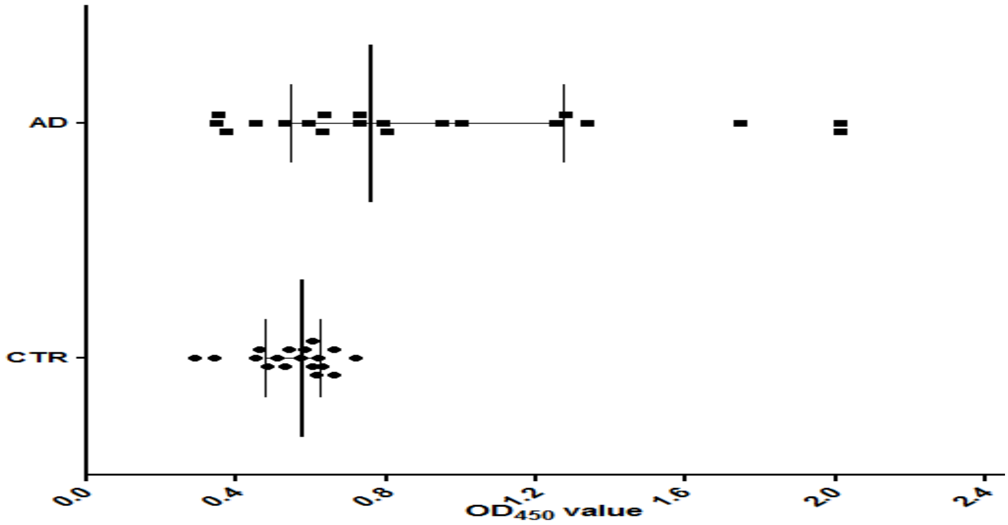

Figure 1.13 Reactivity of 12III1 against AD and healthy sera.

Data show levels of IgGs in AD patients significantly higher than healthy individuals (mean AD=0.93, CTR=0.55) (p-value = 0.0044). Intriguingly, IgGs present in AD sera bind with high-avidity the 12III1 phage clone, as confirmed by avidity test using Urea 4M (mean AT= 91.43).

Acknowledgements

This activity was partially funded by Italian Ministry of Education, University and Research (MIUR) by means of the national Program PON R&C 2007–2013, project project HIPPOCRATES – Development of Micro and Nano-Technologies and Advanced Systems for Human Health (PON02_00355_29641931).

Phage-display libraries were a kind gift of Prof. Franco Felici.

The activity "**Phage-display as tool for biomarker discovery in neurodegenerative diseases**" was carried out in collaboration with:

Professor A. Nicoletti and Professor M. Zappia, Section of Neurosciences, Department G.F. Ingrassia, University of Catania, Italy

Doctor S. Conoci and S. Petralia, STmicroelectonic Catania, Italy

Bibliography

Aiyar A. The use of CLUSTAL W and CLUSTAL X for multiple sequence alignment. 2000. Methods Mol. Biol. 132, 221-41.

Barbas CF, Kang AS, Lerner RA, Benkovic SJ. Assembly of combinatorial antibody libraries on phage surfaces: The gene III site. 1991. Pro Nat Acad Sci U S A. 88, 7978-82.

Bonnet D, Dick JE. Human acute myeloid leukemia is organized as a hierarchy that originates from a primitive hematopoietic cell. 1997. Nat. Med. 3, 730–37.

Cao J, Zhao P, Miao XH, Zhao LJ, Xue LJ, Qi ZT. Phage display selection on whole cells yields a small peptide specific for HCV receptor human CD81. 2003. Cell. Res. 13, 473-79.

Cesareni G. Phage-plasmid hybrid vectors. 1988. Biotechnology. 10, 103-11.

Carnazza S, Gioffrè G, Felici F, Guglielmino SPP. Recombinant phage probes for Listeria monocytogenes. 2007. J. Phys. Condens. Matter 19,13.

Carnazza S, Foti C, Gioffrè G, Felici F, Guglielmino SPP. Specific and selective probes for *Pseudomonas aeruginosa* from phage-displayed random peptide libraries. 2008. Biosens. Bioelectron. 23, 1137–44.

Deroo S, Muller CP. Antigenic and immunogenic phage displayed mimotopes as substitute antigens: Applications and limitations. 2001. Comb. Chem. High Through Screen 4, 75-110.

Felici F, Castagnoli L, Musacchio A, Jappelli R, Cesareni G. Selection of antibody ligands from a large library of oligopeptides expressed on a multivalent exposition vector. 1991. J. Mol. Biol. 222, 301-10.

Kishchenko GP, Minenkova OO, Ilyichev A A, Gruzdev AD, Petrenko VA. Study of structure of phage-M13 virions containing chimeric B-protein molecules. 1991. Mol. Biol.-Engl. Transl. 25, 1171-76.

Kishchenko G, Batliwala H, Makowski L. Structure of a foreign peptide displayed on the surface of bacteriophage M13. 1994. J. Mol. Biol. 241, 208-13.

Lentini G, Fazio E, Calabrese F, De Plano LM, Puliafico M, Franco D, Nicolò MS, Carnazza S, Trusso S, Allegra A, Neri F, Musolino C, Guglielmino SPP. 2015. Phage-AgNPs complex as SERS probe for U937 cell identification. Biosens. Bioelectron. 74, 398–405.

Luzzago A, Felici F. Construction of Disulfide-Constrained Random Peptide Libraries Displayed on Phage Coat Protein VIII. 1998. Methods Mol. Biol. 87, 155–64.

McCafferty J, Griffiths AD, Winter G, Chiswell DJ. Phage antibodies: Filamentous phage displaying antibody variable domains. 1990. Nature 348, 552-4.

McConnell SJ, Kendall ML, Reilly TM, Hoess RH. Constrained peptide libraries as a tool for finding mimotopes. 1994. Gene, 151, 115-8.

Mead, D. A.; Kemper, B. Chimeric single-stranded DNA phage-plasmid cloning vectors. 1988. Biotechnology. 10, 85-102.

Parmley SF, Smith GP. Antibody-selectable filamentous fd phage vectors: affinity purification of target genes. 1988 Gene 73, 305-18.

Reya T, Morrison SJ, Clarke M F, Weissman IL. Stem cells, cancer, and cancer stem cells. 2001. Nature. 415, 105–11.

Smith GP. Filamentous fusion phage: novel expression vectors that display cloned antigens on the virion surface. 1985. Science 228, 1315-17.

Smith GP. Gene 1993, 128, 1-2.

Smith G P, Petrenko VA. Phage display. 1997. Chem. Rev. 97, 391-410.

Petrenko VA, Smith GP. Phage from landscape libraries as substitute antibodies. 2000. Protein Eng. 13, 101–04.

Petrenko VA, Vodyanoy VJ. Phage display for detection of biological threat agents. 2003. J. Microbiol. Methods 53, 253–62.

Petrenko VA, Sorokulova IB. Detection of biological threats. A challenge for directed molecular evolution. 2004. J. Microbiol. Methods, 58, 147-68.

Ponsel D, Neugebauer J, Ladetzki-Baehs K, Tissot K. High affinity, developability and functional size: the holy grail of combinatorial antibody library generation. 2011. Molecules 16, 3675-700.

Rodi DJ, Makowski L. Phage-display technology - finding a needle in a vast molecular haystack. 1999. Curr. Opin. Biotechnol. 10, 87-93.

Thompson JD, Higgins DG., Gibson TJ. CLUSTAL W: improving the sensitivity of progressive multiple sequence alignment through sequence weighting, position-specific gap penalties and weight matrix choice. 1994. Nucleic Acids Res. 22, 4673-80.

Zwick MB, Shen J, Scott, JK. Phage-displayed peptide libraries. 1998. Curr. Opin. Biotechnol. 9, 427-39.

CHAPTER 2

Raman spectroscopy applied to cellular systems

Introduction

The label-free imaging of cell systems allows clustering of cells based on their inherent chemical makeup. Imaging based on label, such as fluorescent labels, distinguish one cell type from another by the binding between label and a cell surface marker. Differently the use of Raman analysis includes contributions not only from surface markers, but also influences from the signaling pathways and intracellular molecules which relate to the current state of the cell as well as cell type and function.

Spectroscopy can be defined as an analysis technique to study the interaction of electromagnetic radiation with atoms and molecules. The scattering of a light after interaction with matter grades into its component energies (colors). The resultant dissection of energies can be used to analysis that matter's physical properties.

When the energy of an incident photon is unaltered after collision with a molecule, the scattered photon keeps same frequency (elastic or Rayleigh scattering). Differently, if energy is transferred from the molecule to the photon or vice versa, the scattered photon has less or more than the energy of the incident photon (inelastic or Raman scattering).

Scattered photons with more energy will be shifted to a lower frequency (red-shifting or Stokes shift) (Diem *et al*, 2008; Wachsmann-Hogiu *et al*, 2009), while photons with less energy will be shifted to a higher frequency (blue-shifting or anti-Stokes shift) (Diem *et al*, 2008; Wachsmann-Hogiu *et al*, 2009), to balance in both cases the total energy of the system. Raman scattering is an example of inelastic scattering because of the energy transfer between the photons and the molecules during their interaction. The difference in energy between the incident and scattered photons corresponds to the energy of the molecular vibration (Wachsmann-Hogiu *et al*, 2009).

The loss (or gain) in the photon energies corresponds to the difference in the final and initial vibrational energy levels of the molecules participating in the interaction. The resultant spectra are characterized by shifts in wave numbers (inverse of wavelength in cm^{-1}) from the incident frequency. The frequency difference between incident- and Raman-scattered light is termed the Raman shift, which is unique for individual molecules and represented as 1/cm. Raman peaks are spectrally narrow, and in many cases can be associated with the vibration of a particular chemical bond (or a single functional group) in the molecule (Choo-Smith *et al*, 2002). The vibrations are molecular bond specific allowing a biochemical fingerprint to be constructed of the material (Harris *et al,* 2009).

It is important to note that, depending on whether the bond length or angle is changing, vibrations are subdivided into two classes: stretching (symmetric and asymmetric) and bending (scissoring, rocking, wagging and twisting).

There are six different vibrational modes. In symmetric and asymmetric stretching types, the lengths of the bonds become unstable. In another four types, the length remains stable and the angulations of the bonds changes (**Figure 2.1**).

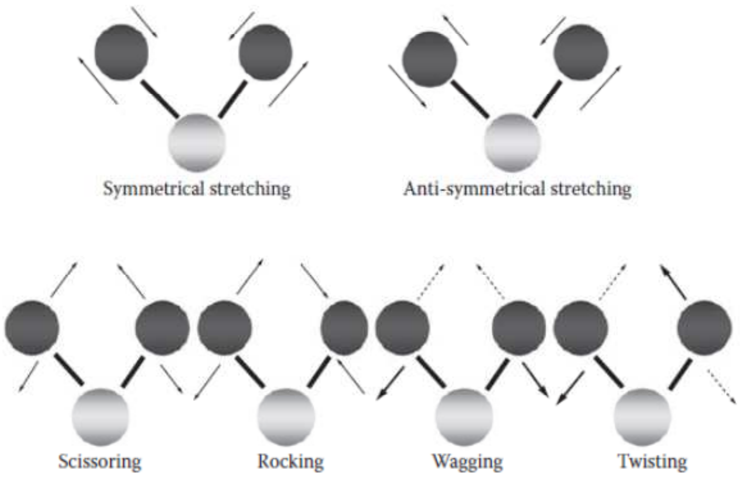

Figure 2.1 Different types of vibration of the chemical bonds (Rehman *et al*, 2012)

In this section, it's verified the ability of Raman measurement to discriminate cellular systems, such as bacterial pathogens or neoplastic cells. The large amount of information present in the vibrational spectra were evaluated by multivariate technique, including principal component analysis (PCA) and Hierarchical Cluster Analysis (HCA), that allowed these many subtle spectral differences to be clarified and used to classify cell types. Particularly, Raman spectroscopy allows identifying pathogenic bacteria, namely *Staphylococcus epidermidis* ATCC 12228, *Staphylococcus aureus* ATCC 29213 and *Pseudomonas aeruginosa* ATCC 27853, without the use of any label type. Moreover, Raman spectroscopy represents a good tool for discrimination of cell type, belonging to different cell lines. At this purpose, cells by four different cell lines, namely histiocytic lymphoma (U937), laryngeal carcinoma (HEp-2) and myelome multiple (MM1 and U266B1), were spectrophotometrically evaluated. Subsequently the same cell lines are evaluated individually on the basis of their different metabolic state and chemo-resistance to some drugs.

Identification of pathogenic microbes by Raman spectroscopy

Identification of pathogenic microbes is an important public safety issue in many fields. However, their exactly identification is very complex. Recently, micro-Raman spectroscopy emerges as an innovative and fast detection technique to well classify molecular fingerprint. The acquired Raman spectra contain important information about the complex structure of the investigated cell. Especially in the wave number region below 1800 cm^{-1} interesting vibrational features due to proteins (amide I, II, III), aromatic amino acids (phenylalanine (Phe)) and nucleic acid components (guanine (G), adenine (A)) are present. Previous chapter has shown the potential for phage display to targeting membrane receptors of pathogenic bacteria.

Materials and Methods

Cell lines and culture conditions. For Raman analysis pathogenic bacteria *S. epidermidis* ATCC 12228, *S. aureus* ATCC 29213 and *P. aeruginosa* ATCC 27853 were grown in their respective culture media. Stock organisms were maintained in LB broth (or TSB) containing 20% (v/v) glycerol at −80 °C.

Raman spectroscopy. Cells by each culture were taken from the broth and smeared by a diluting loop on CaF_2 slides (**Figure 2.2**). The samples were allowed to dry in air before characterization with Raman spectroscopy in the 450–2000 cm^{-1} range. Raman spectra were collected by the Horiba XploRa spectrometer equipped with an Olympus BX40 microscope, a Peltier cooled charge coupled device (CCD) sensor. The 532nm (2.33 eV) diode laser line was as the excitation source. An acquisition time of 100s allowed a sufficient signal/noise (S/N) ratio. To ensure reproducibility, experiments were performed in triplicate.

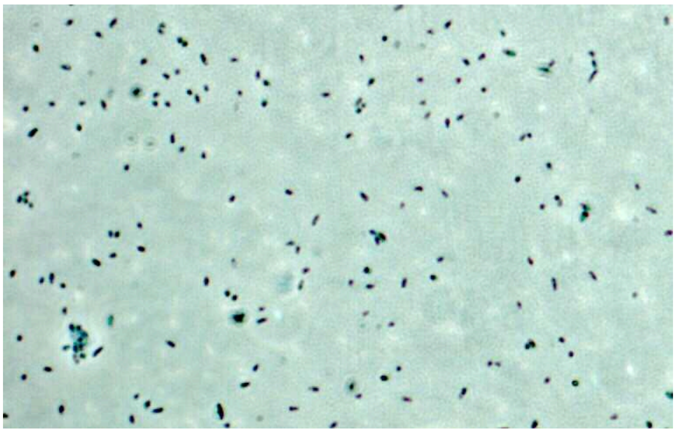

Figure 2.2 Microscopic image of a smear of single bacterial cells of *P. aeruginosa* ATCC 27853.

Multivariate data analyses were carried out with MatLab and XLSTAT (statistical software for Microsoft Excel) software. To improve analysis, all the spectra were previously subjected to some data treatment. First of all, a continuous baseline correction was performed using the adaptive iteratively re-weighted penalized least square algorithm (airPLS) (Savitzky and Golay, 1964). Corrected spectra were then normalized to their own maximum intensity and slightly smoothed using the Savitzky-Golay smoothing-derivative procedure (Zhang *et al*, 2010). The resulting spectra were loaded into rows of a matrix which was used as input for Principal Component Analysis (PCA) and subsequent and Hierarchical Cluster Analysis (HCA).

Results and Discussions

In **Figure 2.3** representative micro-Raman spectra from the three pathogenic bacterial species are shown exemplarily.

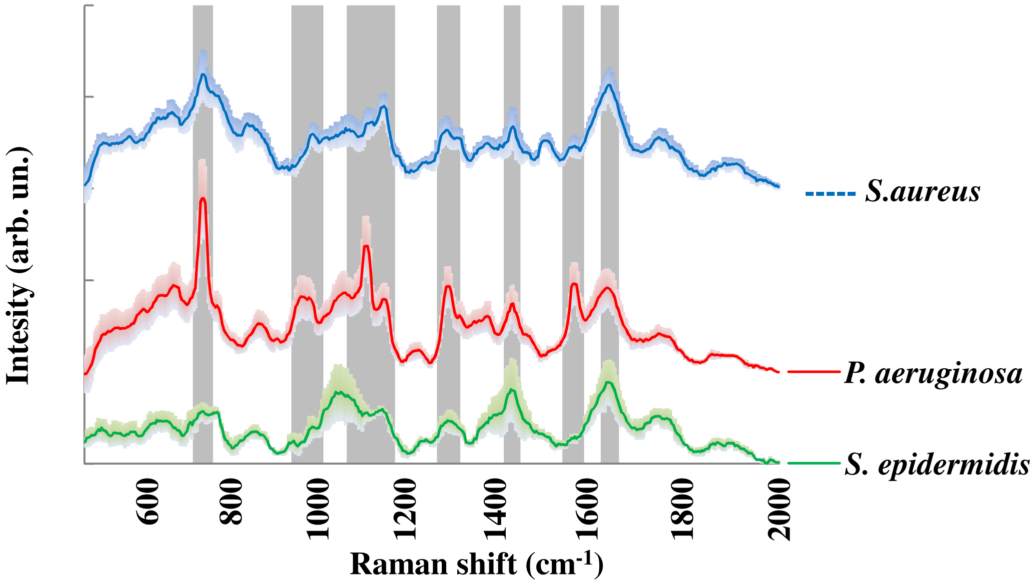

Figure 2.3 Representative micro-Raman spectra of *S. aureus* (blue line), *P. aeruginosa* (red line) and *S. epidermidis* (green line).

In the inset **(Figure 2.3)** is reported the mean Raman spectrum, averaged over all the Raman spectra acquired. The shaded area is enclosed within the standard deviation values limits. The spectra by each bacterial species contain important information about the complex structure of the investigated cell. Particularly, the wave number regions, inked in Figure 2.3 by light gray, show interesting vibrational features due to proteins, lipids and nucleic acids and can be used as molecular species-specific fingerprint. More details about the regions are shown in the table below, with corresponding vibrational modes, assignment tentative and references (**Table 2.1**).

Raman band (cm^{-1})	**Vibrational modes**	**Assignments**	**References**
710-760	Symmetric ring breathing mode	DNA/RNA bases	Chan et al., 2006
		Protein	Cheng et al., 2005
940-1010	Skeletal modes	Lipid	Shetty et al., 2006
	Symmetric ring breathing mode	Protein	Cheng et al., 2005
1070-1170	ν(C–C) or ν(C–O)	Lipid	Kast et al., 2008
	C–C, C–N stretching	Protein	Chan et al., 2006
1270-1320	Amide III	Protein	Stone et al., 2004
	CH2 deformation	Lipid	
1420-1450	Ring breathing modes	DNA/RNA bases	Chan et al., 2006
	δ(CH_2), δ(CH_3)	Lipid	Kast et al., 2008
1550-1600	C= C stretching	Protein	Cheng et al., 2005
	Symmetric ring breathing mode	DNA bases	Chan et al., 2006
1630-1670	Amide I	Protein	Cheng et al., 2005
	C= C stretching	Lipid	Stone et al., 2004

Table 2.1 Raman band used as molecular species-specific fingerprint, corresponding vibrational modes and their assignments.

Regions, just considered, have been used for the bacterial species discrimination. In order to demonstrate the feasibility of procedure, fifteen spectra by *S. epidermidis* (3), *S. aureus* (6) and *P. aeruginosa* (6) were analyzed. Because of the complexity of the spectra, the use of computational platforms, described in Materials and Methods section, have been required in order to easily visualize difference between bacterial species.

As an input set for the PCA and subsequent HCA procedures, the Raman spectra, after baseline subtraction area normalization and smoothing procedures, were used (Taleb *et al,* 2006). The result of a PCA analysis performed on a given data set is a vector which contains the relevance of principal components classified as a function of their variance. Thereafter, HCA algorithm is applied to the PCA results in order to separate the data into statistically similar groups.

Figure 2.4. shows results of PCA analysis and subsequent HCA procedure.

Data points in the PCA graph, showing more than the 75% of the variance within the first two principal components (PC1 and PC2), are exactly clustered by HCA algorithm. Data confirms that the most striking differences between the clusters are in wave number region previously described as molecular species-specific fingerprint. Moreover HCA highlights intra-species subgroups, probably due to a different metabolic state within the same cell population. This variance could also involve antibiotic resistance mechanisms within the same species. Studies on this are still ongoing.

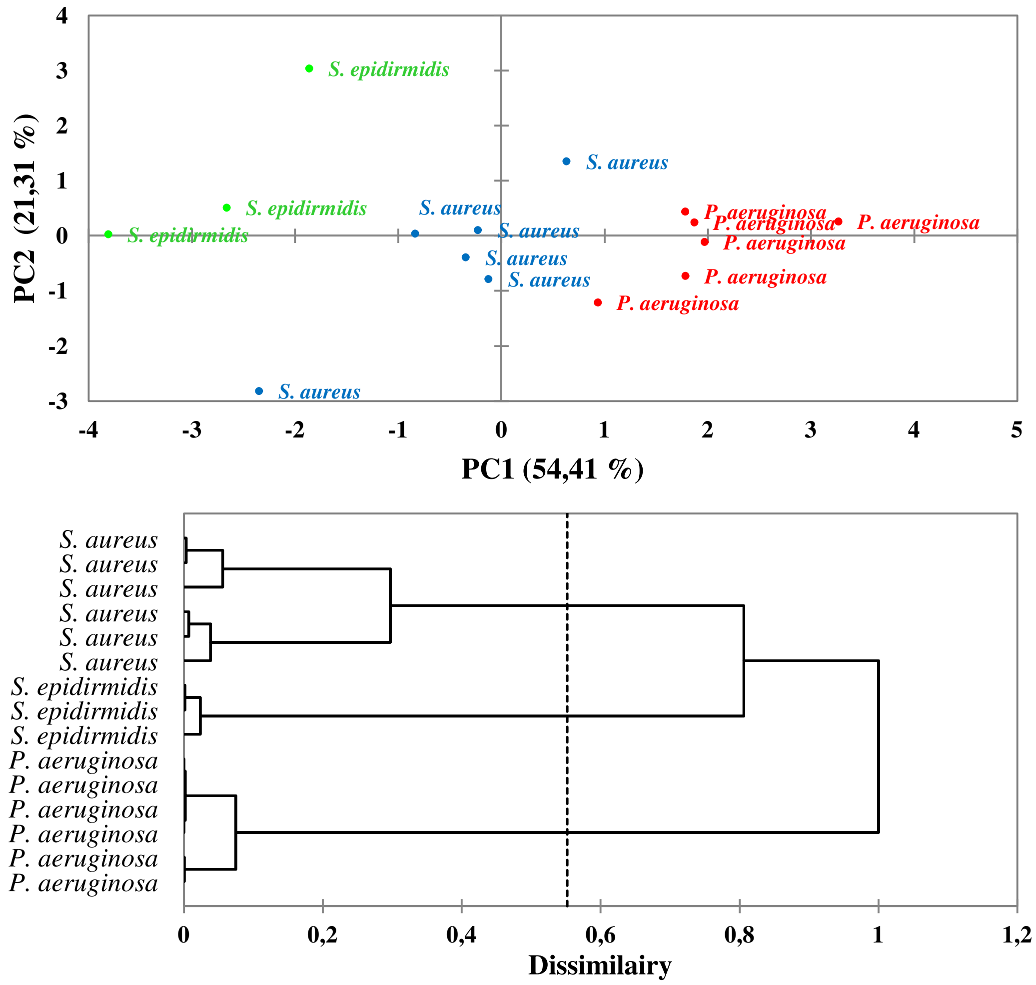

Figure 2.4 Output by PCA (upper panel) and HCA (under panel) analysis of bacterial spectra.

Application of Raman spectroscopy to discriminate cancer cells

Raman spectra analysis of cellular systems can be used as a diagnostic method to identify neoplastic cells within an unknown multicellular sample. Moreover, due to its fingerprint character, it can be used to describe the changes that take place in cancer cells. In fact, vibration of specific functional groups leads to the appearance of spectral absorption bands whose intensities and positions provide information regarding the sample's structural properties and can optically probe the molecular changes associated with diseased tissues (Chan *et al*, 2008; Stone and Matousek, 2008). Moreover, it can be used for deriving direct chemical/structural information in a label-free, nondestructive, and real-time manner at single-cell level, without requiring any exogenous modification of samples (Carey, 1999).

Materials and Methods

Cell lines and culture conditions.

U937 is a human cell line established from a diffuse histiocytic lymphoma. U937 cell line was purchased from American Type Culture Collection (ATCC® CRL-1593.2™, Milan, Italy) and maintained in RPMI 1640 with L-Glutamine (Lonza, Basel, Switzerland) supplemented with 10% fetal bovine serum (FBS, Lonza, Basel, Switzerland), penicillin (100 units/ml) and streptomycin (100 µg/ml) at 37 °C in humidified 5% CO_2 incubator.

HEp-2 cell line was originally propagated from a human laryngeal carcinoma. Cell line was purchased from American Type Culture Collection (ATCC® CCL-23™, Milan, Italy) and maintained in RPMI 1640 with L-Glutamine (Lonza, Basel, Switzerland) supplemented with 10% fetal bovine serum (FBS, Lonza, Basel, Switzerland), penicillin (100 units/ml) and streptomycin (100 µg/ml) at 37 °C in humidified 5% CO_2 incubator.

MM.1S (ATCC® CRL-2974™) and MM.1R (ATCC® CRL-2975™) cell lines were purchased from the American Type Culture Collection (ATCC; Rockville, MD, USA). Both the cell lines were cultured in RPMI 1640 medium supplemented with 10% fetal bovine serum (FBS), 100 units/ml penicillin, 100 µg/ml streptomycin, and 2 mM L-glutamine (Sigma-Aldrich, Milan, Italy).

U266B1 (ATCC® TIB-196™) cell lines were purchased from the American Type Culture Collection (ATCC; Rockville, MD, USA). Cell lines were cultured in RPMI

1640 medium–supplemented with 2mM Glutamine and 10% Feetal Bovine Serum (FBS), and maintained around $5 \cdot 10^6$ cells/ml in humidified atmosphere at 5% CO_2 and 37 °C.

U266B1 drug resistance (U266-BzR) cells were generated by dose escalation of bortezomib over 6 months by once weekly treatment with bortezomib starting at 16 nmol/l; the bortezomib concentration was doubled every 3 weeks until a final growth concentration of 64 nmol/l was reached. Cultures were removed from bortezomib for 14 days or 6 months before analysis and cultured in a manner consistent with the parental lines.

Preparation protocol. In order to measure the average number of viable cells, before carrying out Raman spectroscopic analysis, samples by each cell culture were stained with Trypan Blue (Sigma-Aldrich, Milan, Italy) and counted. $1 \cdot 10^6$ viable cells/mL were centrifuged at 500 *xg* for 5 min and washed twice in Phosphate Buffer Saline (PBS, Sigma-Aldrich, Milan, Italy) to remove all traces of culture medium. Finally, 50 µl of cell suspension were deposed on a CaF_2 slide treated with 0.01% polylysine (Sigma-Aldrich, Milan, Italy). Each sample was fixed by air-drying in sterile conditions for 15 min. All tests were performed in triplicate.

About HEp-2, these cells are able to adhere to the surface and grow to fill the entire available area (confluent culture). The preparation protocol provided a preliminary trypsinization process of fully confluent culture by treatment with trypsin-EDTA. Then, the cultures were centrifuged at 500 *xg* for 5 min and washed twice in PBS buffer ($1 \cdot 10^5$ cells/mL). Finally 50 µl of cell suspension were deposed on CaF_2 slide, treated as previously described. Each sample was fixed by air-dried fixation in sterile condition for 15 min. All tests were performed in triplicate.

Raman scattering measurements were carried out by means of Horiba XploRA micro-Raman spectrometer using the 532 nm laser line, focused on the sample's surface through the 100X objective of a microscope. The backscattered radiation was collected by the same microscope optics and dispersed by a monochromator equipped with a 600 line/mm holographic grating. The dispersed radiation was detected by means of a Peltier-cooled charged-coupled device (CCD) sensor. In order to avoid samples degradation, the laser power at the sample surface was kept as low as possible (≈ 1 mW), while the integration and the accumulation times were fixed at 50 s and 3 s, respectively. In this condition, cells showed no damage. For each sample, Raman analyses were randomly performed on a low number of cells (30-35 cells) in different slide regions. Experimental conditions allowed the use of multivariate analysis, preserving both individual information of spectra and statistical significance of sample size.

Results and Discussions

In **Figure 2.5** are shown an average of all the Raman spectra acquired on a given cell line, together with the standard deviation values for all the observed contributions.

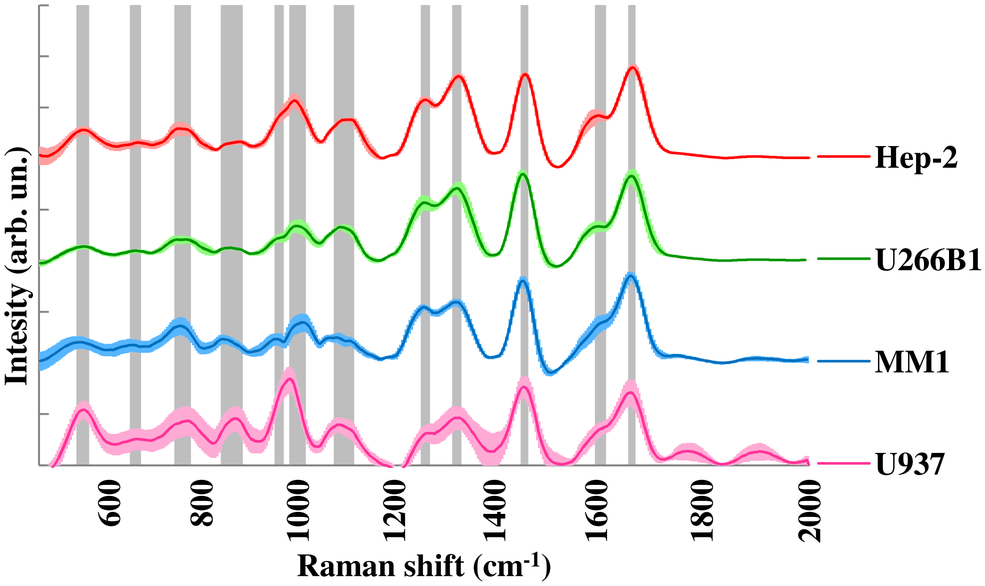

Figure 2.5 Representative micro-Raman spectra of HEp-2 (red line), U266B1 (green line) and MM1 (blue line) and U937 (pink line).

In the inset is reported the mean Raman spectrum, averaged over all the Raman spectra acquired. As described above about bacteria samples, shaded area is enclosed within the standard deviation values limits, while wave number regions inked in figure by light gray show the most important vibrational features due to proteins, lipids and nucleic acids that can be used as molecular species-specific fingerprint. More details about the regions are shown in the table below, with corresponding vibrational modes, assignment tentative and references (**Table 2.2**).

Raman band (cm^{-1})	Vibrational mode	Assignment	References
530-550	Ester group	Cholesterol	Krafft et al, 2005
650-670	C–S stretching mode C–C twisting mode	Protein	Cheng et al 2005
740-780	Symmetric ring breathing mode	DNA/RNA bases Protein	Cheng et al 2005 Stone, et al 2002; 2004
850-880	Ring breathing mode C–C stretching ring	Protein	Stone, et al 2002; 2004
980-1020	Symmetric ring breathing mode of benzene derivates, Symmetric ring breathing mode	Protein	Stone, et al 2002; 2004
1070-1100	ν(C–C) or ν(C–O) C–C, C–N stretching O–P–O backbone stretching	Lipid Protein DNA	Kast et al., 2008 Chan et al., 2006
1250-1270	Amide III Ring breathing modes = C–H bend	Protein DNA/RNA bases	Chan, et al 2006
1320-1330	CH3CH2 wagging mode	Protein DNA/RNA bases	Huang et al 2003
1450-1470	ν(C=C) CH2 wagging, amide (III) stretching CH2/CH3 deformation	Lipid Protein	Cheng, et al, 2005 Cipriani et al, 2008
1600-1615	Ring vibration	Protein	Lakshimi, et al 2002
1660-1670	Amide I C= C stretching	Protein Lipid	Cheng et al., 2005 Stone et al., 2004

Table 2.2 Raman band used as molecular cell line fingerprint, corresponding vibrational modes and their assignments.

Regions, just considered, have been used for the cell line discrimination, according the same procedure described in the previous section. In this case, procedure has been verified on forty spectra, teen for each cell line.

Data points in the PCA graph, showing more than the 70% of the variance within the first two principal components (PC1 and PC2), are clustered by HCA algorithm. In this case, because of the origin proximity between U266B1 and MM1 cell line, some spectra of the latter are erroneously grouped with U266B1 cluster. In fact, the other cell lines, namely U937 and HEp-2, are exactly grouped into different clusters.

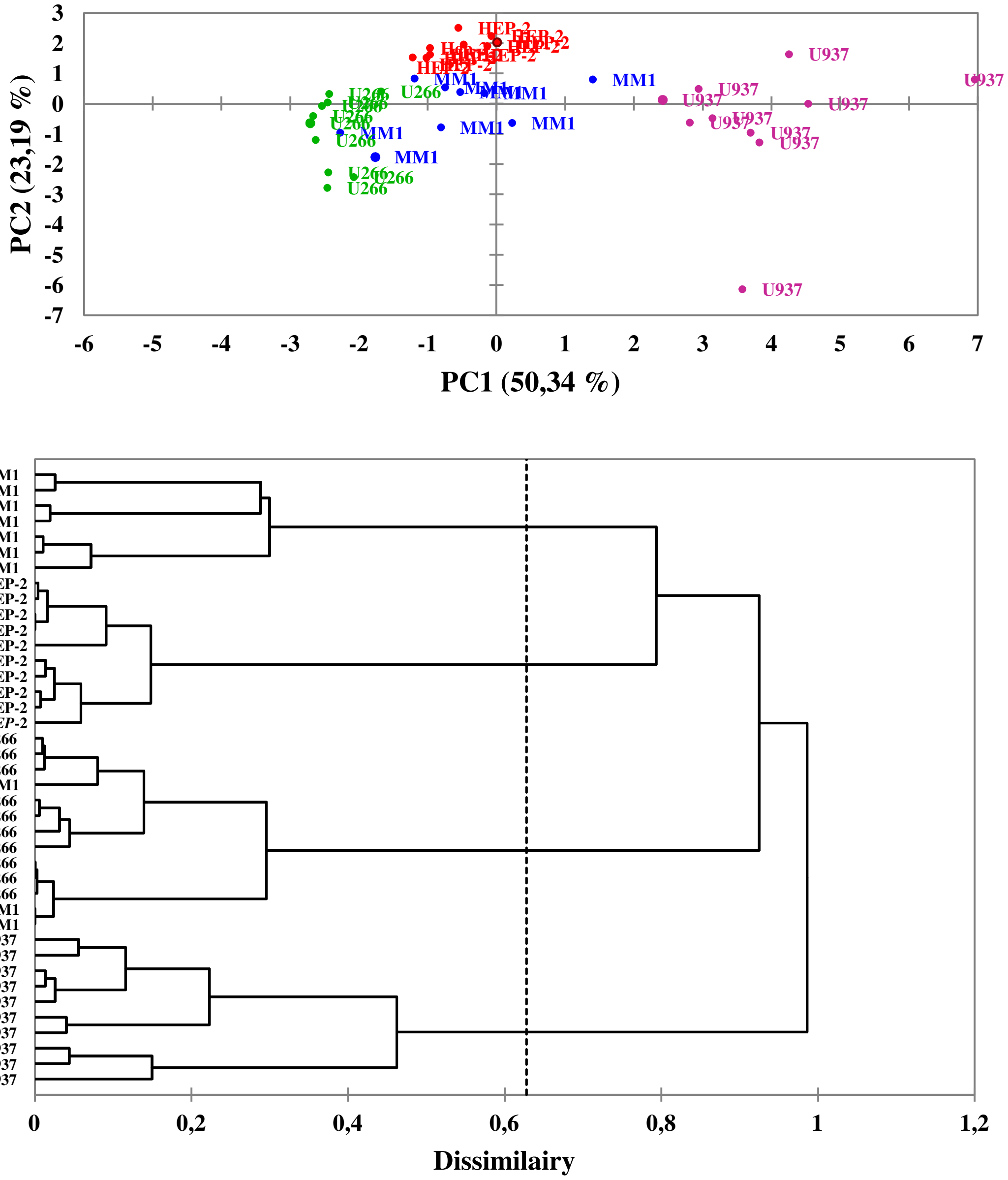

Figure 2.6 Output by PCA (upper panel) and HCA (under panel) analysis of cell line spectra

Data points in the PCA graph, showing more than the 70% of the variance within the first two principal components (PC1 and PC2), are clustered by HCA algorithm. In this case, because of the origin proximity between U266B1 and MM1 cell lines, some spectra of the latter are erroneously grouped with U266B1 cluster. In fact, the other cell lines, namely U937 and HEp-2, are exactly grouped into different clusters.

It should be noted that the experimental analysis was conducted on unsynchronized cell lines, therefore have been deliberately increased metabolic changes within each same cell line. In this case, subtle variances of spectra can occur within the same cell line and coupled with the experimental noise lead to intrinsic poor spectra reproducibility and to a low statistical analysis confidence level, such as in the case of minimal residual disease, e.g. tumor cells variation due to therapeutic treatments or, more simply, lifetime cells structural variation.

In this regard, it has been investigated if the Raman spectroscopy was able to highlight features associated to drug treatment and disease progression.

U937 cellular line can be chosen as a leukemia model, since it shows many monocytic characteristics, such as differentiation or apoptosis susceptibility, cytokine secretion phenomena and new receptors exhibition.

In order to increase those phenomena, spectral analysis was carried out on U937 cells cultured for 144 h, where a significant increase of apoptosis induction was observed by epifluorescence microscopy **Figure 2.7**.

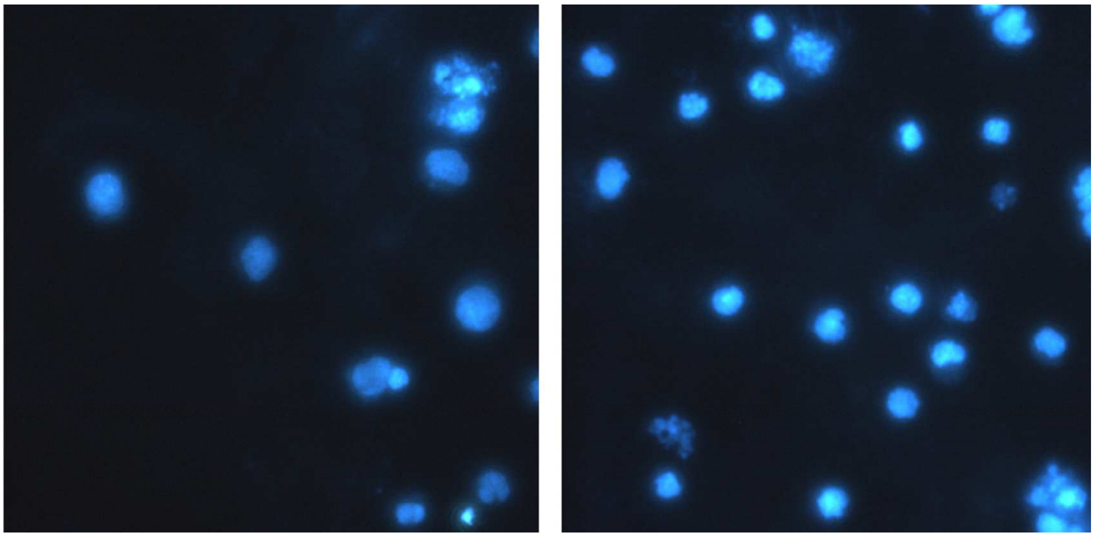

Figure 2.7 Fluorescence imaging by DAPI staining of U937 cells in aging culture. Data have been published in Spectrochimica Acta Part A: Molecular and Biomolecular Spectroscopy (Fazio *et al,* 2016)

After this time interval, about 20% of the cells on the average showed structural alterations of cellular nucleus that can be associated to apoptotic features.

The observed structural modifications can be highlighted in the Raman spectra as striking difference in the intensity of low frequency region, between 400 and 1200 cm^{-1}, mainly ascribable to nucleic acids and proteins. **Figure 2.8** shows representative spectrum, obtained averaging over all measurements, of two cell types (left panel) and intensity values of most discriminant peaks (right panel).

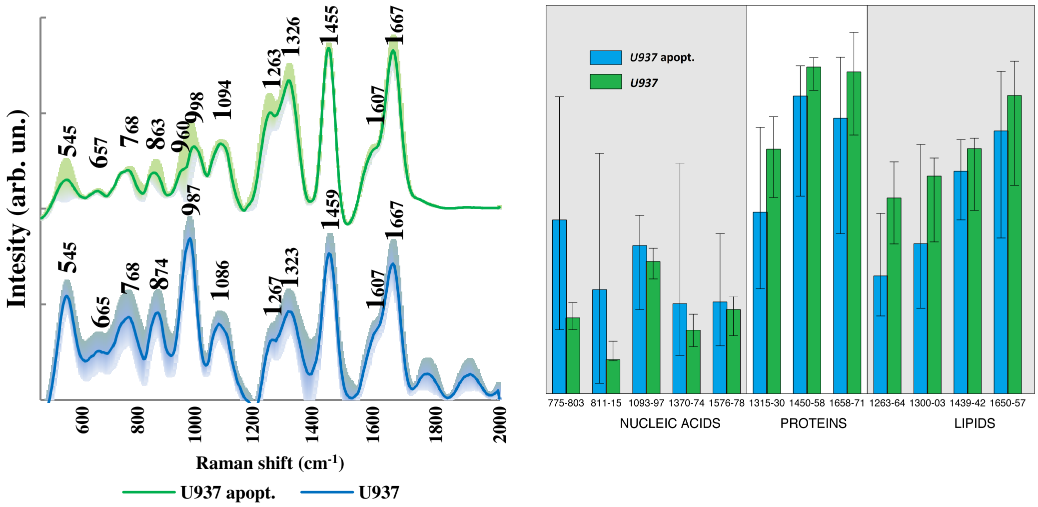

Figure 2.8 Representative micro-Raman spectra of U937 (left panel) and intensity values of most discriminant peak s(right panel). Data have been published in Spectrochimica Acta Part A: Molecular and Biomolecular Spectroscopy (Fazio *et al*, 2016)

Significant decrease of the bands intensities corresponding to nucleic acids is compatible with phenomena of fragmentation of the DNA and other nuclear components, already observed by DAPI staining, while a slight intensity increase of the features due to protein and lipids contributions is also compatible with phenomena a different transcriptional activity, abnormal protein folding and accumulation of both membrane and non-membrane lipids (triglycerides).

It has been proposed that oxidative stress leads to DNA damage, with the consequent accumulation of mutations, genomic instability, loss of function and apoptosis.

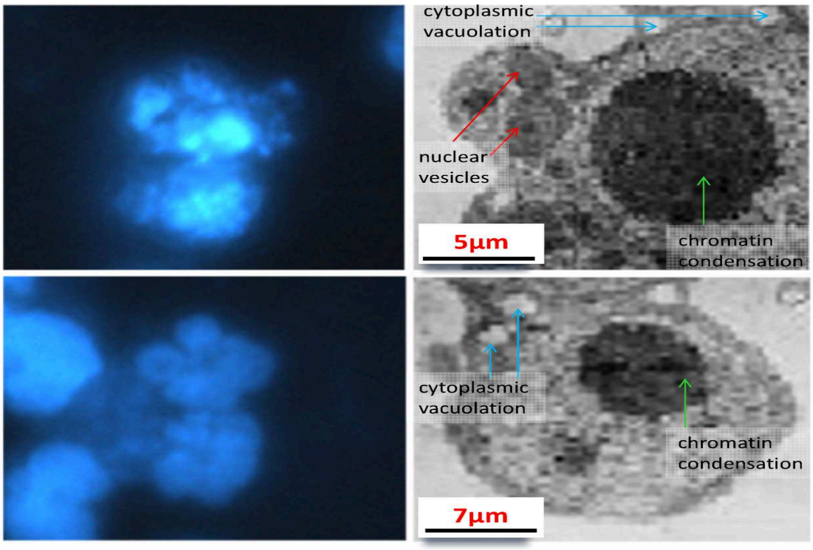

Figure 2.9 Fluorescence imaging by DAPI staining (left) and TEM images (right) of U937 cells in aging culture. Data have been published in Spectrochimica Acta Part A: Molecular and Biomolecular Spectroscopy (Fazio *et al*, 2016)

TEM images (**Figure 2.9 right**) show agglomerated nanostructures both outside the cells and engulfed in vesicles. All these morphological features are representative of cytoplasmic vacuolation (cyan arrow), nuclear vesicles budding from the nucleus (red arrows), as well as chromatin condensation (green arrows). On the overall, they are indicative of undergoing apoptotic cells (Mita *et al,* 2003) in good agreement with fluorescence data.

The results of the PCA analysis and of the subsequent HCA procedure confirms the presence of two Raman spectra sub-classes within the same cell line **(Figure 2.10)**.

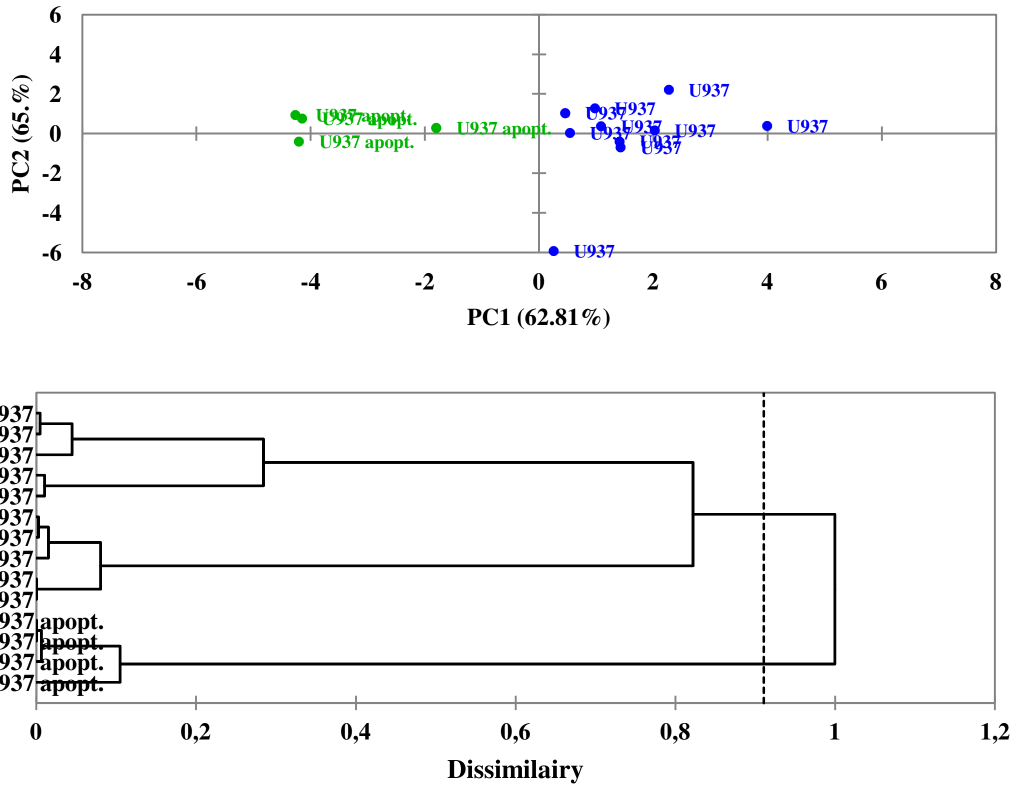

Figure 2.10 Output by PCA (upper panel) and HCA (under panel) analysis of U937 spectra. Data have been published in Spectrochimica Acta Part A: Molecular and Biomolecular Spectroscopy (Fazio *et al*, 2016).

Another aspect of drug treatment and disease progression can be the emergence of new cell subtypes with drug resistance within the same cell line.

This aspect has been dealt on multiple myeloma cells, namely MM1 and U266B1 cell lines, sensitive and resistant to dexamethasone and bortezomib, respectively.

Figure 2.11 shows an average of all the Raman spectra acquired on a given cell line, together with the standard deviation values for all the observed contributions.

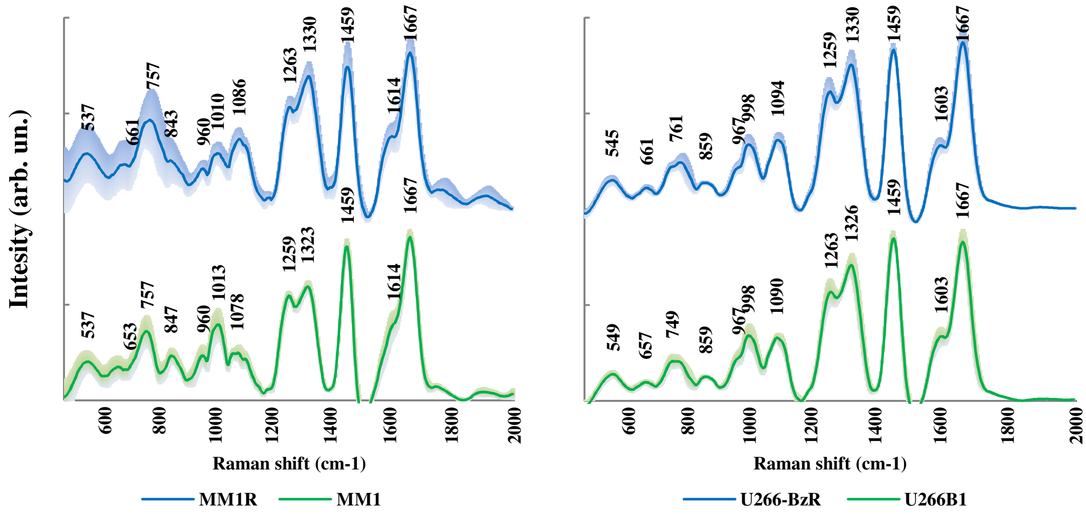

Figure 2.11 Representative micro-Raman spectra of MM1 (left panel) and U266B1 (right panel) cell line.

In both cell lines, Raman spectra of cell resistant show subtle differences, in terms of peaks positions and intensities, for nucleic acids, lipids and proteins specific bands. Particularly, it's observed significantly shifts in the regions 650-850, 950-1000 and 1250-1350 cm^{-1}. Regarding nucleic acids, the observed changes mainly involve the shift of peaks ascribable to phosphate backbone and DNA/RNA nucleotides contributions. Lipid contributions, in MM.1R Raman spectra, show differences in the shifts of bands due to ν(C–C), ν(C–O) and CH_3CH_2 in phospholipids. Finally, in protein contributions, main changes involve the shift of symmetric ring breathing in phenylalanine and tryptophan. Data could suggest a common resistance mechanism against different drugs, mainly due to a reorganization of biological macromolecules. This phenomenon has partially been worked out for MM1 cell lines, associating the acquisition of GC-resistance with a reduced heat-stress resistance and mechanical strength of cell membrane.

Below are shown results of the PCA analysis and the subsequent HCA procedure, for both cell lines (**Figure 2.12**)

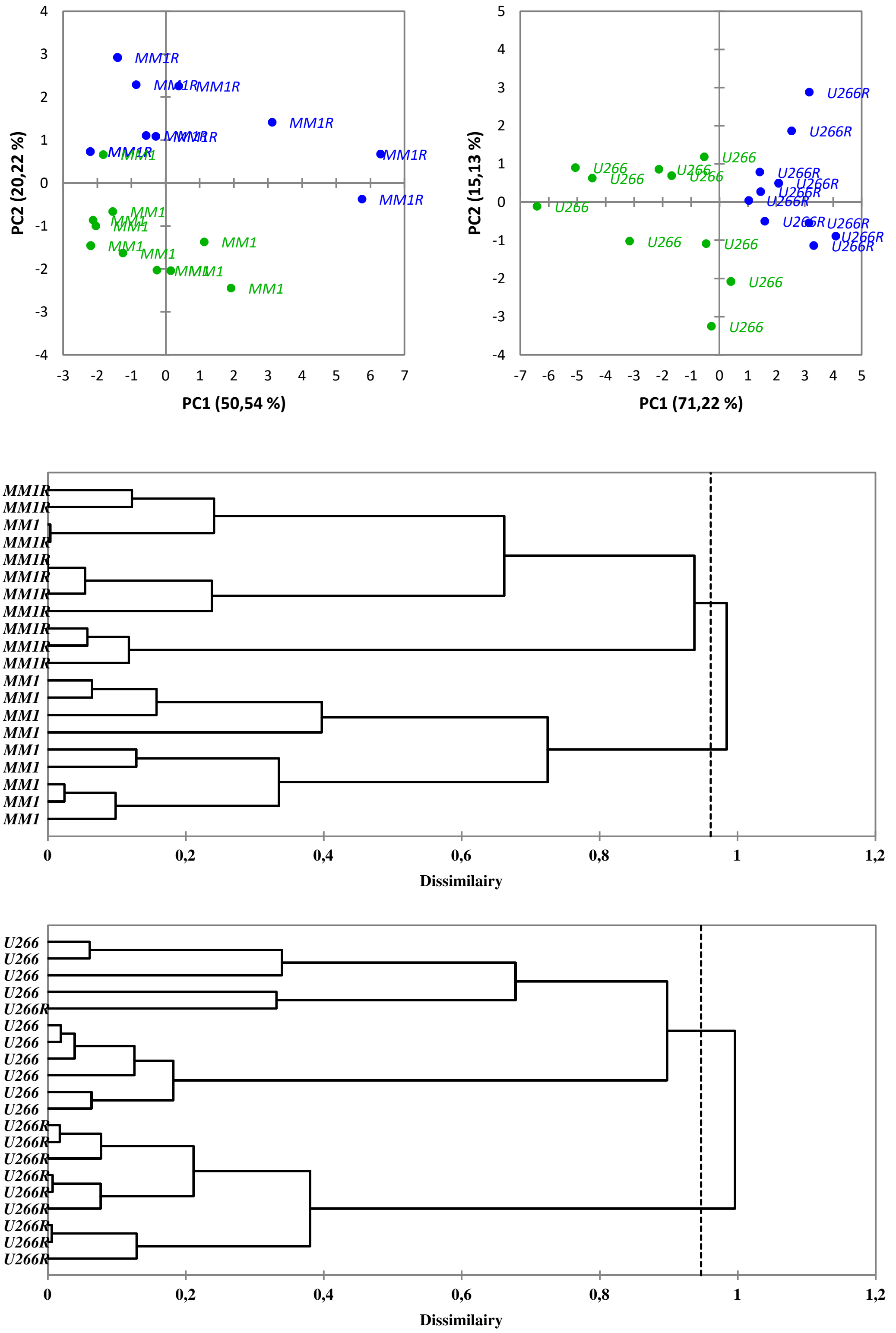

Figure 2.12 B Output by PCA (upper-left panel) and HCA (middle panel) analysis of MM1 spectra and Output by PCA (upper-right panel) and HCA (lower panel) analysis of U266B1 spectra.

About MM1 cell line, data points in the PCA graph show more than the 70% of the variance within the first two principal components (PC1 and PC2). However, HCA analysis shows for MM1R sub-group a less defined cluster with one spectrum incorrectly attributed to the MM1S. A similar data are obtained by PCA and subsequently HCA analysis. In this case results show a less defined cluster for U266B1 sub-group, with one spectrum incorrectly attributed to the U266-BzR.

Although the resistant cell subgroups are not exactly separated from their sensitive subgroups, those data pose the Raman spectroscopy as a powerful diagnostic tool not only in a preclinical phase, but also in during drug treatment to detect resistant cells.

In fact, the therapeutic effects can be brought out only after an extended therapeutic treatment, with a significant delay in the implementation of a truly effective therapy and unnecessary patient exposure to serious side effects. To this purpose the proposed method can be helpful in the speeding up cell identification, even if further research is needed to verify whether analysis of patient cells could allow the identification of the resistance to a given drug or to a specific combination of drugs, in order to address the appropriate pharmacological choice, also ensuring therapeutic success. Moreover the reported specific changes in the Raman spectra will be useful to better understand and to investigate further changes at the molecular level that lead to drug-resistant neoplastic cells.

Acknowledgements

This activity was partially funded by Italian Ministry of Education, University and Research (MIUR) by means of the national Program PON R&C 2007–2013, project project HIPPOCRATES – Development of Micro and Nano-Technologies and Advanced Systems for Human Health (PON02_00355_29641931).

XploRA Raman spectrometer was a kind gift of A.B.A.L. onlus Messina (Italy) (http://www.abalmessina.it).

This activity was carried out in collaboration with:

Doctor E. Fazio and Professor F. Neri Department of Mathematical and Computational Sciences, Physical Science and Earth Science (MIFT), University of Messina, Italy.

Doctor A. Allegra and Professor C. Musolino, Division of Hematology, Department of General Surgery, Pathological Anatomy and Oncology, University of Messina, Italy.

Doctor F. Cimino and Professor A. Saija, Department of Chemical, Biological, Pharmaceutical and Environmental Sciences, University of Messina, Italy.

Doctor S. Trusso Institute of Chemical-Physical Processes (IPCF)-CNR Messina, Italy.

Bibliography

Carey PR. Raman spectroscopy, the sleeping giant in structural biology, awakes. 1999. J. Biol. Chem.; 274: 26625–28.

Chan JW, Taylor DS, Zwerdling T, Lane ST, Ihara K, Huser T. Micro-Raman spectroscopy detects individual neoplastic and normal hematopoietic cells. 2006 Biophys. J. 90, 648–56.

Chan J, Fore S, Wachsmann-Hogiu S, Huser T. Raman spectroscopy and microscopy of individual cells and cellular components. 2008. Laser & Photon. Rev. 2, 325–49

Cheng WT, Liu MT, Liu HN, Lin SY. Micro-Raman spectroscopy used to identify and grade human skin pilomatrixoma. 2005. Micrsc. Res. Tech. 68, 75–79.

Choo-Smith L P, Edwards HGM, Endtz HP, Kros JM, Heule F, Barr H, Robinson J S Jr, Bruining HA, Pupells GJ. Medical applications of Raman spectroscopy: From proof of principle to clinical implementation. 2002. Biopolymers 67, 1–9.

Cipriani P and Smith CY. Characterization of thalidomide using Ramanspectroscopy. 2008. Spectrochem. Acta. A Mol. Biomol. Spectroscopy 69, 333–37.

Cretich, M., Damin, F., Pirri, G., and Chiari, M. 2006, Protein and peptide arrays: recent trends and new directions, Biomol. Eng. 23, 77-88.

Diem M, Griffiths PR, Chalmers JM. Vibrational Spectroscopy for Medical Diagnosis. 2008. London: John Wiley & Sons 187–202.

Fazio E, Trusso S, Franco D, Nicolò MS, Allegra A, Neri F, Musolino C, Guglielmino SPP. A micro-Raman spectroscopic investigation of leukemic U-937 cells in aged cultures. 2016. Spectrochem. Acta. A Mol. Biomol. Spectroscopy. 159, 21-29

Harris AT, Lungari A, Needham CJ, Smith SL, Lones MA, Fisher SE, Yang XB, Cooper N, Kirkham J, Smith DA, Martin-Hirsch DP, High AS. Potential for Raman spectroscopy to provide cancer screening using a peripheral blood sample. 2009. Head & Neck Oncology 1, 34.

Huang Z, McWilliams A, Lui M, McLean DI, Lam S, Zeng H. Near-infrared Raman spectroscopy for optical diagnosis of lung cancer. 2003. Int. J. Cancer 107, 1047–52.

Kast RE, Serhatkulu GK, Cao A, Pandya AK, Dai H, Thakur JS, Naik VM, Naik R, Klein MD, Auner GW, Rabah R. Raman spectroscopy can differentiate malignant tumors from normal breast tissue and detect early neoplastic changes in a mouse model. 2008. Biopolymers 89, 134–241.

Krafft C, Neudert L, Simat T, Salzer R.. Near-infrared Raman spectra of human brain lipids. 2005. Spectrochimia Acta 61, 1529–35.

Lakshimi RJ, Kartha VB, Krishna CM, Solomon JGR, Ullas G, Uma Devi P. Tissue Raman spectroscopy for the study of radiation damage: Brain irradiation of mice. 2002. Radiat. Res. 157, 175–82.

Mita P, De Luca A, Abbro L, Dini L. Ultrastructural analysis of apoptosis induced by apoptotic U937 cells conditioned medium. 2003. Ital. J. Zool. 70, 141–46.

Rehman IU, Movasaghi Z, Rehman S. 2012. Series in Medical Physics and Biomedical Engineering, CRC Press; A Taylor and Francis Book.

Savitzky A, Golay MJE. Smoothing and differentiation of data by simplified least squares procedures. 1964. Anal. Chem. 36, 1627–39.

Shetty G, Kedall C, Shepherd N, Stone N, Barr H. Raman spectroscopy: Evaluation of biochemical changes in carcinogenesis of oesophagus. 2006. Br. J. Cancer 94, 1460–64.

Stone N, Kendell C, Shepherd N, Crow P, Barr H. Near-infrared Raman spectroscopy for the classification of epithelial pre-cancers and cancers. 2002. J. Raman Spectroscopy 33, 564–73.

Stone N, Kendall C, Smith J, Crow P, Barr H. Raman spectroscopy for identification of epithelial cancers. 2004. Faraday Discussion 126, 141–57.

Stone N, Matousek P. Advanced transmission Raman spectroscopy: A promising tool for breast disease diagnosis. 2008. Cancer Res. 68, 4424–30.

Taleb A, Diamond J, McGarvey JJ, Beattie JR, Toland C, Hamilton PW. Raman microscopy for the chemometric analysis of tumor cells. 2006. J. Phys. Chem. B 110 19625–31.

Wachsmann-Hogiu S, Weeks T, Huser T. Chemical analysis in vivo and in vitro by Raman spectroscopy: From single cells to humans. 2009. Curr. Opin. Biotechnol. 20, 63–73.

Zhang ZM, Chen S, Liang YZ. Baseline correction using adaptive iteratively reweighted penalized least squares. 2010. Analyst 135, 1138–46.

CHAPTER 3
Selective phage clones for fluorescence imaging

Introduction

Fluorescence is a highly sensitive method for molecular and cell targeting. For example, intrinsic proteins are able to emit fluorescence light, as a result of aromatic amino acids presence (phenylalanine, histidine, tryptophan and tyrosine). On the other hand, several extrinsic fluorescent dyes offer additional possibilities for protein characterization, binding to ε-amino group, N-terminus or thiol group of cystein.

Detailed explanations about fluorescence is massively present in the literature (Lakowicz, 2006; Valeur, 2002). Briefly, when an electromagnetic radiation, usually in the ultraviolet or visible light spectrum, hits a fluorescencent dye, this molecule transits, within femtoseconds, from the ground state to higher singlet excited states. So energy loss can lead to emission of light with a longer wavelength, and therefore lower energy.

In recent years, the increasing availability of fluorescent dyes has directed researchers to development of non-invasive methodologies in diagnostic imaging field.

In this context, extracorporeal (*in vitro*) diagnostics provides a non-invasive, early, and accurate detection of the biological disease markers in the process of routine screening, thus enabling the appropriate treatment regimen to be chosen. Various nanotechnology platforms have been developed to allow the simultaneous real-time evaluation of a broad range of disease markers by non-invasive techniques (Riehemann *et al.,* 2009). Fluorescence remains one of most diffused diagnostic tools, because extremely versatile and continuously improved by new emerging techniques

Fluorescence imaging could have many advantages in diagnostic providing valuable information at the structural, functional and/or molecular level of biological markers. The strength of this technique is the ability to identify interactive regions of proteins and other molecules through the fluorescence visualization of labeled probes. Usually, antibodies were used for immunostaining and identification of targets *in vitro*. However, they are sensitive to temperature, pH and organic solvents that could denature their structure and their biological activity. Thereafter, they expose only two recognition sites on their Fab. Other works, instead, utilize purified peptides selected with phage display technique as imaging probes. These have been identified to recognize different type of tumor cells, such as breast, colon, prostate cancer (Schally *et al*, 2000), or particular targets that are expressed in neoplastic microenvironment (Zhao *et al*, 2014). After being synthesized, peptides are conjugated with radioisotopes (Sosabowski and Mather, 2006), fluorochromes or paramagnetic iron particles (Yang *et al*, 2006); they reach their target and allow the identification thanks to the tracer to which they are bonded. Peptides may be conjugated with drugs, nucleotide sequences (Flierl *et al*, 2003) and other molecules for drug and gene targeting or penetrate in the cells by carrying cytotoxic activity (Akrami *et al*, 2016).

Despite the advantages and versatility for many applications, the peptides have the same susceptibility to chemical and physical conditions of antibodies.

Using whole phages in the place of synthetic peptides allows overcoming all the limitations discussed above. In fact phages are long term stable and resistant to temperature, pH, organic solvents, denaturing agents. In contrast to peptides or antibodies, phages maintain their viability after conjugation and consequently the possibility to be recovered and if necessary propagated conveniently by amplification in host bacteria. In this way, large amounts of viral infectious particles are easier to produce with shorter and cheaper purification steps than peptides or antibodies. Particularly, M13 phage, genetically engineered on the pVIII protein, not only expose thousands of insert copies, but preserve the folding of exposing peptides on its capsid proteins. In fact, synthetic peptides alone could lose their tridimensional structure invalidating target recognition.

In some studies, labelling has been performed using entire M13 bacteriophages, which displayed peptides on PIII minor capsid protein, able to specifically recognize cancer cells (Ghosh *et al*, 2012), osteosarcoma (Sun *et al*, 2010), epithelial cell tight junctions (Herman *et al*, 2008), cells that early response to anti-angiogenic treatment (Cao *et al*, 2011).

Labelling didn't invalidate the recognition of the specific target on PIII protein, since fluorochrome reacts mainly with PVIII capsid protein. Li K. et al (2010) have used M13 bacteriophage for dual-modification: fluorescent molecules FL-NHS for bioimaging and folate-azide for giving specificity towards cancer cells overexpressing folate receptors (Li *et al*, 2010). Most of labelling procedures are complicated and time consuming, requiring long periods for phage purification from excess of reagents and fluorochromes.

Avoiding further engineering or chemical modifications of phage capsid proteins, a labelling technique, simple, reliable, cheap and rapid, has been developed using whole phagemid, without interfering on binding affinity and specificity toward cell targets. In this way, it’s obtained an efficient bioactive and bio functionalized probe for *in vitro* imaging.

This section describes an imaging approach by using specific phage probes labelled directly with fluorescein isothiocyanate (FITC). Particularly, procedures and results for fluorescence detection of bacterial pathogens, namely *P. aeruginosa*, *S. epidermidis* and *S. aureus,* and histiocytic lymphoma cells, namely U937, in liquid samples are described.
Moreover, in order to verify whether this approach could be extended in the analysis of clinical samples, EIII1 FITC-labelled clone, selected against U937 cells, has been tested versus myelomonocytic leukemia cells on blood smear.

Bacterial fluorescence imaging

Materials and Methods

Bacteria and growth media. Pathogenic bacteria *Staphylococcus epidermidis* ATCC 12228, *Staphylococcus aureus* ATCC 29213 and *Pseudomonas aeruginosa* ATCC 27853 were grown in their respective culture media to give a concentration of $2{\cdot}10^9$ CFU (Clone Forming Units) per ml. Stock organisms were maintained in LB broth (or TSB) containing 20% (v/v) glycerol at −80 °C.

Phage labelling with FITC. For fluorescence analysis, it was carried out the same procedure for 9IIIB5, StauIVS5 and P9b species-specific clones against *S. epidermidis, S. aureus* and *P. aeruginosa*, respectively. As regards the last clone, namely P9b, phage selection against its target, *P. aeruginosa*, has been previously described by Carnazza *et al* (2008).

Phage labelling with FITC was carried out according to the procedure described by Herman *et al.*, and adapted to sperimental condition of the present study (Herman *et al.*, 2008).

$1{\cdot}10^{13}$ PFU (Plaque Forming Units) were resuspended in 200 µl Buffer $Na_2CO_3/NaHCO_3$ (pH 9.2) with 5 µl of fluorescein isothiocyanate (FITC, 5mg/ml). Clones were incubated for 2 h in the dark on rotator (8 rpm) at Room Temperature (RT) to allow reaction with fluorochrome. Sample was incubated at 4 °C over night with 200 µl of PEG/ NaCl and then centrifuged at 15300 ×*g* at 4 °C for 1 h. The supernatant was discarded and the pellet resuspended in 100 µL of Tris Buffered Saline [TBS, (7.88 gr/L Tris-HCl, 8.77 gr/L NaCl)]. Labelled clones were stored in the dark at 4 °C until utilization.

Sample preparation for fluorescence imaging. Three different samples, one for pathogenic species, were prepared using the same procedure. 50 µl of cells (at a concentration about $2{\cdot}10^9$ CFU/ml) were put on Poly-L-Lysine (PLL) coated glass slides and fixed with cold absolute methanol for 10 min. Cells were washed three times with PBS and then incubated with 50 µl of FITC labelled-phage clone (titer $1{\cdot}10^{13}$ PFU/ml, cell/phage ratio 1:5000) for 1 h at 37 °C. After two washings steps in PBS and one in ultrapure water, the sample was allowed to dry in air. Wild-type vector pC89 served as negative control for evaluation of background from nonspecific binding. The samples were analyzed by a fluorescence microscope (Leica DMRE) with 63× magnification.

Results and Discussions

Labelling procedure involves a direct link between phage capsid protein and FITC amine-reactive fluorochrome. Although a loss of the bond selectivity was expected, all tested clones showed *in vitro* imaging a high binding efficiency against their specific cellular targets, according to Jaye et al., 2004.

Figure 3.1 shows *S. epidermidis* targeting by FITC-labelled 9IIIB5 clone (left) compared to insert-less vector pC89 (right).

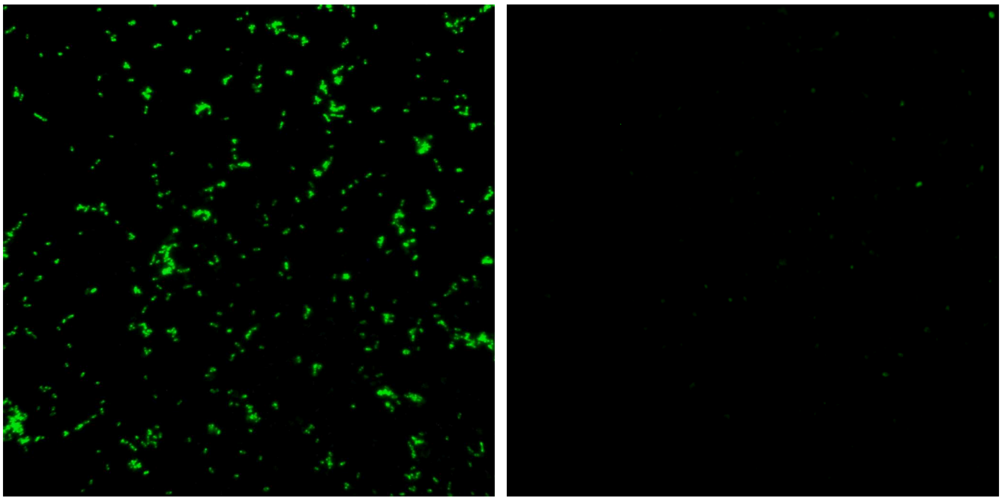

Figure 3.1 ***S. epidermidis*** **with FITC-labelled 9IIIB5 clone (left) and insert-less vector pC89 (right).**

The presence of bright fluorescence indicates that selected clone binds strongly its cell target, resisting the washing step to remove excess unbound phage. On the other hand, absence of fluorescence in the right panel of **Figure 3.1** indicates that the recognition of cell target is due to foreign peptide display on phage clone surface.

A similar result has been obtained using the *StauIVS5* phage clone against its specific target cell, namely *S. aureus* **[Figure 3.2].**

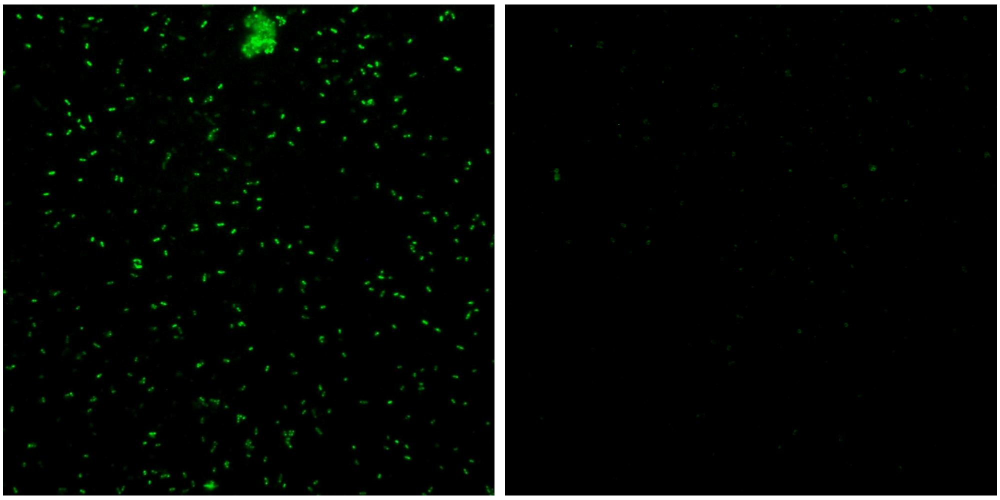

Figure 3.2 ***S. aureus*** **with FITC-labelled StauIVS5 clone (left) and insert-less vector pC89 (right).**

Like the previous case, the strong link between the clone and its target is mainly due to the presence of the foreign peptide, as confirmed by *S. aureus* sample treated with insert-less vector pC89 (right panel). However, an interesting aspect concerns reduction of cluster distribution, typical of Staphylococcus genus, present in the first case and absent in the latter. It seems, in fact, that the interaction between the clone and its cell target, affect in any way the normal fitness of bacterial growth. Studies on this aspect are still in progress.

Finally, **Figure 3.3** shows the results obtained using the P9b phage clone against its specific target cell, namely *P. aeruginosa.*

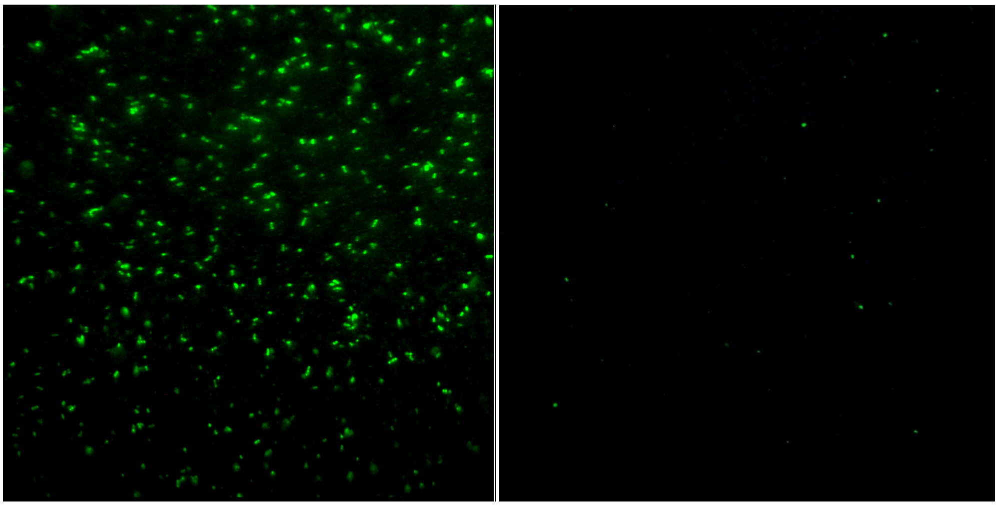

Figure 3.3 ***P. aeruginosa*** **with FITC-labelled P9b clone (left) and insert-less vector pC89 (right).**

According to previous cases, a bright fluorescence on *P. aeruginosa* cells was only obtained by using P9b selected clone. Moreover, it is known that foreign peptide bound with high avidity an outer-membrane proteins (OMPs) of *P. aeruginosa*, with a weight of 42 kDa.

The functional approach just described can be applied exploiting other fluorescent dyes. It would be possible to functionalize a given phage clone, selected for a single bacterial target, with a specific fluorochrome. In such a way, the emission of the specific fluorescence in an unknown sample will reveal the presence of the tagged bacterium.

Moreover, the use of a mixture of phage clones, each carrying its specific fluorchrome, would allow the simultaneous typing of different bacteria in a pathological sample, becoming an easy and rapid tool for multiplex target identification.

Leukaemia fluorescence imaging

Materials and Methods

Cell lines and culture conditions. U937 cell line cultured in RPMI 1640, as described in Chapter1, were maintained at cell density between 1 × 10^5 and 2 × 10^6 viable cells/mL by replacement of medium every three days.

Labelling of phage with FITC. The same procedure, described above, were used for labelling of EIII1 clones, selected against whole diffuse histiocytic lymphoma (U937) cells in suspension.

Sample Preparation for fluorescence imaging. $2 \cdot 10^5$ U937 cells were put on Poly-L-Lysine (PLL) coated glass slides and fixed with cold absolute methanol for 10 min. Cells were washed three times with PBS and then incubated with 50 µl of FITC labelled-phage clone (titer $4 \cdot 10^{10}$ PFU/ml, cell/phage ratio 1:10000) for 1h at 37 °C. After two washings steps in PBS and one in ultrapure water, the sample was allowed to dry in air. Wild-type vector pC89 served as negative control for evaluation of background from nonspecific binding. The samples were analyzed by a fluorescence microscope (Leica DMRE) with 63× magnification.

Results and Discussions

Figure 3.4 shows U937 targeting by FITC-labelled EIII1 clone (left) compared to insert-less vector pC89 (right).

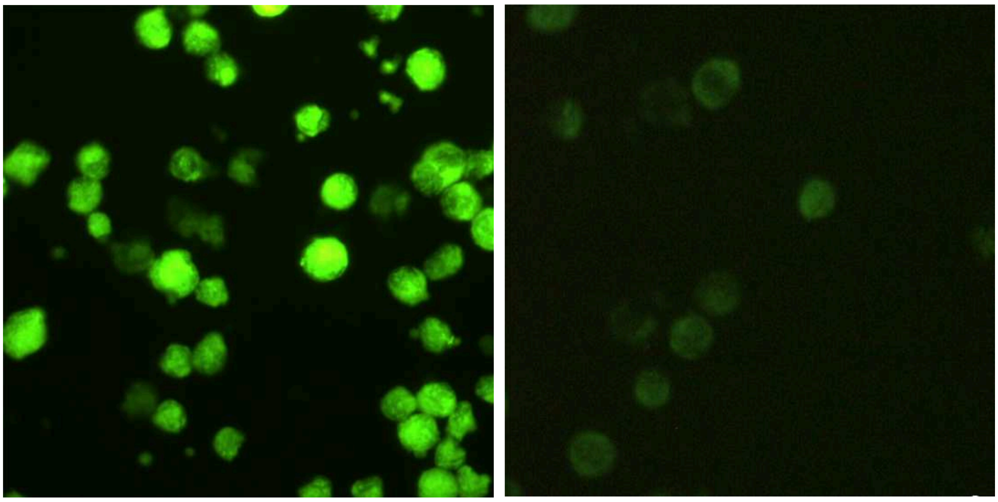

Figure 3.4 U937 cells targeting by FITC-labelled EIII1 clone, selected by a 9-mer random M13 phage display libraries. Data have been published in Biosensors and Bioelectronics (Lentini *et al*, 2015).

FITC-labelled EIII1 clone was found to specifically bind to U937, as microscopy observations revealed bright green fluorescent stained U937 cells (**Figure 3.4**). On the contrary, only background fluorescence was observed in U937 cells by using FITC-labelled pC89 (insert-less phagemid), indicating a specificity of the peptide expressed by EIII1 clone. As observed in the experiments for bacterial cells identification by fluorchrome conjugated phage clones, conjugation with FITC fluorochrome does not affect the phage clone ability to recognize the cell target. Therefore, the whole phage structure can be used as a robust and versatile probe, in which the recognition sites are contained in each copy of the major coat PVIII proteins and, consequently, homogeneously distributed on the whole phage surface.

This system could be used for discrimination of blood malignancy cells *in vitro* or *ex vivo* as, for example, on a blood smear for diagnosis.

In fact, the detection of circulating tumor cells in the blood is very useful in order not only to characterize leukaemia typologies but also for the monitoring of therapy, the control of treatment efficacy and, after the therapy, the detection of the minimal residual disease. Thereafter a probe that specifically recognizes leukemic cells could be used for gene or drug targeted therapy, which are the most promising approaches for many types of blood malignancy. Identification of blood tumor markers has progressed slowly, especially because of difficulties in isolating pure populations of cells that change continuously their molecular expression.

At this purpose, FITC-labelled EIII1 clone, selected towards U937 cell lines, was tested against a blood smear from patient affected by myelomonocytic leukaemia. The results are showed in **Figure 3.5.**

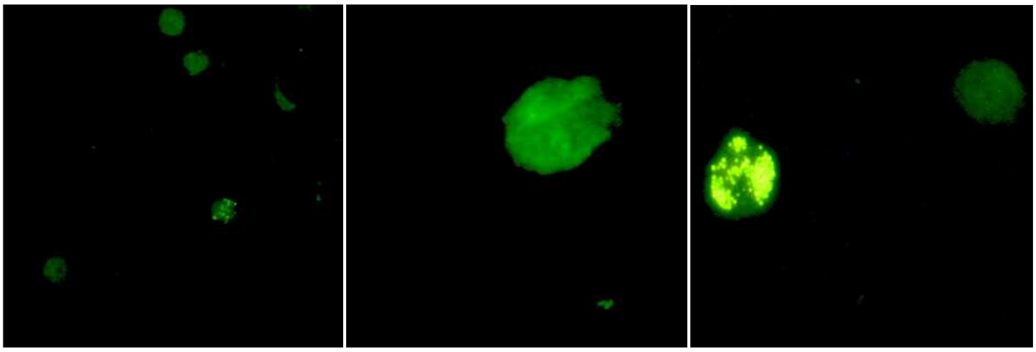

Figure 3.5 Cells targeting by FITC-labelled EIII1 clone in a blood smear from patient affected by myelomonocytic leukaemia.

Fluorescence images point out that only 5% of cellular elements were recognized by FITC-labelled EIII1 clone. However, images revealed that FITC-labelled EIII1 clone stained cells in two distinct ways. In the first, staining was homogeneously distributed on the whole cell surface, as observed in U937 cells. On the contrary, in other cells staining was not homogeneous, but localized in distinct inner regions of the cell and appeared very bright.

Moreover, different intensities of staining could be observed. Such images indicate that the cell molecular target is unevenly distributed inside the cells and its expression is not constant (**Figure 3.6**). It is known that cell phenotype can be arranged during cell lifecycle, in dependence of the physiological stage, and during the different steps of cell differentiation.

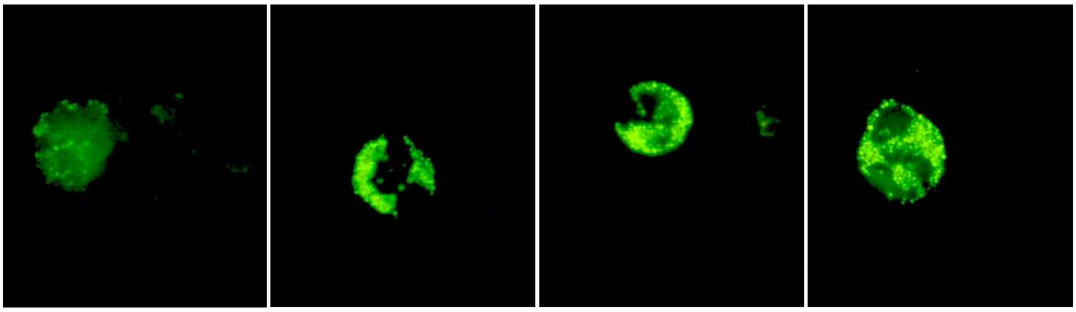

Figure 3.6 Unevenly distribution of molecular targets recognized by FITC-labelled EIII1 clone.

The cell line U937 is a precursor of monocytes and varies almost completely its antigenic profiles during the differentiation. It is likely that the 5% of cellular elements recognized by FITC-labelled EIII1 clone share at least one of the molecular targets present in U937, probably because they derive from the same lineage.

The data indicate that the proposed approach may be applied for diagnosis in blood malignancies, however it has to be implemented with other phage clones, able to identify a more significant number of cells present in the sample.

Acknowledgements

This activity was partially funded by Italian Ministry of Education, University and Research (MIUR) by means of the national Program PON R&C 2007–2013, project project HIPPOCRATES – Development of Micro and Nano-Technologies and Advanced Systems for Human Health (PON02_00355_29641931).

The activity "**Leukaemia fluorescence imaging**" was carried out in collaboration with:

Doctor A. Allegra and Professor C. Musolino, Division of Hematology, Department of General Surgery, Pathological Anatomy and Oncology, University of Messina, Italy.

Bibliography

Akrami M, Balalaie S, Hosseinkhani S, Alipour M, Salehi F, Bahador A, Haririan I. Tuning the anticancer activity of a novel pro-apoptotic peptide using gold nanoparticle platforms. 2016. Scientific Reports 6:31030.

Cao Q, Liu S, Niu G, Chen K, Yan Y, Liu Z, Chen X. Phage display peptide probes for imaging early response to bevacizumab treatment. 2011. Amino Acids. 41, 1103–11.

Carnazza S, Foti C, Gioffrè G, Felici F, Guglielmino SPP. Specific and selective probes for Pseudomonas aeruginosa from phage-displayed random peptide libraries. 2008. Biosens. Bioelectron. 23, 1137–44.

Flierl A, Jackson C, Cottrell B, Murdock D, Seibel P, Wallace DC. Targeted Delivery of DNA to the Mitochondrial Compartment via Import Sequence-Conjugated Peptide Nucleic Acid. 2003. Molecular Therapy 7, 50-57.

Ghosh D, Kohli AG, Moser F, Endy D, Belcher AM. Refactored M13 Bacteriophage as a Platform for Tumor Cell Imaging and Drug Deliver. 2012. ACS Synth Biol. 1, 576-82.

Herman RE, Makienko EG, Prieve MG, Fuller M, Houston MEJr, Johnson PH. Phage Display Screening of Epithelial Cell Monolayers Treated with EGTA: Identification of Peptide FDFWITP that Modulates Tight Junction Activity. Journal of Biomolecular Screening 12, 1092-101.

Jaye DL, Geigerman CM, Fuller RE, Akyildiz A, Parkos AJ. Direct fluorochrome labeling of phage display library clones for studying binding specificities: applications in flow cytometry and fluorescence microscopy. 2004 Immunol. Methods. 295, 119-27.

Lakowicz JR. Principles of fluorescence spectroscopy. 2006. Analytical Chemistry 3rd edition Springer.

Li K, Chen Y, Li S, Nguyen HG, Niu Z, You S, Mello CM, Lu X, Wang Q. Chemical Modification of M13 Bacteriophage and its application in cancer cell imaging. 2010 Bioconjug Chem 21, 1369-76.

Lentini G, Fazio E, Calabrese F, De Plano LM, Puliafico M, Franco D, Nicolò MS, Carnazza S, Trusso S, Allegra A, Neri F, Musolino C, Guglielmino SPP. 2015. Phage-AgNPs complex as SERS probe for U937 cell identification. Biosens. Bioelectron. 74, 398–405.

Schally AV, Comaru-Schally AM, Plonowski A, Nagy A, Halmos G, Rekasi Z. Peptide analogues in the therapy of prostate cancer. 2000. Prostate 45, 158–66.

Sosabowski JK, Mather SJ. 2006. Conjugation of DOTA-like chelating agents to peptides and radiolabeling with trivalent metallic isotopes. Nat Protoc. 1(2), 972-6.

Sun, X, Niu G, Yan Y, Yang M, Chen K, Ma Y, Chan N, Shen B, Chen X. Phage display-derived Peptides for osteosarcoma imaging. 2010. Clin. Cancer Res. 16, 4268-77.

Riehemann K, Schneider SW, Luger TA, Godin B, Ferrari M, Fuchs H. Nanomedicine--challenge and perspectives. 2009. Angew. Chem. Int. Ed. 48, 872 – 97.

Valeur B. Molecular fluorescence: Principles and applications. 2002. Photochemistry 2rd edition Wiley-VCH.

Yang L, Mao H, Cao Z, Wang A, Peng X, Wang X, Karna P, Adams G, Yuan Q, Staley C, Wood WC, Nie S, Gao X. Development of peptide conjugated Superparamagnetic Iron Oxide (SPIO) Nanoparticles for Targeted MR Imaging and Therapy of Pancreatic Cancer. 2006. NSTI-Nanotech 2, 17-20.

Zhao Y, Ji T, Wang H, Li S, Zhao Y, Nie G. Self-assembled peptide nanoparticles as tumor microenvironment activatable probes for tumor targeting and imaging. 2014. J Control Release. 177, 11-9.

CHAPTER 4

Phage-based capture and concentrating system for single step detection of pathogens

Introduction

One of the most encountered problems in diagnostics is the efficient detection of an analyte when present at low concentration in a clinical specimen. For this purpose, techniques for separation and concentration of the analyte (molecules or cells) in a smaller volume are a prerequisite for any efficient detection procedure.

Several optical biosensors have been proposed for detection of biomolecules and pathogens in biological samples. In this field, paramagnetic beads have assumed considerable importance because of their easy use and greater surface/volume ratio compared to a flat surface. Several authors reported the use of paramagnetic particles for identification of viruses and bacteria in food, water, environmental or biological samples (Wei *et al*, 2012; Sen *et al*, 2011; Zhu *et al*, 2011). These systems usually consist in an immune-magnetic sandwich assay in which two antibodies are required: the one for beads coating and the other, usually conjugated with fluorophores or enzymes, for target identification. As alternative to antibodies, many researchers use peptides coupled to paramagnetic beads (Ciocchini *et al*, 2013). However, both antibodies and peptides are sensitive to environmental physicochemical variations, as previously discussed in Chapter 1. Moreover, their large scale production and purification are expensive and time-consuming and in most cases they are not reusable.

This section describes a phage-based capture and concentrating system for single step detection of pathogens in liquid samples.

Particularly, the following describes procedures and results for optical detection of bacterial pathogens, namely *Pseudomonas aeruginosa*, *Staphylococcus epidermidis* and *Staphylococcus aureus.* Selective phage clones, namely P9b, StauIVS5 and 9IIIB5, were used to coat commercial beads with different characteristics (materials, size, chemical functionalization). The phage-coated beads were able to recognize and bind the bacterial targets.

Materials and Methods

Bacteria and growth media. *S. epidermidis* ATCC 12228, *S. aureus* ATCC 29213 and *P. aeruginosa* ATCC 27853 were grown in their respective culture media. Stock organisms were maintained in LB broth (or TSB) containing 20% (v/v) glycerol at −80 °C.

Functionalization of beads. Functionalization procedure was optimized on different beads, namely Latex beads Servant (Ø 0.8µm), Paramagnetic Dynabeads® Tosylactivated (Ø 2.8µm), Paramagnetic ScreenMAG-Carboxyl (Ø 1µm) and Paramagnetic ScreenMAG-Amine (Ø 1µm) beads.

Beads functionalization included two procedure variations related to the functional groups exposed on bead surface.

About Paramagnetic Dynabeads® Tosylactivated, the bond with phages occurs directly through the sulphuric or amino groups of the peptide displayed on the phage.

In this case, functionalization protocol is the following:

> According to the manufacturer protocol, 0.1 mg of beads was washed twice with 1 ml of Borate buffer (pH 9.0) with the aid of a rotator (8 rpm). The beads were resuspended in Borate Buffer. Phage were concentrated by centrifugation with PEG-NaCl at 15300 *xg* at 4° C (Eppendorf 5147R), resuspended in ultrapure water and added to the beads. The tubes were incubated in a rotator (8rpm) for 24h at 40 °C. The supernatants were recovered for titration of unbound phages. Phage-coated beads were washed three times with Phosphate Buffer Saline (PBS, pH 7.1) and resuspended in PBS + 4% Bovine Serum Albumin (BSA) in order to block any residual uncovered site on their surface.

About Paramagnetic ScreenMAG-Carboxyl, Paramagnetic ScreenMAG-Amine and Latex beads Serva, functionalization protocol includes a variant with 2-(N-Morpholino) EthanelSulfonic acid buffer (MES, pH 6.0) and 1-Ethyl-3[3-Dimethylaminopropyl] Carbodiimide (EDC).

In this case functionalization protocol is the following:

> According to the manufacturer protocol, 0.1 mg of beads was washed twice with 1 ml of MES buffer (pH 6.0) with the aid of a rotator (8 rpm) and a magnetic separator. The beads were resuspended in 100 µl MES + 1 mg of EDC. Phage were concentrated by centrifugation with PEG NaCl at 15300 *xg* at 4 °C (Eppendorf 5147R) and resuspended in ultrapure water. Phages were

concentrated by centrifugation with PEG NaCl at 15300 *xg* at 4 °C (Eppendorf 5147R), resuspended in ultrapure water and added to the beads. The tubes were incubated in a rotator (8 rpm) for 2h at Room Temperature (RT). The supernatants were recovered for titration of unbound phage. Beads were washed three times with Phosphate Buffer Saline (PBS, pH 7.1) and resuspended in PBS + 4% Bovine Serum Albumin (BSA) in order to block any residual uncovered sites on their surface.

The size of the beads has been investigated to evaluate its spatial relation with phage dimension in the efficiency of bead coating. In fact, surface availability and phage steric hindrance have to be finely tuned to achieve a good and homogeneous distribution of phages on the bead surface.

At this purpose, all beads, previously considered, were tested with different phage concentrations, namely 336 Phage/Bead (Ph/B), 168 Ph/B, 101 Ph/B, 34 Ph/B.

ELISA assay on beads surface. In order to verify phage coating of the beads, an ELISA assay has been performed. 20 µl of beads functionalized with the different phage concentrations, and 20 µl of the respective negative controls, were normalized by Optical Density (OD_{620}) measurement and washed three times with Washing Buffer (PBS + 0.05% Tween 20). 250 µl of anti-M13 major coat protein PVIII-HRP monoclonal conjugate (1:5000 diluted in PBS + 0.1% BSA + 0.5% Tween 20) were added. After 1h of incubation at 37 °C and three washing steps, reactions were developed with 250 µl of 3,3',5,5'- TetraMethylBenzidine (TMB), Horse Radish Peroxidase (HRP) substrate, for 20 min in the dark, stopped with HCl 2N and read at 450 nm in Multiscan FC (Thermo Scientific Type: 357).

Capture Tests with pathogens. Capture tests were performed by incubating beads functionalized with different Phage/Bead ratios with each pathogen (10^3 cells/ml) in PBS (pH 7.1; 1 ml) for 15 min at RT on a rotator mixer operating at 8 rpm.

Gold Standard determination of capture efficiency. The efficiency of capture was assessed by Standard Plate Count. After capture, the supernatants were recovered, and uncaptured bacteria were enumerated by spread plating on LB agar plates followed by incubation overnight at 37 °C. Colony Forming units per millilitre (CFU/ml) counts were determined before and after beads incubation with bacteria and the capture efficiency percentage was calculated. Tests were performed in triplicate and results were reported as percentage average of capture.

Direct Detection of Captured Bacteria. Depending on the bead nature, paramagnetic or latex, two detection procedures have been be used.

About paramagnetic beads, detection were carried out by use of beads conjugated with a fluorophore, such as Rhodamine wavelength 6G (wavelength excitation 526 nm, wavelength emission 555 nm) and an unspecific fluorophore, indicating presence of captured bacteria into the beads aggregates.

Protocol is the following:

After capture, paramagnetic beads were recovered with magnetic separator on a circular coverslip placed on the cap of the reaction tube and incubated with a solution of DAPI blue fluorescent nucleic acid stain (1µg/ml of ultrapure water; wavelength excitation 350 nm, wavelength emission 460 nm) for 5 min, or with SYTO9 green fluorescent nucleic acid stain (3.34 mM; Molecular Probes; wavelength excitation 485 nm, wavelength emission 498 nm) for 15 min. Then they were washed once to remove the excess of fluorochrome and observed under LEICA DMRE fluorescence microscope with Leica C Plan 63× objective.

About latex beads, detection was carried out by agglutination test. In this case, the protocol is the following:

$1.8 \cdot 10^8$ phage-functionalized latex beads were dispensed in each well of a glass slide containing decimal dilutions of bacterial suspension and incubated for 5 min at RT in a horizontal shaker.

Indirect Detection of Captured Bacteria Detection can also carried by visible micro-Raman spectroscopy or multiplex-PCR assay.

About visible micro-Raman spectroscopy, procedures, described in Chapter 2, have to take into account the appearance of new bacterial spectral features arising from interactions with phage-coated beads. A more detailed explanation is provided in the Results and Discussions section. Furthermore, to quantify the reproducibility and specificity of the experimental data, the output signals are pre-processed and used for the construction of barcodes, specific for each strain considered. According to Patel *et al* (2008), second derivative of the Raman spectra were calculated using the same Savitzky-Golay routine developed for smoothing. Binary arrays, i.e. the barcodes, were obtained setting to 1 the spectral points at which a down curvature was detected, and setting to 0 the spectral point showing an up curvature. An empirically determined edge value for second order derivative was used as a zero point assignment. Data treatments were performed using custom scripts written in Matlab©.

About multiplex-PCR, this assay allows the detection of DNA of pathogens simultaneously present in the same sample by using species-specific primers in the same reaction mixture. With a single reaction, it is possible to detect and distinguish the captured bacteria within a few hours.

After bacterial capture by phage-coated beads, three pairs of primers, specific for *S. aureus*, *S. epidermidis*, *P. aeruginosa*, were used in a multiplex polymerase chain reaction.

The complementation and hairpin structure and the primer specificity were checked by analysis in Basic Local Alignment Search Tool (http://blast.ncbi.nlm.nih.gov/Blast.cgi) and in Amplification Silico PCR (http://insilico.ehu.es/PCR/).

Primers used in this work are reported in **Table 4.1**

Strains	**Gene target**	**Primer sequences (fw-rev)**	**Amplicon size (bp)**	**References**
P. aeruginosa	algD GDP mannose dehydrogenase	**5'**-TTCCCTCGCAGAGAAAACATC-**3'** **5'**-CCTGGTTGATCAGGTCGATCT-**3'**	520	da Silva *et al*, 1999.
S. aureus	Thermostable nuclease A	**5'**-GCGATTGATGGTGATACGGTT- **3'** **5'**-AGCCAAGCCTTGACGAACTAAAGC-**3'**	279	Shortle, 1983.
S.epidermidis	Encodes a recombination/ repair protein	**5′-** CAGTTAATCGGTATGAGAGC-**3′** **5′-**CTGTAGAGTGACAGTTTGGT-**3'**	219	Iorio *et al*, 2011.

Table 4.1 Species-specific primers and related amplicon size for *P. aeruginosa*, *S. aureus*, *S. epidermidis*.

The amplification was performed on a Thermal Cycler (MyCycler^{TM} ThermoCycler,Bio-Rad) using 50 µl of reaction mixture, containing 10 µl of captured bacteria as template, 1.25 U of Taq Hs DNA polymerase (Bioline, UK) and 0.2 µM of each primers (1 µM of the primers algD, 1 µM of the primers nucA, 1 µM of the primers recN) and 1X reaction buffer. Amplification conditions were the following: denaturation for 10 min at 95 °C, followed by 40 cycles of 95 °C for 30s, 60 °C for 30s, 72 °C for 90s, with final extension at 72 °C for 7 min. Amplified products were analyzed by 2% of agarose gel electrophoresis stained with ethidium bromide and visualized on UV transilluminator.

Results and Discussions

Figure 4.1 shows avidity in the time of specific phage clone against bacteria target.

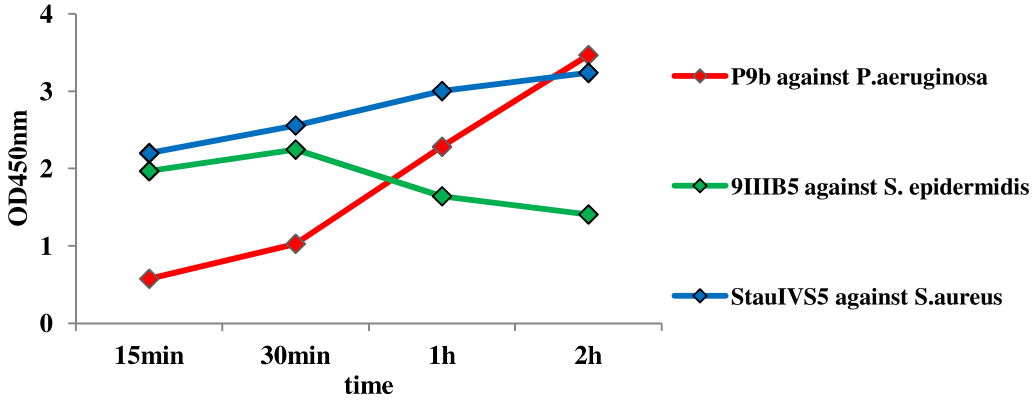

Figure 4.1 kinetic phage-capture ELISA of specific phage clone against bacteria target.

In kinetic phage-capture ELISA assay each organism was incubated at different times, 15 min, 30 min, 1 h and 2 h, with an equal amount of each specific phage, and bound phages were detected by using anti-M13 peroxidase conjugate antibody and then TMB substrate colour development.

In particular, data showed the following: P9b clone avidity increased linearly throughout the time; StauIVS5, the specific clone to *S. aureus*, showed a high level of avidity at 15 min, which progressively increased during the time; finally, 9IIIB5 avidity increased within 30 min, then declined progressively.

After avidity tests, each clone was separately used to functionalize beads.

In order to verify phage coating of the beads, ELISA assay was performed using an anti-pVIII monoclonal antibody-HRP (horseradish peroxidase) conjugates. **Figure 4.2** show data of phage coating for all considered beads.

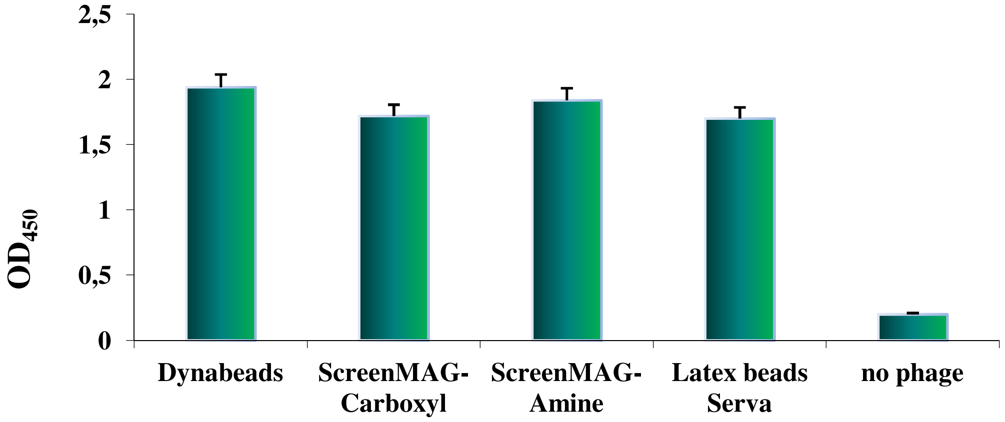

Figure 4.2 ELISA assay on phage-coated beads.

Despite the differences in bead reactive groups involved in phage binding there are no significant differences of beads coating.

The optimal Ph/B ratio for optimal beads coating was 168 (beads diameter 0.8 and 1 um) and 1300 (beads diameter 2.8 um) **(Figure 4.3)**.

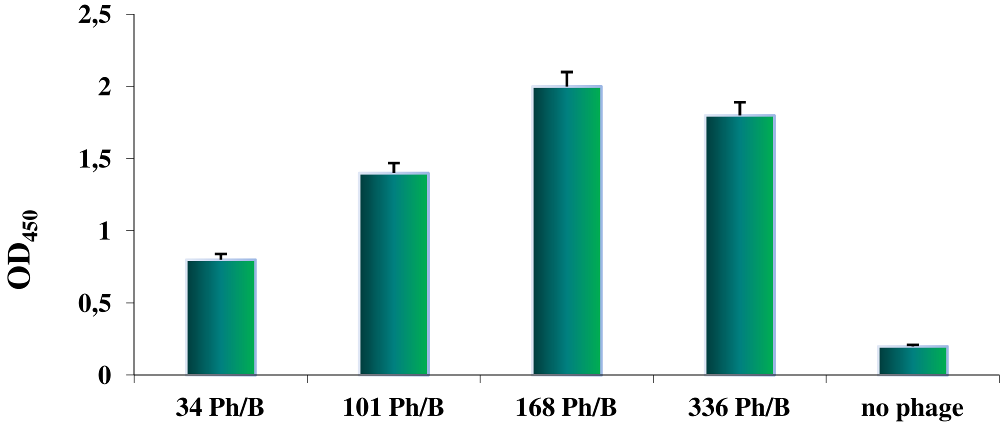

Figure 4.3 ELISA assay on phage-coated beads with different phage concentrations.

The coating increased linearly up to a threshold after which clones probably overlap among them. As an example, ELISA test results of different Ph/B ratios used for coating of Commercial paramagnetic beads ScreenMAG-Amine with phage clone P9b are grafically presented in **Figure 4.3**.

Muzard *et al* (2012) described strategies to modify M13 bacteriophages for the coating of superparamagnetic microparticles as a system for large scale immune-separation. The most convenient method reported for phage assembly to the beads was the end-on attachment using genetically engineered pIII proteins, since chemical modifications of the pVIII proteins resulted in some loss of functionality, though producing the highest coverage with the simplest strategy.

Results show instead that M13 phage bound covalently to groups exposed on paramagnetic/latex beads, without need to neither engineer capsid protein nor introduce affinity system. Data were confirmed by capture efficiency results **Figure 4.4**.

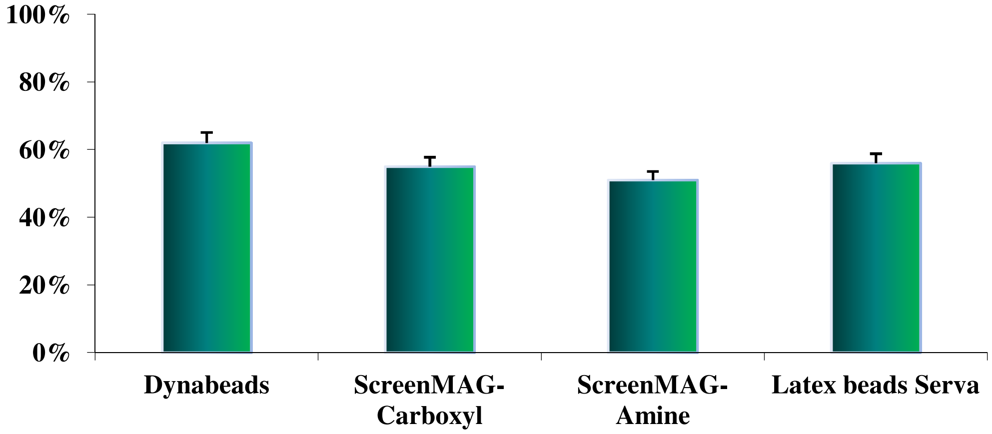

Figure 4.4 ELISA assay on phage-coated beads for capture efficiency evaluation.

Capture tests were performed by incubating phage-coated beads with bacteria for 15 min at RT. The capture efficiency was first assessed by Standard Plate Count. Colony Forming units per milliliter (CFU/ml) counts were determined before and after beads incubation with bacterial suspensions and the capture efficiency was expressed as percentage (**Figure 4.4**).

For the assessment of the limit of detection (LOD), a suspension of 10^3 bacteria was used with dilutions of functionalized beads ranging from 10^7 to 10 using Standard Plate Count. Tests were performed in triplicate and results were averaged and reported as percentage of capture. The lowest cell concentration that was considered positive was 10^2 CFU/ml for all tested bacteria, whereas the concentration of 10^6 beads allowed the optimal capture.

In **Figure 4.5** an agglutination test with phage-functionalized carboxylated blue latex particles against *P. aeruginosa* is shown.

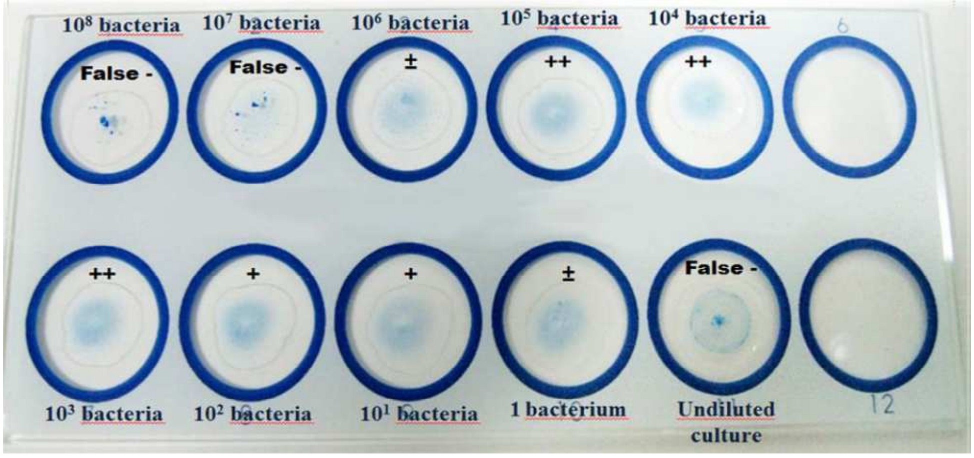

Figure 4.5 Agglutination test with phage-functionalized carboxylated blue latex particles against *P. aeruginosa.* Data have been published in XVIII AISEM Annual Conference (Calabres *et al*, 2015).

Results showed that agglutination behavior proceeded linearly as function of bacterial concentrations (**Figure 4.5**), demonstrating that phages covalently bonded to beads were able to capture target bacteria.

Similar results have been obtained with paramagnetic fluorescent beads **(Figure 4.6)**.

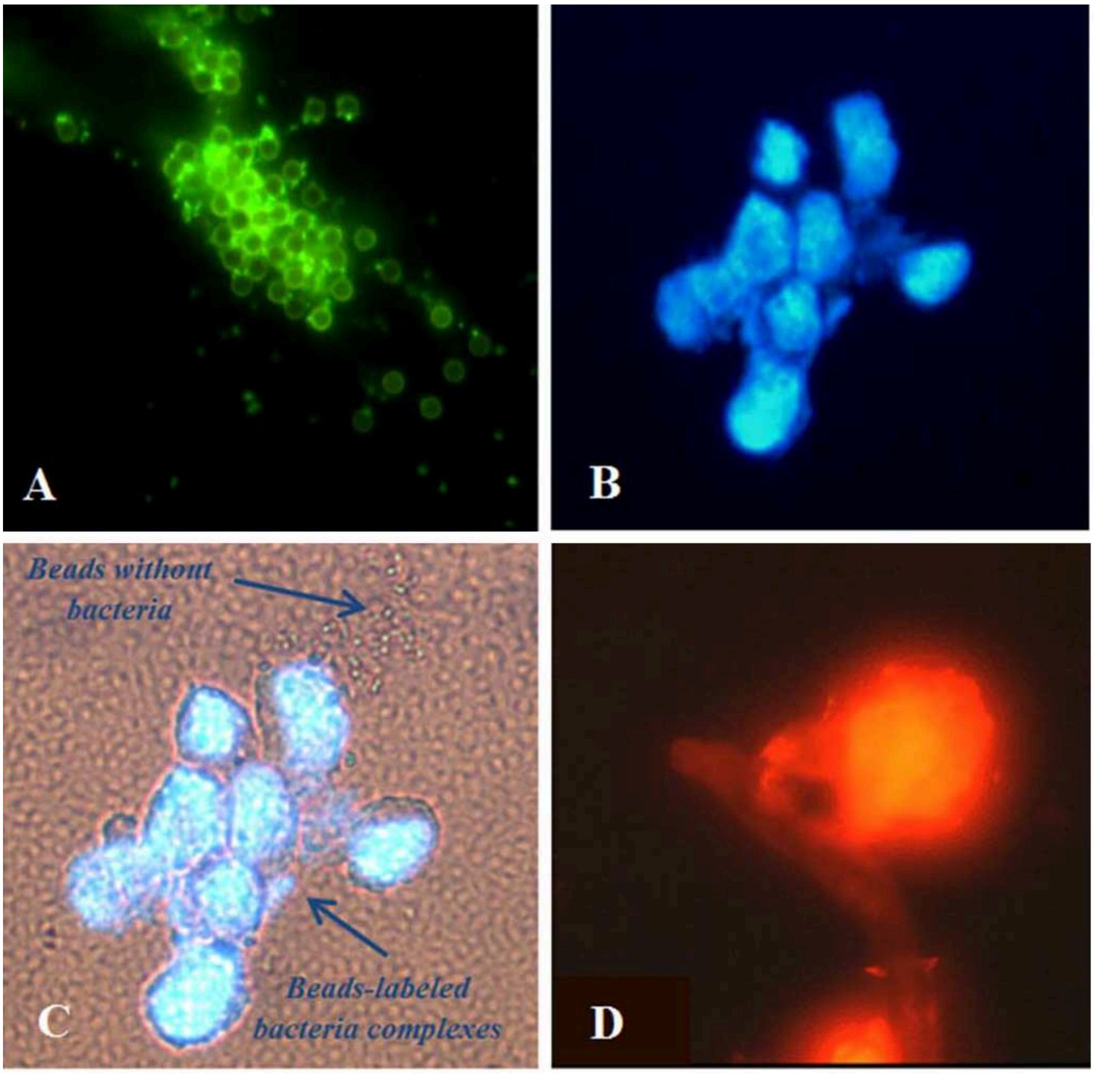

Figure 4.6 Brilliant fluorescent complexes of *P. aeruginosa* captured by phage-coated paramagnetic beads. Images represent aggregates stained with Syto9 (A) or DAPI (B, C) and bright orange fluorescence of beads excited at 526 nm (D). Data have been published in XVIII AISEM Annual Conference (Calabres *et al*, 2015).

After incubation with phage-coated beads, captured *P. aeruginosa* cells were stained with SYTO9 (**Figure 4.6 A**) or DAPI (**Figure 4.6 B and C**) fluorescent dyes for DNA, then were visualized under a LEICA fluorescence microscope. The observation of SYTO9- or DAPI-stained fluorescent aggregates (**Figure 4.6 A and B**) indicated that bacterial cells were efficiently captured by phage-coated beads.

The paramagnetic beads used in the experiment have a core stained with Rhodamine 6G, and if excited at 526 nm they emit a bright orange fluorescence (**Figure 4.6 D**). Then, since paramagnetic beads conjugated with a wide range of fluorochromes are commercially available **Figure 4.7**, it is possible to coat a single fluorochrome-conjugated bead with a specific phage clone. In this way, the specific fluorescence emitted by the beads present in the aggregates will allow the identification of a single bacterial species in a given sample.

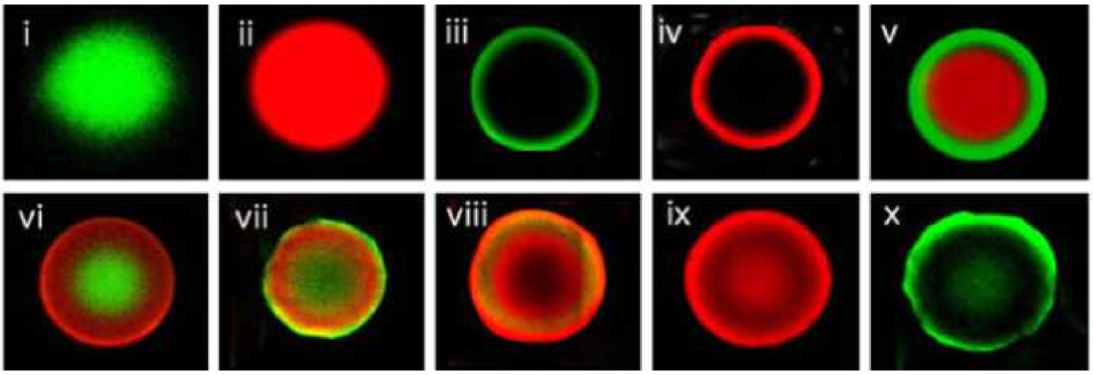

Figure 4.7 Paramagnetic beads conjugated with several fluorochromes.

Since the specificity of recognition is guaranteed by selectivity of the phage clone coated on the beads surface, the proposed system could be used for the simultaneous typing of different bacteria in a pathological sample, becoming an easy and rapid tool for multiplex target identification.

However, microscopy analysis is not a procedure that can be easily automated, so when a high number of samples have to be analyzed, a more adequate technique is needed. Detection by visible micro-Raman spectroscopy represents a rapid and effective alternative to the previously proposed methods. In this case methodology has to take into account the appearance of new bacterial spectral features arising from interactions with phage-coated beads. In **Figure 4.8** Raman measurements carried out on *P. aeruginosa* and complex P9b-coated beads/ *P. aeruginosa* cells are shown.

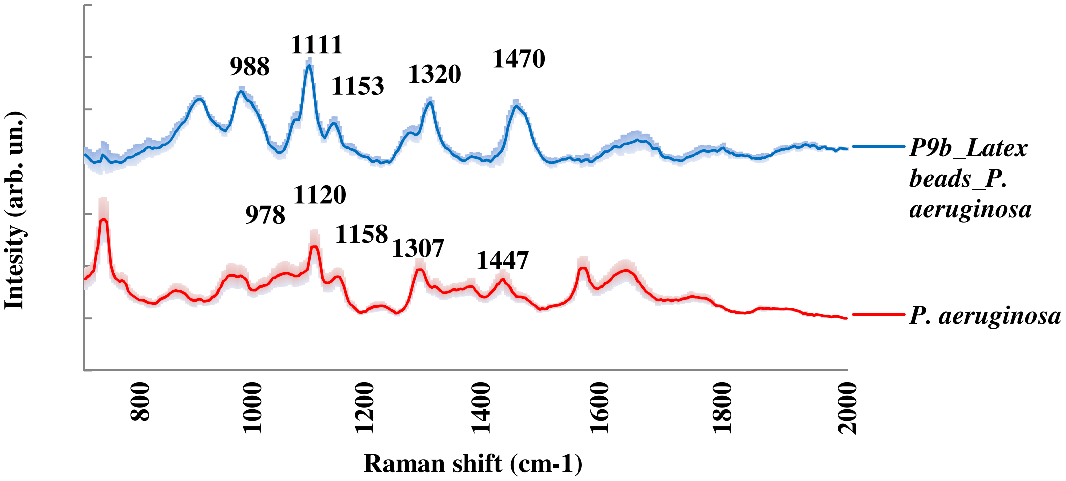

Figure 4.8 Raman spectra of *P. aeruginosa* and complex P9b-coated beads/ *P. aeruginosa*.

New Raman contributions beside significant changes in the peaks profile are identified. These changes mainly involve the stretching modes of carbohydrates, the C-C or C-O stretching modes of phospholipids, the stretching modes of proteins and the CH_2 bending and CH_3 rocking modes in the 700–1080 cm^{-1} spectral range (Rehman *et al,* 2012). Particularly, Raman peaks at 978, 1120, 1158, 1307 and 1447 cm^{-1} observed from *P. aeruginosa* were shifted at 998, 1111, 1153, 1320 and 1470 cm^{-1}, respectively. These changes are a clear indication of modifications of the structures of the bacterial cells that interact with phage through the engineered peptides displayed on the phage surface (Kengne-Momo *et al*, 2012). As consequence, in order to use micro Raman spectroscopy in rapid identification of bacteria bound to phage-coated beads, an extensive research about new bacterial spectral features is necessary to build a new database that can be used as a public tool for professionals and researcher involved in pathogen detection.

Furthermore, to quantify the reproducibility and specificity of the experimental data, the output signals are pre-processed and used for the construction of barcodes, specific for each strain considered.

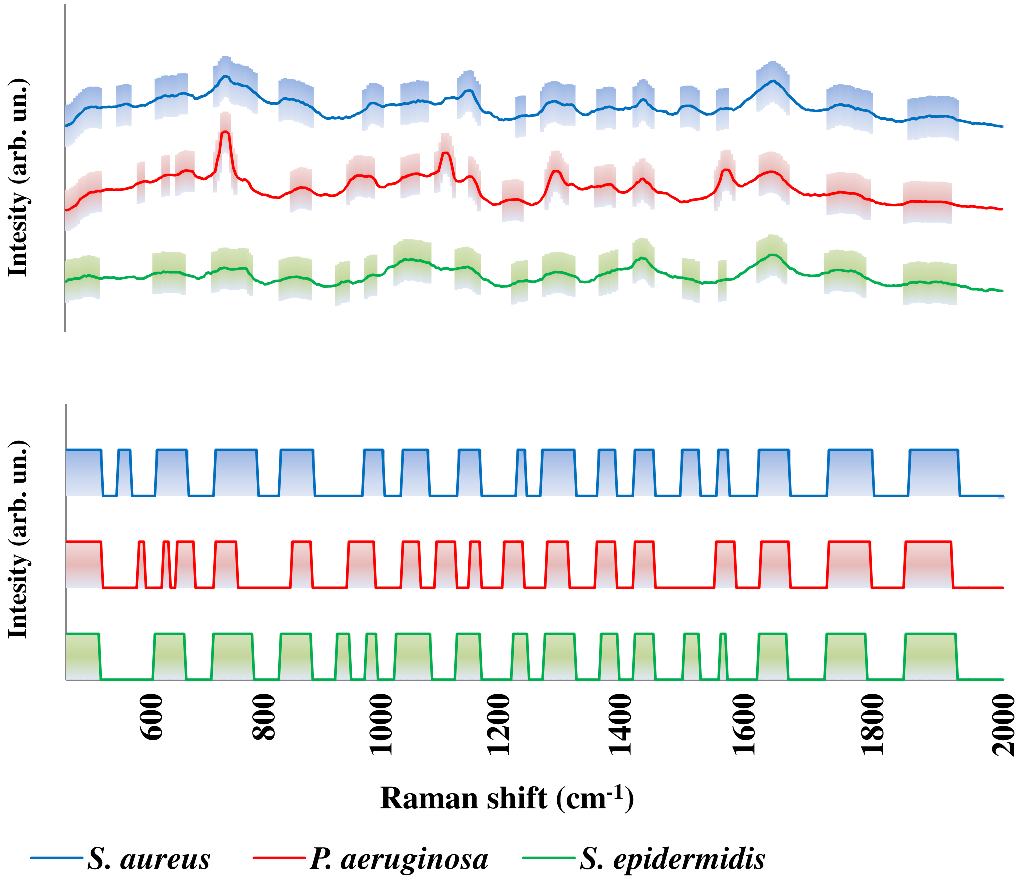

Figure 4.9 Raman spectra and relative barcodes of the three captured microorganisms used for this study (*S. aureus, S. epidermidis* and *P. aeruginosa*).

As previously described, spectra represent a fingerprint for the rapid identification of the different bacterial species. Therefore, the barcodes thus obtained constitute the analysis software database that can be used for the identification of unknown samples.

This innovative approach, based on the combination of phage display technology and micro-Raman spectroscopy, can be used to capture, concentrate and rapidly detect different bacterial strains present in a biological sample.

Sensors prepared with phage as probes could be an effective analytical method for detecting and monitoring quantitative changes of bacterial agents in a various applications including clinical based diagnostics and possibly biological warfare applications. The sample testing process, including data acquisition, required 30 min. The Raman spectra of each bacterium are highly specific because each microorganism has a unique spectral pattern, which is the result of the vibrational information obtained from macromolecules of the bacterial cell.

The proposed system is an alternative diagnostic tool that enables a rapid, high sensitive and specific one-step detection of the bacteria involved in sepsis. Although this study is a proof of concept of an innovative platform for the detection of *S. aureus, S. epidermidis,* and *P. aeruginosa*, such method can be virtually extended and applied to detection of other causes of bacterial sepsis.

Finally, *S. aureus, S. epidermidis,* and *P. aeruginosa* cells, captured by phage-coated beads, were also subjected to multiplex PCR, following the procedure described in Materials and Methods Section. In particular, the reaction has been performed on samples containing both the single and the three bacterial species mixed together **(Figure 4.10).**

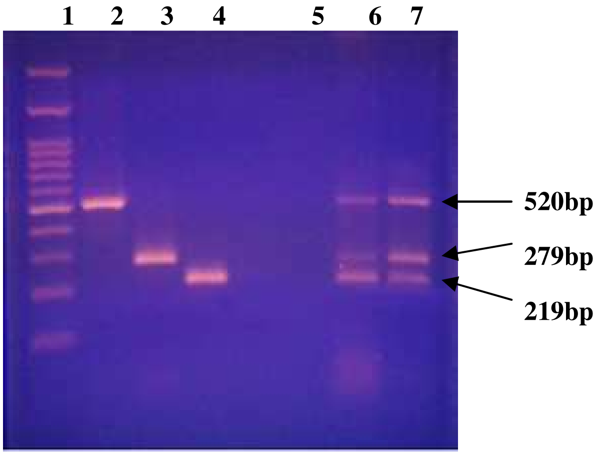

Figure 4.10 Bacterial identification using the multiplex PCR system. Lane 1: Marker (100-3000bp); Lane 2: amplicon algD for *P. aeruginosa* (520bp); Lane 3: amplicon nucA for *S. aureus* (279bp); Lane 4: amplicon recN *Staphylococcus epidermidis* (219bp); Lane 5: Mulitplex Negative control; Lane 6: Mulitplex Positive control; Lane 7 Multiplex by bacterial species mixed together . All bacteria were tested at a concentration of 10^3 batteri/ml.

PCR is a widespread molecular biology technique which is used in diagnostics laboratory as a tool for routinely pathogen identification. Also in such case, the use of phage-coated beads for pathogen capture from any kind of sample may be an interesting implementation in rapid bacterial identification by PCR standard procedure.

Acknowledgements

This activity was partially funded by Italian Ministry of Education, University and Research (MIUR) by means of the national Program PON R&C 2007–2013, project project HIPPOCRATES – Development of Micro and Nano-Technologies and Advanced Systems for Human Health (PON02_00355_29641931).

XploRA Raman spectrometer was a kind gift of A.B.A.L. onlus Messina (Italy) (http://www.abalmessina.it).

The activity of "**Bacterial detection by visible micro-Raman spectroscopy**" was carried out in collaboration with:

Doctor E. Fazio and Professor F. Neri Department of Mathematical and Computational Sciences, Physical Science and Earth Science (MIFT), University of Messina, Italy.

Doctor S. Trusso Institute of Chemical-Physical Processes (IPCF)-CNR Messina, Italy.

Bibliography

Calabrese F, Carnazza S, De Plano LM, Lentini G, Franco D, Guglielmino SPP. Phage-coated paramagnetic beads as selective and specific capture system for biosensor applications. 2015. XVIII AISEM Annual Conference 1-4.

Ciocchini AE, Rey Serantes DA, Melli LJ, Iwashkiw JA, Deodato B, Wallach J, Feldman MF, Ugalde JE, Comerci DJ. Development and validation of a novel diagnostic test for human brucellosis using a glyco-engineered antigen coupled to magnetic Beads. 2013. PLoS Negl. Trop. Dis. 7, 1-11.

Da Silva Filho LVF, Levi JE, Bento CNO, Da Silva Ramos SRT, Rozov T. PCR identification of Pseudornonas aeruginosa and direct detection in clinical samples from cystic fibrosis patients. 1999. J. Med. Microbiol. 48, 357-61.

Iorio NLP, Azevedo MB, Frazão VH, Barcellos AG,Barros EM, Pereira EM, de Mattos CS, dos Santos KRN. Methicillin-resistant Staphylococcus epidermidis carrying biofilm formation genes: detection of clinical isolates by multiplex PCR. 2011 International Microbiology 14, 13-17.

Kengne-Momo RP, Daniel P, Lagarde F, Jeyachandran YL, Pilard JF, Durand-Thouand MJ, Thouand G. Protein Interactions Investigated by the Raman Spectroscopy for Biosensor Applications. 2012. Int. J. Spectrosc. 7.

Muzard J, Platt M, Lee GU. M13 Bacteriophage-activated superparamagnetic beads for affinity separation. 2012. Small, 8, 2403–11

Patel IS, Premasiri WR, Moir DT, Ziegler LD. Barcoding bacterial cells: a SERS based methodology for pathogen identification. 2008. J. Raman Spectrosc. 39, 1660–72.

Rehman IU, Movasaghi Z, Rehman S. 2012. Series in Medical Physics and Biomedical Engineering, CRC Press; A Taylor and Francis Book.

Sen A, Harvey T, Clausen J. A microsystem for extraction, capture and detection of E-Coli O157:H7. 2011. Biomed. Microdevices, 13, 705-15.

Shortle, D. A genetic system for analysis of staphylococcal nuclease. 1983. Gene 22,181-89.

Wei B, Li F, Yang H, Yu L, Zhao K, Zhou R, Hu Y. Magnetic beads-based enzymatic spectrofluorometric assay for rapid and sensitive detection of antibody against ApxIVA of Actinobacillus pleuropneumoniae. 2012 Biosens. Bioelectron. 35, 390-93.

Zhu P, Shelton DR, Li S, Adams DL, Karns JS, Amstutz P, Tang C-M. Detection of E. coli O157:H7 by immunomagnetic separation coupled with fluorescence immunoassay. 2011. Biosens. Bioelectron., 1, 337-41.

CHAPTER 5
Selective phage clones assembled to metal nanoparticle

Introduction

The controlled assembly of bio-hybrid nanostructured materials is an emerging research area due to their potential applications in bioengineering, biosensing and biomedical research.

For example, various methods of enhancement have been developed to extend detection limit of Raman spectroscopy, including enhancement with noble metal nanostructures. In fact, despite the advantages described in previous chapters, practical uses of Raman spectroscopy have been significantly limited by scattering signal, which is intrinsically weaker than most other fluorescence signals (Qian and Nie, 2008). Surface Enhanced Raman Spectroscopy (SERS) is a very sensitive analytic tool, suitable even for single molecule detection. In SERS, metal nanoparticles, such as silver or gold nanoparticles, can particularly enhance the Raman spectra of the molecules through amplifying the local electromagnetic field incident on a sample adsorbed on a metal surface (Aroca *et al*, 2005; Ko *et al*, 2008; Agarwal *et al*, 2011; Fazio *et al*, 2013). The sensitivity of SERS has been shown to be as high as 10^{14}–10^{15} (Nie and Emory, 1997; Kneipp et al., 1997). This technique is regarded as a promising analytical tool for the analysis of biological samples because it provides detailed spectroscopic information, which can be translated into imaging signal and adapted to an *in vivo* imaging system (Qian *et al*, 2008). Gold and silver nanoparticles could be used not only as plasmonically active substrates for label-free SERS detection, but also functionalized with different Raman reporter molecules for targeting specific ligands such as peptides, proteins, antibodies, deoxyribonucleic acid (DNA) and antibody fragments (Zhang *et al*, 2011; Jokerst *et al*, 2011; Gao *et al*, 2013, Neng *et al*, 2013, Baniukevic *et al*, 2013).

Moreover, the use of noble metals allows the development of new strategies in localized therapy.

It has been established that silver, mostly in the form of nitrate or sulfadiazine salts, is an antimicrobial agent and a common compound for wound treatment (Stickler, 2000). Compared to antibiotics, toxicity of silver is not specific, does not induce resistance mechanisms and shows anti-inflammatory properties (Wright *et al*, 2002).

On the other hand, other noble metals, as gold nano-particles, may be applied in responsive systems, such as pH-sensitive polymers or those activated by enzymes specific of the disease site, as well as a diverse group of externally activated vectors. Among the various interesting examples, there are gold nanoshells activated by near-infrared (NIR) light.

Gold nanoparticles absorb light in the NIR region, causing heating of tumor tissue and irreversible tissue damage (Hirsche *et al*, 2003). Furthermore, plasmon resonance can be modulated by varying the exposure light in relation to the surface to be treated.

Nevertheless, some drawback still remain such as the availability to identify selectively and with high reproducibility probes that can act like nanotags for the recognition of target cells. Molecular targeting and detection of single living cells was already achieved by using gold or silver nanoparticles conjugated with synthetic peptides (Xie *et al*, 2009, *Ahmad et al*, 2012). However, peptides have disadvantages such as the folding instability, sensibility to the changes in physico-chemical parameters of the medium and high cost of synthesis and production.

Taking into account the previously described properties, phage-metallic nanoparticles networks are considered appropriate systems to integrate the unique properties of the metallic nanoparticles while preserving the biological properties of phages as robust and selective probes.

This section describes a procedural approach for self-assembly of silver nanoparticles and phages. Particularly, the influence of different phage suspension buffers (i.e. the influence of different ions and medium pH) have been evaluated on the self-assembly of AgNPs and phages in order to find the appropriate conditions to favor the formation of the AgNPs-phage complex. The approach has been extended for the development of biologically active AgNPs–phage networks that function as signal reporters for SERS on cell-type specific molecular target. Histiocytic lymphoma cell line (U937) is used as an *in vitro* model of cancer cells, and a 9-mer pVIII M13 phage display library is screened against U937 to identify a clone that selectively recognizes these cells.

A similar approach has been developed to the functionalization of phage clones with gold nanoparticles.

Materials and Methods

Ag nanoparticles preparation. Colloidal solutions of Ag nanoparticles were prepared by pulsed laser ablation of a high purity (99.9%) silver target immersed in distilled water, using the second harmonic (532 nm) of a neodymium-doped yttrium aluminum garnet (Nd:YAG) laser (model New Wave Mod. Tempest 300) operating at 10 Hz repetition rate with a pulse width of 5 ns. The target was irradiated at the laser fluence of 1 J/cm2 and for an ablation time of 20 min.

Au nanoparticles preparation. Colloidal solutions of Au nanoparticles were prepared using the same parameters for Ag nanoparticles preparation, as described above.

Phage clones. P9b and EIII1 phage clones, deriving by affinity-selection procedures against *P. aeruginosa* and U937, were used. Isoelectric point value (pI) of phage clones was calculated by using "compute MW/pI," present on the proteomics server of the Swiss Institute of Bioinformatics Expert Protein Analysis System (ExPASy).

Phage suspension buffers.

In order to evaluate the influence of phage suspension buffer on the phage assembly with silver nanoparticles, different pH and ion-type buffers were used:

- Phosphate Buffer (PB*) 0.2 M pH 5.86. Potassium phosphate monobasic anhydrous (22.4 g/l, Lickson) and sodium phosphate dibasic heptahydrate (3.49 g/l, Sigma-Aldrich) were mixed and dissolved in ultrapure water. The final pH was 5.86.
- Phosphate Buffer (PB*) 0.2 M pH 7.23. Potassium phosphate monobasic anhydrous (9.36 g/l, Lickson) and sodium phosphate dibasic heptahydrate (32.73 g/l, Sigma-Aldrich) were mixed and dissolved in ultrapure water. The final pH was 7.23.
- Phosphate Buffered Saline (PBS) 0.01MpH 7.18. Potassium phosphate monobasic (0.2 g/l, Lickson), sodiumphosphate dibasic (1.15 g/l, Sigma-Aldrich), sodium chloride (8 g/l, Applichem) and potassium chloride (0.2 g/l, AnalytiCals Carlo Erba) were mixed and dissolved in ultrapure water. The final pH was 7.18.
- Tris-buffered saline (TBS) pH 5.18 and pH 7.02. Tris hydrochloride (7.88 g/l, Euroclone) and sodium chloride 140 mM (8.77 g/L, Applichem) were mixed and dissolved in ultrapure water. The pH was adjusted to 5.18 and 7.02 with 5 N hydrochloric acid.

Phage-AgNPs networks preparation. The phage-AgNPs networks were prepared according to the following procedure:

> Silver nanoparticles were incubated with the phage clone resuspended in different buffers (final titer $5 \cdot 10^{11}$ PFU/ml) in a 4:1 ratio at 30 °C in orbital shaking at 320 rpm (KS130 Basic IKA) over night. In order to separate the AgNPs-phage network from the unbounded phages and free silver, networks were purified by centrifugation at 20800 *xg* for 30 min and resuspended in 5 ml of their respective buffers. The complexes were stored at 4 °C until utilization.

Phage-AuNPs networks preparation. The phage-AuNPs networks were prepared according to the following:

> Gold nanoparticles were incubated with the phage clone resuspended in Phosphate Buffered Saline (PBS) 0.01M, pH 7.18 (final titer of $5 \cdot 10^{11}$ PFU/ml) in a 5:1 ratio at 30 °C in orbital shaking at 240 rpm (KS130 Basic IKA) over night. In order to separate the AuNPs-phage networks from the unbounded phages and free AuNPs, networks were purified by centrifugation at 2150 *xg* for 40 min and resuspended in 5 ml of their respective buffers. The complexes were stored at 4 °C until utilization.

Samples characterization

The UV–vis absorption response of the Ag and Au nanostructures were investigated, in the colloidal phase immediately after the ablation process, by means of a Perkin-Elmer Lambda 750 UV–vis spectrometer in the 190–1100 nm range. Further, the Ag sample morphology was investigated by means of Transmission Electron Microscopy (TEM) measurements. The TEM images were taken on appropriately dried solutions by a JEOL JEM-2010 microscope, operating at an acceleration voltage of 200KV and equipped with a Gatan 794 Multi-Scan CCD camera. A fraction of the AgNPs-phage colloidal complex was deposited on carbon substrates to carry out Scanning Electron Microscopy (SEM) characterization. SEM images were taken by a scanning electron microscope (Merlin; model ZEISS-Gemini 2) operating at an accelerating voltage of 5 kV. Micro-Raman spectroscopy measurements were carried out by means of an Horiba XploRa spectrometer equipped with an Olympus BX40 microscope, a Peltier cooled charge coupled device (CCD) sensor and a 532 nm (2.33 eV) laser as the excitation source. An acquisition time of 100s allowed a sufficient signal/noise (S/N) ratio.

Results and Discussions

Phage-displayed peptide P9b was chosen as a prototype for optimize the synthesis procedure to assembly AgNPs and bacteriophage.

In order to assess the influence of phage suspension buffer on the phage assembly with silver nanoparticles, different pH and ion-type buffers were evaluated.

Firstly, the stability of silver nanoparticles in the used buffers was evaluated by optical absorption spectroscopy in the UV–Vis region (**Figure 5.1**).

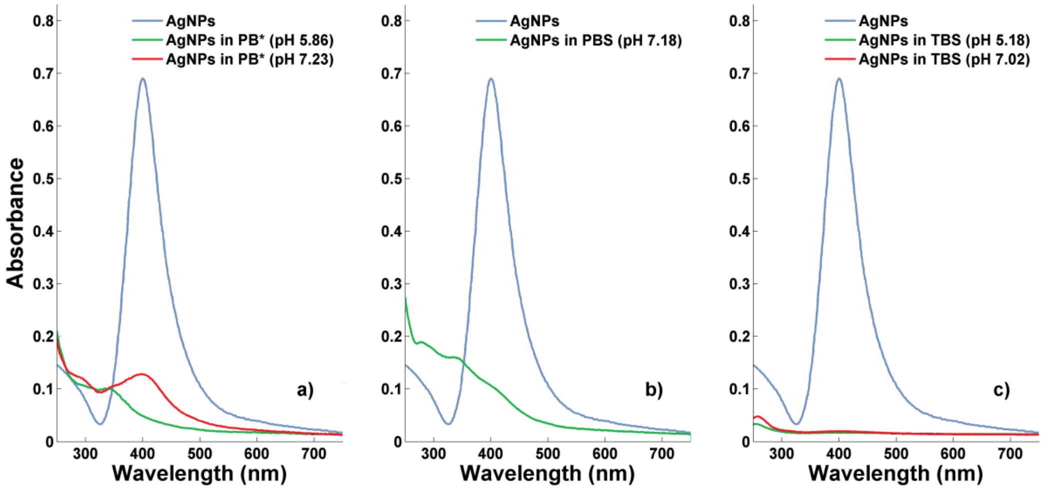

Figure 5.1. Absorption spectra of the AgNPs in different ion-type buffers and, for the same buffer, at different pH values. Data have been published in Sensing and Bio-sensing Research (Scibilia *et al*, 2016).

About Phosphate Buffer (both PB* and PBS), at pH 7.23 SPR peak intensity value of AgNPs decreases until it disappears, whereas it is totally absent at pH 5.86. About TBS, SPR feature is totally absent.

The disappearance of the Ag marker indicates that no Ag nanoparticles remain in suspension. On the overall, it emerges that the optical absorbance reduction/absence of the SPR signal is probably due to the formation of sparingly soluble silver salts on the particle surface. In fact the ions present in the buffer solutions, such as sodium (Na^+), potassium (K^+), chloride (Cl^-) and phosphate (PO_4^{3-}), complex with the AgNPs resulting in nanoparticles aggregation and precipitation. This phenomenon is usually explained as resulting from the screening of electrostatic repulsions between the nanoparticles (Wang *et al*, 2011).

Taking into account these results, silver nanoparticles were incubated with the phage clone resuspended in the different buffers. Results have been reported in **Figure 5.2**.

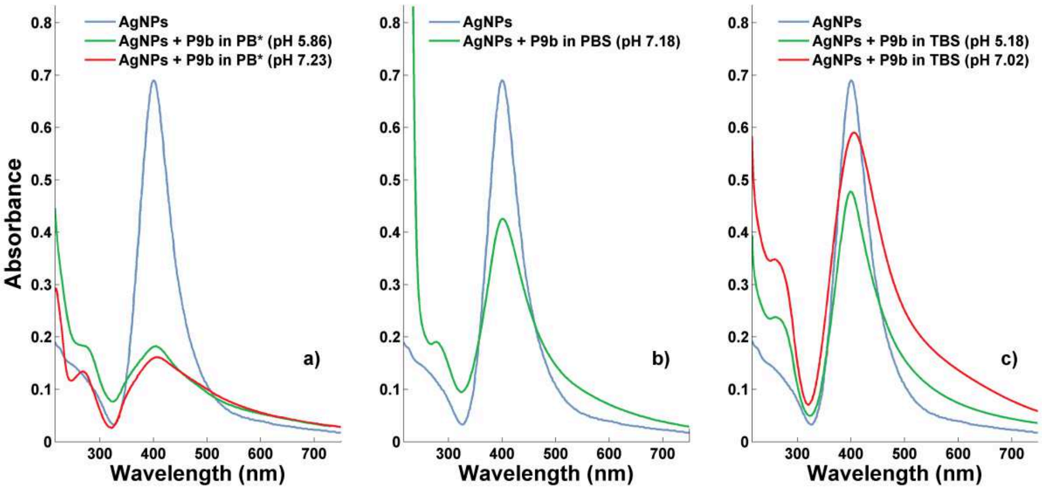

Figure 5.2 Absorption spectra of AgNPs-P9b networks in the different ion-type buffers and, for the same buffer, at different pH values. Data have been published in Sensing and Bio-sensing Research (Scibilia *et al*, 2016).

The most relevant evidences are that the AgNPs does not totally precipitate in the presence of bacteriophage as well as an agglomeration process occurs between the species in solutions. Moreover, all spectra show a low visible contribution in the 250–270 nm range, due to the aromatic residues of phage (Overman *et al*, 2005).

About PB*, spectra show the well-known SPR band centered at 405 nm, even if with significantly reduced intensity values and asymmetrically widens with respect to that observed for the water-prepared AgNPs (control). This behavior seems to be partially affected by the pH values of the PB* buffer solution.

SPR of the AgNPs-P9b networks in Phosphate Buffered Saline (PBS) and both Tris-buffered saline (TBS) show that line shapes have very similar behaviors. Comparing these features with the behavior shown in **Figure 5.1**, the most relevant evidence is the persistence of AgNPs SPR peak, similar to that prepared in water, indicating that an interaction between phage and AgNPs maintains the latter in suspension. Also in both TBS buffers, this phenomenon seems to be partially dependent on the pH values and different ionic species of buffer.

On the overall, the optical absorption response in the different ion-type buffers and pH values is influenced by the different ions present and by the fluctuations in the surrounding ion clouds (Jeon *et al*, 2011). In fact, polyelectrolytes in aqueous solution are coated by a condensed layer of mobile oppositely charged counterions (Butler *et al*, 2003). Because of their polyelectrolyte nature, M13 and other filamentous viruses can be complexed by different ions, changing the spatial distributions of charges on their surfaces. In particular, pVIII major coat proteins constitute the bulk of the total charge on the virus. Changes in the phage surface charge dramatically affect its ability to assemble procapsids, as reported by Parent *et al* (2003).

The importance of salt–bridge interactions in stabilizing proteins varies and appears to be highly dependent upon factors such as the screening of the charges by solvent, the cost of desolvating the charged groups to form these bridges, and the relative flexibility of the side chains involved in the ion pair (Yang *et al,* 1992).

Furthermore, the pVIII protein surface charge density can be controlled by changing the pH of the system in the range around the pI of pVIII-P9b phage protein. pI value of pVIII is 6.3, therefore protein surface charge is positive at pH below pI. Because in both cases a similar behavior has been noticed, results suggest that the assembly of silver nanoparticles onto phage is not only directed by opposite-charge interaction between silver nanoparticles and bacteriophage, but rather by different ions types present in the buffer. The electrostatic interactions between silver nanoparticles and bacteriophage are governed by the Brownian motion of the ions in the buffer solution, that act like attractor sites, by creating salt bridge and promoting the formation of AgNPs-phage networks.

The occurred formation of the networks, consisting of entire bacteriophage structure directly assembled with AgNPs, was evidenced carrying out SEM/EDX measurements. Particularly closed-packed Ag-phage nanostructures were formed on the assembled phage films on all the micrometer-length scale investigated, as shown in **Figure 5.3**. Most of the AgNPs are in the regions in which the EDX probe shows the presence of nitrogen, carbon and oxygen species as well as atomic species typical of salts. This result indicates that the phage structures are decorated to the AgNPs and in proximity of the salts.

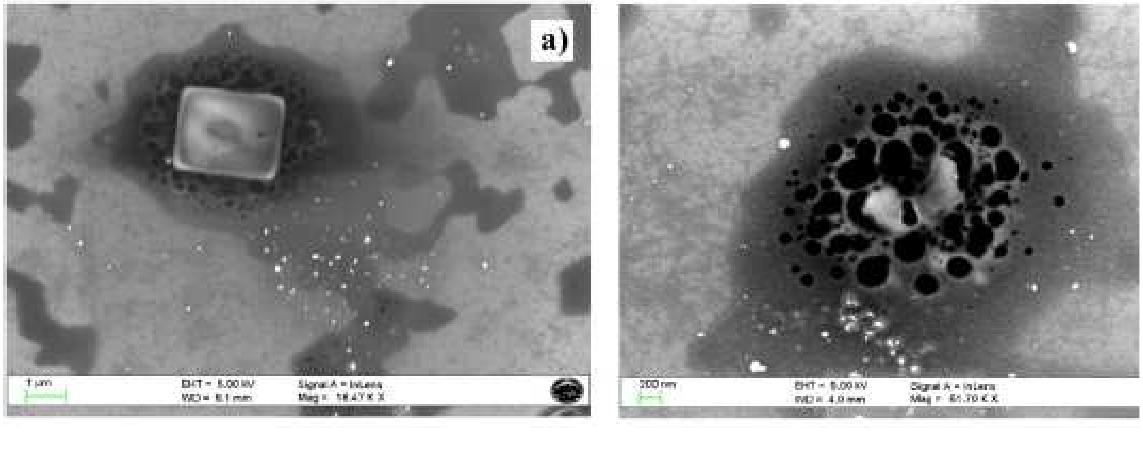

EI	AN	Series	unn. (wt.%)	Cnorm (wt.%)	Cnorm (at.%)	C Error (1Sigma) (wt.%)
Si	14	K-series	104.52	73.57	76.37	4.92
Ag	47	L-series	25.61	18.03	4.87	1.77
C	6	K-series	7.82	5.50	13.35	1.30
O	8	K-series	2.07	1.45	2.65	0.47
N	7	K-series	1.77	1.24	2.59	0.46
Cl	17	K-series	0.28	0.20	0.16	0.06
		Total	142.6	100	100	

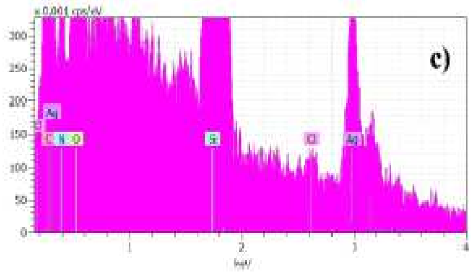

Figure 5.3 SEM image of AgNPs-P9b networks in TBS. Data have been published in Sensing and Bio-sensing Research (Scibilia *et al*, 2016).

Raman spectroscopy characterization provides additional evidence for the comprehension of the phage-silver interaction.

Particularly, in **Figure 5.4** the Raman spectra of P9b phage and AgNPs-P9b networks in PBS (pH 7.18) are shown. The Raman spectrum of phage is characterized by some contributions located at 993, 1285 and 1643 cm^{-1}, attributed to the stretching mode of amide and the peaks centered at 540 and 1455 cm^{-1}, ascribed to polar and aromatic residues of phage coat proteins (Aslanian *et al*, 1982).

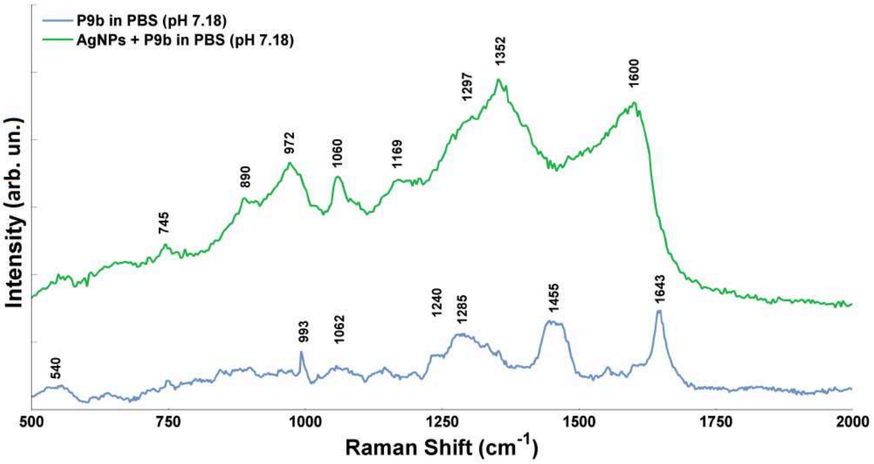

Figure 5.4 Raman spectra of AgNPs-P9b networks in PBS (pH 7.18). Data have been published in Sensing and Bio-sensing Research (Scibilia *et al*, 2016).

The contribute at 540 cm^{-1} is related to ν(S–S) trans-gauche mode of amino acid cysteine. The wild-type sequences of M13 major coat proteins do not contain cysteines, whereas pIII, pVII, and pIX have internal cysteines that play important roles in structure formation via disulfide bonds (Chung *et al*, 2014). Moreover, the phage Raman spectrum is characterized by a barely visible band at 1240 cm^{-1}, due to amide III random coil, and by a narrow peak at 1643 cm^{-1}, attributed to the major capsid protein (pVIII) α-helix secondary structure (Siddhanta *et al,* 2012). The AgNPs–P9b network shows some differences respect to the P9b phage. A significant shift of the Raman features associated to the protein contributions and the appearance of new Raman features, centered at around 745, 890, 972, 1169, 1297, 1352 and 1600 cm^{-1}, have been observed.

Moreover, with respect to the P9b phage Raman spectrum, the contributions at about 1060 cm^{-1} are very intense, referred to the PO^{2-} stretching mode of packaged ssDNA phage (Benevides *et al*, 1991) and the peaks at 745, 890 and 972 and at 1352 cm^{-1}, ascribed to the symmetric breathing of tryptophan, C-C and C-N stretching mode of amide.

These spectral changes depend on the orientation and the distance of the molecules from the surface of the metal nanostructures (Podstawka *et al,* 2004).

M13 filamentous bacteriophage coat is a symmetric array of several thousand α-helical major coat proteins (pVIII) that surround the DNA core.

The sequence of pVIII can be divided into four functional domains [22]: (i) an acid (1–6) and (ii) an amphipathic domain (7–20) on the N-terminus; (iii) a hydrophobic (21–39) and (iv) a basic domain (40–50) located near the C-terminus, as observed in **Figure 5.5**.

H_2N-**^{1}Ala-Glu-Gly-Asp-Asp-^{6}Pro-^{7}Ala-Lys-Ala-Ala-Phe-Asn-Ser-Leu-Gln-Ala-Ser-Ala-Thr-^{20}Glu-^{21}Tyr-Ile-Gly-Tyr-Ala-Trp-Ala-Met-Val-Val-Val-Ile-Val-Gly-^{39}Ala-^{40}Thr-Ile-Gly-Ile-Lys-Leu-Phe-Lys-Lys-Phe-Thr-Ser-Lys-Ala-^{50}Ser-**COOH

Figure 5.5 Schematic showing the primary structure and domain organization of the pVIII major coat protein in phage M13. Red: acid domain (1–6); Green: amphipathic domain (7–20); Blue: hydrophobic domain (21–39); Orange: basic domain (40–50). Data have been published in Sensing and Bio-sensing Research (Scibilia *et al*, 2016).

It's known from literature, Tyr 21 and Tyr 24 are located in a loop region while Phe 26 is positioned in an α-helix tract, so about six residues are accessible to solution and contribute to the surface charge on M13 (Matsuno *et al,* 1998). By changing the pH or the ions in buffer solution, the protonation states of the amino acids on the virus major coat protein were modified, as well as surface charge density (Butler *et al,* 2003).

In this context, the Raman spectral changes, observed in presence of the AgNPs, mainly indicate stretching modes deformation of tyrosine and phenylalanine residues, suggesting the phage direct interaction with AgNPs (Stewart *et al.*, 1999) and preserving the binding activity of the engineered peptides displayed on the N-terminus of the same major coat proteins.

In TBS, the Raman spectrum of phage is similar to one observed in PBS, although some features related to the CH_2OH groups stretching vibration of polar amino acids serine and threonine at 1045 cm^{-1} (Rehman *et al*, 2012) and to the vibrational modes of the nucleotide bases of packaged ssDNA located at 598 and 1290 cm^{-1} (Benevides *et al,* 1991) are more evident (**Figure 5.6**).

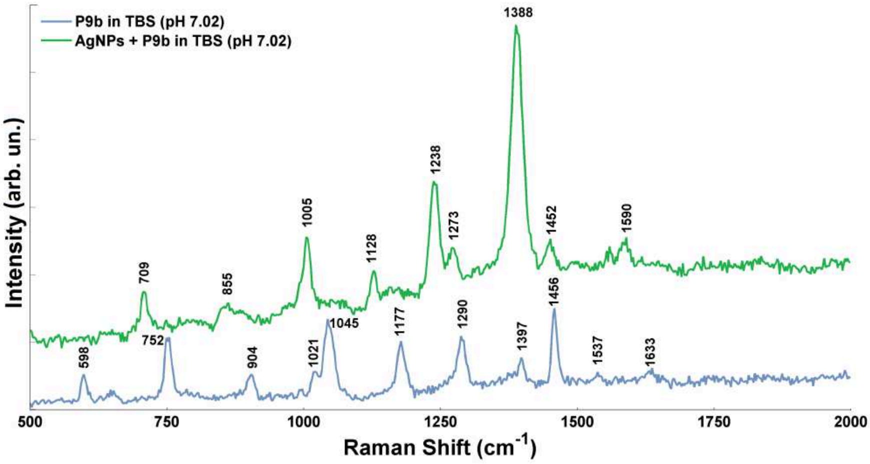

Figure 5.6 Raman spectra of AgNPs-P9b networks in TBS (pH 7.02). Data have been published in Sensing and Bio-sensing Research (Scibilia *et al*, 2016).

These findings point out a folding variation of phage coat proteins in TBS buffer, as well as confirmed by the presence of a peak located at 904 cm^{-1}, assigned to the variations in the secondary structures of proteins (CH_2/CH_3 deformations as scissoring, wagging, twisting, and rocking).

The main differences between the Raman spectra of AgNPs-P9b complex and P9b in TBS are: (i) the shift of the phenylalanine contribution from 1456 cm^{-1} down to 1452 cm^{-1}; (ii) the appearance of new Raman peaks at 1005 and 1590 cm^{-1}, ascribed to asymmetric and symmetric ring breathing modes of phenylalanine (Stewart *et al,* 1999); (iii) the appearance of new contributes at 709 and 855 cm^{-1}, assignable to tyrosine residues (Siamwiza *et al*, 1975); (iv) the appearance of some peaks related to protein stretching modes (at 1128, 1238, 1273 and 1388 cm^{-1}). These dynamic structural changes indicate the binding of silver nanoparticles mainly on the aromatic side chains of tyrosine and phenylalanine residues. In particular, three important residues (Tyr 21, Tyr 24 and Phe 26), located in a highly hydrophobic segment of the pVIII protein, are involved in the assembly of bacteriophage and AgNPs. Furthermore, the appearance of a new peak at 1273 cm^{-1}, which is assignable to CH α-helix rocking, confirm the folding variation of the α-helix portion of the hydrophobic domain where the phenylalanine residue 26 is located (Tsuboi *et al,* 2001).

Also in this case, the engineered peptides on N-terminal portions of the PVIII remain available for a specific and selective target-binding.

The intrinsic ability to produce stable species without the *a priori* need for any aggressive chemicals, like reducing or capping agents, makes laser ablation in liquids particularly attractive as a biocompatible technique, allowing to obtain AgNPs useful for biomedical applications.

Moreover, as previously described, AgNPs–phage networks may function as signal reporters for SERS on cell-type specific molecular targets, such as neoplastic cells.

In order to verify this possibility, histiocytic lymphoma cell line (U937) has been used as an *in vitro* model of cancer cells, and EIII1 is used to selectively identify these cells.

Figure 5.7 shows Raman spectra of U937 and EIII1 alone.

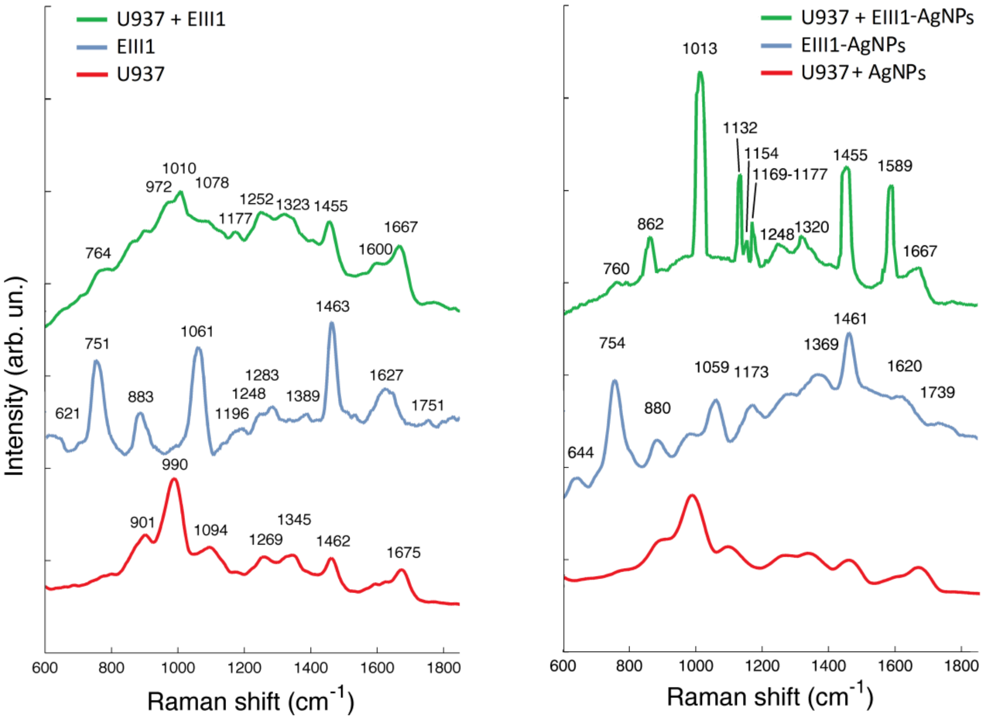

Figure 5.7 Raman spectra of U937cells, EIII1 phage and U937–EIII1 complex (left panel) and AgNPs + U937cells, AgNPs–EIII1 and AgNPs–EIII1 + U937 (right panel). Data have been published in Biosensors and Bioelectronics (Lentini *et al*, 2015)

Raman spectra recorded on different samples as well as on different positions within the samples, were similar. The Raman spectrum of U937 cells shows many peaks assignable to proteins (901.5, 990.4, 1269 and 1675 cm^{-1}), nucleic acids (1094 and 1345 cm^{-1}) and saccharides (1462 cm^{-1}) (Allegra *et al*, 2014).

In this experimental condition, the presence and the position of new Raman features, compared to those described in chapter two, are strongly influenced by cell fixation methods (Chan *et al*, 2009; Ranc *et al*, 2013). Treatment with methanol induces an increase in intensity of the contributions assignable to membrane proteins and carbohydrates. This behaviour is explained on the basis of the action of methanol on membrane lipids. On the other hand, the peaks ascribed to the protein composition remained almost unchanged. Moreover, the U937 methanol treatment did not modify the ability of the phage clone to recognize its cellular target.

About EIII1 (**Figure 5.7**), Raman spectra are characterized by some contributions located at 1196, 1248, 1283, 1388, 1627 and 1751 cm^{-1} , attributed to the stretching mode of amide, and other peaks centred at 621, 751.7 and 1463 cm^{-1}, due to the aromatic residues of phage coat proteins (Aslanian *et al*, 1982; Aubrey and Thomas, 1991). Moreover, the Raman spectrum of EIII1 showed a weak band at 883.5 cm^{-1} and an intense contribution at 1062 cm^{-1}, referred to the PO^{2-} stretching mode of packaged ssDNA phage (Benevides *et al*, 1991).

Finally, about U937-EIII1 assemblies, **Figure 5.7** shows a shift to lower wavenumber of feature ascribable to proteins, nucleic acids and saccharides contributions (1078, 1252, 1323, 1455 and 1667 cm^{-1}) and appearance of new Raman peaks, centred at 764, 972, 1010, 1177 and 1600 cm^{-1}. The shift in Raman peaks is related to the interaction of engineered phage peptides with the U937 cells (Fabriciova *et al*, 2004; Jurasekova *et al*, 2009), while the new peaks are ascribed to stretching modes of saccharides and proteins, suggesting that phage-binding target is represented by a cellular glycoprotein (Lu *et al*, 2013).

Although the specific recognition allows discriminating the superimposition of many different chemical entities, arising from the co-presence of phage and cell, it is not possible to use this features as a marker for discrimination of cell target recognized by the phage. On the other hand, since SERS preferentially enhances the spectral regions of molecular groups in which noble metal take place, AgNPs-EIII1 network has been used to evaluate U937-phage interaction.

In **Figure 5.7** the Raman spectra of AgNPs-U937 and AgNPs-EIII1 assemblies are shown.

The Ag-U937 spectrum was similar to the U937 one, while the AgNPs-EIII1 network showed some differences respect to the EIII1 phage. The differences are mainly associated to enhancement and slightly shifting of protein and DNA contributions. These spectral changes depend on the orientation and the distance between molecules and Ag-NPs, according to Podstawka *et al* (2004). If the Raman vibrations of the reporter molecules are narrow and do not overlap, the inclusion of AgNPs-EIII1 network into U937 cells can potentially monitor simultaneously different and new interactions.

U937cells targeted by EIII1-AgNPs network showed the appearance of new Raman scattering peaks at 862.6, 1132 and 1154 cm^{-1} in addition to the enhancement intensity of some of the fundamental U937 Raman features (specifically, the contributions related to proteins centred at 760.6, 1013, 1154, 1169, 1177,1248, 1320, 1455, 1589 and 1667 cm^{-1}). These spectral features refer to the oligosaccharides complexes, namely molecules involved in probe-target interaction (Rehman *et al*, 2012). The strong electric field near the AgNPs allowed a different coupling mechanism between the optical electric field and the vibration. The selection rule for this process differed markedly from the usual Raman selection rules. The SERS-induced occurrence of new Raman peaks was attributed to the lowering of the symmetry of the investigated molecules or to the presence of a steep field close to the nanoparticles metal surface (Fazio *et al,* 2012). In this case, EIII1-AgNPs complexes "bind" a cell-specific target probably represented by a glycoprotein receptor localized on the plasma membrane.

As previously described, the proposed network has the advantage to integrate the unique signal reporting properties of AgNPs while preserving the biological properties of phage without the use of additional SERS signal reporters. In this system no preliminary information about the nature of target are needed and its application is potentially extensible for the detection of any cell-type specific molecular targets.

Moreover, AgNPs–phage network could be used as carrier for therapeutic drugs and for cancer cells targeting and killing. In fact, it is well known that AgNPs are selectively involved in the disruption of mitochondrial respiratory chain, leading to ROS production and to the interruption of ATP synthesis which cause DNA damage (Rosarin *et al,* 2012).

The approach just described has also been developed for the functionalization of phage clones with gold nanoparticles. Also in this case, phage-displayed peptide P9b was chosen as a prototype **(Figure 5.8).**

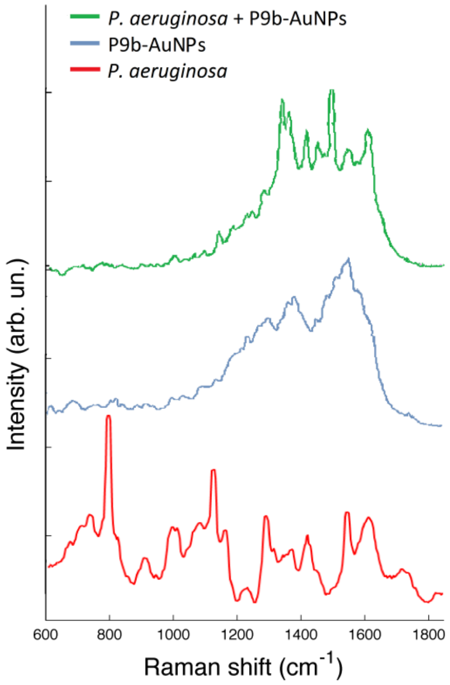

Figure 5.8 Raman spectra of *P. aeruginosa*, P9b-AuNPs and *P. aeruginosa* + P9b-AuNPs.

Raman spectra profile of phage P9b funzionalized with Au-NPs is very similar to what was observed for P9b funzionalized with Ag-NPs in PBS buffer (**Figure 5.4**).

However in this case, the enhanced spectral features turn out to be solely attributable to protein contributions. To test whether the clone maintained its ability to recognize its cell target, P9b-AuNPs have been mixed with *P. aeruginosa*. The increase of intensity of Raman contribute around 1300-700 cm^{-1} region indicates that the gold nanoparticles are positioned near the surface proteins. Moreover, absence of significant peaks under 1000 cm^{-1} reveals that no interactions could be recorded between nucleic acids, namely DNA or RNA, and P9b-AuNPs.

These results are according with Carnazza *et al*, for which P9b phage clone specifically recognizes and binds the outer membrane fraction of *P. aeruginosa* (Carnazza *et al,* 2008).

Acknowledgements

This activity was partially funded by Italian Ministry of Education, University and Research (MIUR) by means of the national Program PON R&C 2007–2013, project project HIPPOCRATES – Development of Micro and Nano-Technologies and Advanced Systems for Human Health (PON02_00355_29641931).

XploRA Raman spectrometer was a kind gift of A.B.A.L. onlus Messina (Italy) (http://www.abalmessina.it).

This activity was carried out in collaboration with:

Doctor E. Fazio and Professor F. Neri Department of Mathematical and Computational Sciences, Physical Science and Earth Science (MIFT), University of Messina, Italy.

Doctor S. Trusso Institute of Chemical-Physical Processes (IPCF)-CNR Messina, Italy.

Doctor S. Scibilia and Professor A. M. Mezzasalma Department of Mathematical and Computational Sciences, Physical Science and Earth Science (MIFT), University of Messina, Italy.

Doctor A. Allegra and Professor C. Musolino, Division of Hematology, Department of General Surgery, Pathological Anatomy and Oncology, University of Messina, Italy

Bibliography

Agarwal N, Fazio E, Neri F, Trusso S, Castiglioni C, Lucotti A, Santo N, Ossi PM. Ag and Au nanoparticles for SERS substrates produced by pulsed laser ablation. 2011. Cryst. Res. Technol. 46, 836–40.

Allegra A, Fazio E, Franco D, Nicolò M, Trusso S, Neri F, Musolino C, Guglielmino SPP. Low-energy laser irradiation promotes cellular damage in Glucocorticoids-resistant Multiple Myeloma cells. 2014. Leuk. Lymphoma 3,1–3.

Aroca RF, Alvarez-Puebla RA, Pieczonka N, Sanchez-Cortes S, Garcia-RamosJV. Surface-enhanced Raman scattering on colloidal nanostructures. 2005. Adv. Colloid Interface Sci.116, 45–61.

Aslanian D, Rontó G, Tóth K. Raman study of isolated and "in situ" T7 phage DNA: conformation and possible interaction with the proteins. 1982. Acta Phys. Acad. Sci. Hung. 53, 25–32.

Athamneh AIM, Senger RS. Peptide-Guided Surface-Enhanced Raman Scattering Probes for Localized Cell Composition Analysis.2012. Appl. Environ. Microbiol. 78, 7805–08.

Aubrey KL, Thomas Jr. GJ. Raman spectroscopy of filamentous bacteriophage Ff (fd, M13, f1) incorporating specifically-deuterated alanine and tryptophan side chains. Assignments and structural interpretation. 1991. Biophys. J. 60, 1337–49.

Baniukevic J, Boyaci IH, Bozkurt AG, Tamer U, Ramanavicius A, Ramanaviciene A. Magnetic gold nanoparticles in SERS-based sandwich immunoassay for antigen detection by well oriented antibodies. 2013.Biosens. Bioelectron. 43, 281–88.

Benevides JM, Stow PL, Ilag LL, Incardona NL, Thomas Jr GJ. Differences in secondary structure between packaged and unpackaged single-stranded DNA of bacteriophage phi X174 determined by Raman spectroscopy: a model for phi X174 DNA packaging. 1991 Biochemistry 30, 4855–63.

Butler JC, Angelini T, Tang JX, Wong GCL. Ion multivalence and like-charge polyelectrolyte attraction. 2003. Phys. Rev. Lett. 91, 028301.

Carnazza S, Foti C, Gioffrè G, Felici F, Guglielmino SPP. Specific and selective probes for Pseudomonas aeruginosa from phage-displayed random peptide libraries. 2008. Biosens. Bioelectron. 23, 1137–44.

Chan JW, Taylor DS, Thompson DL. The effect of cell fixation on the discrimination of normal and leukemia cells with laser tweezers Raman spectroscopy. 2009. Biopolymers 91,132–39.

Chung WJ, Lee DY, Yoo SY, Chemical modulation of M13 bacteriophage and its functional opportunities for nanomedicine. 2014. Int. J. Nanomedicine 9, 5825–36.

Kneipp K, Wang Y, Kneipp H Perelman LT, Itzkan I, Dasari RR, Feld MS. Single Molecule Detection Using Surface-Enhanced Raman Scattering (SERS). 1997. Phys. Rev. Lett. 78, 1667–70.

Ko H, Singamaneni S, Tsukruk VV. Nanostructured Surfaces and Assemblies as SERS Media 2008. Small 4,1576–99.

Fabriciova G, Sanchez-cortes S, Garcia-Ramos JV, MiskovskyP. Surface-enhanced Raman spectroscopy study of the interaction of the antitumoral drug emodin with human serum albumin. 2004. Biopolymers 74,125–30.

Fazio E, Neri F, Valenti A, Ossi PM, Trusso S, Ponterio RC. Raman spectroscopy of organic dyes adsorbed on pulsed laser deposited silver thin films. 2013. Appl. Surf. Sci. 278, 259–64.

Fazio E, Neri F, Savasta S, Spadaro S, Trusso S. Surface-enhanced Raman scattering of SnO2 bulk material and colloidal solutions. 2012. Phys. Rev. B 85 (195423).

Gao F, Lei J, Ju H. Label-Free Surface-Enhanced Raman Spectroscopy for Sensitive DNA Detection by DNA-Mediated Silver Nanoparticle Growth. 2013.Anal. Chem. 85, 11788–93.

Hirsch LR, Stafford RJ, Bankson JA, Sershen SR, Rivera B, Price RE, Hazle JD, Halas NJ, West JL. Nanoshell-mediated near-infrared thermal therapy of tumors under magnetic resonance guidance. 2003. Proc. Natl. Acad. Sci. 100, 13549-54.

Jeon DY, Hwang KH, Park SJ, Kim YJ, Joo MK, Ahn SE, Kim GT, Nam CH. Controlled surface adsorption of fd filamentous phage by tuning of the pH and the functionalization of the surface. 2011. J. Appl. Phys. 109, 064701

Jokerst JV, Miao Z, Zavaleta C , Cheng Z, Gambhir SS. Affibody-Functionalized Gold–Silica Nanoparticles for Raman Molecular Imaging of the Epidermal Growth Factor Receptor. 2011. Small 7, 625–33.

Jurasekova Z, Marconi G, Sanchez-cortes S,Torreggiani A. Spectroscopic and molecular modeling studies on the binding of the flavonoid luteolin and human serum albumin. 2009.Biopolymers 91, 917–927.

Lentini G, Fazio E, Calabrese F, De Plano LM, Puliafico M, Franco D, Nicolò MS, Carnazza S, Trusso S, Allegra A, Neri F, Musolino C, Guglielmino SPP. 2015. Phage-AgNPs complex as SERS probe for U937 cell identification. Biosens. Bioelectron. 74, 398–405.

Lu X, Liu Q, Benavides-Montano JA, Nicola AV, Aston DE, Rasco BA, Aguilar C. Detection of Receptor-Induced Glycoprotein Conformational Changes on Enveloped Virions by Using Confocal Micro-Raman Spectroscopy. 2013. J. Virol. 87, 3130–42.

Matsuno M, Takeuchi H, Overman SA, Thomas Jr GJ. Orientations of tyrosines 21 and 24 in coat subunits of Ff filamentous virus: determination by Raman linear intensity difference spectroscopy and implications for subunit packing. 1998. Biophys. J. 74, 3217–25.

Neng J, Harpster MH, Wilson WC, Johnson PA. Surface-enhanced Raman scattering (SERS) detection of multiple viral antigens using magnetic capture of SERS-active nanoparticles. 2013. Biosens. Bioelectron. 41, 316–21.

Overman SA, Bondr P, Maiti NC, Thomas GJJr., "Structural characterization of the filamentous bacteriophage PH75 from Thermus thermophilus by Raman and UVresonance Raman spectroscopy, 2005Biochemistry 44, 3091–100.

Parent KN, Doyle SM, Anderson E, Teschke CM. Electrostatic interactions govern both nucleation and elongation during phage P22 procapsid assembly. 2005. Virology 340, 33–45.

Podstawka E, Ozaki Y, Proniewicz LM. Part II: surface-enhanced Raman spectroscopy investigation of methionine containing hetero dipeptides adsorbed on colloidal silver. 2004. Appl. Spectrosc. 58, 570–80.

Qian X, Peng XH, Ansari DO, Yin-Goen Q, Chen GZ, Shin DM, Yang L, Young AN, Wang M. D, Nie S. In vivo tumor targeting and spectroscopic detection with surface-enhanced Raman nanoparticle tags. 2008. Nat. Biotechnol. 26, 83–90.

Santi Scibilia S, Lentini G, Fazio E, Franco D, Neri F, Mezzasalma AM , Guglielmino SPP. Self-assembly of silver nanoparticles and bacteriophage. 2016. Sensing and Bio-Sensing Research 7, 146–152.

Ranc V, Srovnal J, Kvítek L, Hajduch M. Discrimination of circulating tumor cells of breast cancer and colorectal cancer from normal human mononuclear cells using Raman spectroscopy. 2013.Analyst 138(20),5983–5988.

Rehman IU, Movasaghi Z, Rehman S. 2012. Series in Medical Physics and Biomedical Engineering, CRC Press; A Taylor and Francis Book.

Siamwiza MN, Lord RC, Chen MC, Takamatsu T, Harada I, Matsuura H, Shimanoichi T. Interpretation of the doublet at 850 and 830 cm-1 in the Raman spectra of tyrosyl residues in proteins and certain model compounds. 1975. Biochemistry 14, 4870–76.

Siddhanta S, Narayana C. Surface enhanced Raman spectroscopy of proteins: implications for drug designing, Nanomater. 2012. Nanotechnol. 2, 1–13.

Stewart S, Fredericks PM. Surface-enhanced Raman spectroscopy of amino acids adsorbed on an electrochemically prepared silver surface. 1999. Spectrochim. Acta A 55, 1641–60.

Stickler DJ. Biomaterials to prevent nosocomial infections: is silver the gold standard? 2000. Curr. Opin. Infect. Dis., 13, 389-93.

Tsuboi M, Ushizawa K, Nakamura K, Benevides JM, Overman SA, Thomas Jr. GJ. Orientations of Tyr 21 and Tyr 24 in the capsid of filamentous virus Ff determined by polarized Raman spectroscopy. 2001 Biochemistry 40, 1238–1247.

Wang D, Tejerina B, Lagzi I, Kowalczyk B, Grzybowski BA. Bridging interactions and selective nanoparticle aggregation mediated by monovalent cations. 2011. ACS Nano 5,530–36.

Wright JB, Lam K, Buret AG, Olson ME, Burrell RE. Early healing events in a porcine model of contaminated wounds: effects of nanocrystalline silver on matrix metalloproteinases, cell apoptosis, and healing. 2002 Wound Repair Regen. 10, 141-51.

Xie W, Wang L, Zhang Y, Su L, Shen A, Tan J, Hu J. Nuclear Targeted Nanoprobe for Single Living Cell Detection by Surface-Enhanced Raman Scattering. 2009. Bioconjugate Chem. 20, 768–73.

Yang AS, Sharp KA, Honig B. Analysis of the heat capacity dependence of protein folding. 1992 J. Mol. Biol. 227, 889–900.

Zhang Y, Hong H, Myklejord DV, CaiW. Molecular Imaging with SERS-Active Nanoparticles. 2011. Small 7,3261–69.

CHAPTER 6
Selective phage clones assembled to nanocarriers

Introduction

One advantage of nanocarriers is their ability to overcome various biological barriers and to localize into the target tissue. Many drug-delivery systems have been developed in order to increase the therapeutic benefit and minimize side effects.

The nanocarriers currently used and investigated can be classified into three main temporally consecutive groups (Sakamoto *et al*, 2007)

The first group comprises passive delivery systems that localize into the target site, as a result of higher permeation and retention (Partk *et al,* 2002). These systems, generally used for cancer therapy, include liposomal nanocarriers covered with a layer, for example of polyethylene glycol, that prevents their uptake by phagocytic blood cells and prolongs their circulation time (Romberg *et al*, 2008; Harris, 2003). Another system of this group includes metal nanoparticles and albumin–paclitaxel nanoparticles, for which drug localization is driven only by the size of the particles and is not related to specific recognition.

The second group of nanocarriers has specific additional functionalities which allow both molecular recognition of the target tissue and active or triggered release of the drug at the disease site. Moreover, this system includes responsive systems, for example, pH-sensitive polymers, activation mediated by specific enzymes or other systems, such as gold nanoshells activated by near-infrared (NIR) light (Duncan, 2003)

The most representative nanocarriers subclass in this group are antibody-functionalized liposomes and nanoparticles (Goren *et al*, 1996; Brannon-Peppas *et al*, 2004).

Antibodies are commonly used as probes for detection of viruses and different bacterial species, so their recognition ability of specific cellular targets, as a tumor marker, can be used to drive the nanocarriers, loaded with the drug, to the disease site, allowing a targeted drug release. However, antibodies efficiency and stability depend on several factors, as temperature, pH, osmolarity, which influence their shelf-life; moreover, their production is still quite expensive and consequently their application will increase the costs of the final product.

Both the representatives of the groups above described are not exempt from barriers which encounter when introduced into the body and significantly reduce the probability of reaching the target tissues at a concentration required for obtaining therapeutic efficacy.

In theory, the ideal nanocarrier should be able to circulate in the vascular system following intravenous administration, recognize drug target, and accordingly release it at high concentrations. This goal can be achieved by multistage approach, which consists in assembling two nanocarriers, defined as first and second stage. Nanocarriers of the second stage are loaded in a larger nanocarrier (defined first stage), which is made of biodegradable and biocompatible materials and with pores size of up to 50 nm. The basic mechanism of the system involves the first stage microparticles targeting the disease molecular markers on the vasculature walls, releasing the second stage nanoparticles loaded with therapeutic agent(s) and facilitating the delivery of active agent into the affected cells so as to provide an enhanced therapeutic effect.

Some of the traditionally used polymers for first stage nanocarrier production, like silicone, have been suspected to cause cancer (Cammas *et al*, 1999).

As consequence, candidate materials to be effectively used, as biopolymers, should be non toxic and biocompatible, in order to minimize any side effects.

Among biopolymers, poly(3-hydroxy)alkanoates (PHAs), polyesters produced by various bacteria as energy/carbon storage materials, usually under unbalanced growth conditions, are particularly attractive.

Poly(3-hydroxy)alkanoates

Poly(3-hydroxy)alkanoates (PHAs) are synthesized by Gram-positive and Gram-negative bacteria, and more than 300 different microorganisms are known to synthesize and accumulate PHAs intracellularly including *Azotobacter* sp., *Pseudomonas* sp., *Bacillus* sp., and *Methylobacterium* sp. (Steinbuchel and Fuchtenbusch, 1998).

They are synthesized as granular cytoplasmic inclusions under nutrient-limiting conditions and excess of carbon source (Steinbuchel and Schlegel, 1991; Keshavarz and Roy, 2010). Moreover, their chemical composition depends on the producer microrganism, the starting substrate and the process conditions and corresponds to a wide diversity of applications (Nicolò *et al*, 2015).

Despite the wide range of applications, commercial diffusion is actually limited by several technical constraints. One of the most pursued strategies to overcome such limits is the identification of growth parameters that may increase the number of producing cells as well as reduce the time required for PHA production.

From this point of view, it has been shown that glutamine, added as nutritional supplement in the culture medium, strongly increases both biomass and PHA yields, favoring the uptake and catabolism of a given carbon source (Rizzo *et al.*, 2016).

One of the unique properties of PHA is their easy biodegradability into water and carbon dioxide by several microorganisms found in a wide range of environments. (Byrom *et al*, 1987). These properties could be exploited in biomedical applications, in that they may be coupled with release of bioactive compounds, such as antibiotics or antitumor drugs. In this sense, the design of polymer chemical properties, deriving by different monomer side chains, can allow the optimization of dosing and the kinetics of the drug release.

This section describes a preliminary test of physical adsorption on PHA microspheres surface of P9b phage clone, expressing peptides able to strongly bind *Pseudomonas aeruginosa* cells, as a proof of concept of specific drug targeting.

For a successful PHA microsphere conjugation with both drug and phage protein, PHA monomer composition is a critical factor that should be considered in the development of an innovative guided-drug delivery system.

In this section, PHA production by several *Pseudomonas* species was optimized in terms of yield and composition of polymer. Particularly, the human pathogen *Pseudomonas aeruginosa* ATCC 27853 and the phytopathogen *Pseudomonas mediterranea* DAPPG51 have been used.

By varying the carbon source (octanoic, lauric, myristic and stearic acids) and the eventual imposition of a metabolic stress (starvation of nutrients, as nitrogen and magnesium; limiting concentrations of nitrogen), PHAs with different pending chain length and, consequently with different physico-chemical properties were obtained. These properties could influence drug-carrier interactions in the drug-delivery system. The following physical-chemical parameters have been considered: molecular weight, monomer composition, melting temperature and glass transition temperature.

Moreover another phytopathogen, namely *Pseudomonas mediterranea* 9.1, was tested for its ability to degrade the main components of crude glycerol, e.g. pure glycerol and myristic, erucic, stearic, linoleic and palmitic acids, and convert them into PHA. The obtained polimer has been chosen as a model biomaterial for creating a second generation guided nanocarrier.

Material and Methods

Bacterial strains, media and growth conditions. All bacterial strains were maintained in Luria Bertani (LB) broth at 30-37 °C under shaking (250 rpm). For PHA production, exponential-phase cells, precultured in LB broth, were inoculated in a chemically defined mineral medium.

The medium contained the following (per liter): 5.8 g K_2HPO_4, 3.7 g KH_2PO_4, 10 ml 0.1 M $MgSO_4$, supplemented with 1 ml of a microelement solution (MT solution). MT solution contained the following (per liter): 2.78 g $FeSO_4 \cdot 7H_2O$, 1.98 g $MnCl_2 \cdot 4H_2O$, 2.81 g $CoSO_4 \cdot 7H_2O$, 1.67 g $CaCl_2 \cdot 2H_2O$, 0.17 g $CuCl_2 \cdot 2H_2O$, 0.29 g $ZnSO_4 \cdot 7H_2O$. After the addition of carbon and nitrogen sources, pH was eventually adjusted to 7.0.

$(NH4)_2HPO_4$ was used as inorganic nitrogen sources at nitrogen final concentration of 8 mM (limiting concentrations) and 16 mM (no stress). Several carbon sources, namely glycerol, octanoic, lauric, myristic and stearic acids were balanced to achieve a C/N molar ratio 14:1.

PHA fluorescent staining. To monitor PHA production, Nile Red staining has been used. 1 ml of each culture was centrifuged at 6000 *xg* for 10 min and then resuspended in 990 µl of Phosphate-Buffered Saline (PBS, Sigma–Aldrich, Germany) and mixed with 10 µl of Nile Red (Sigma–Aldrich, Germany) stock solution (1 mg/ml in absolute ethanol). Samples were incubated in the dark at 30° or 37° C for 20 min; cells were recovered by centrifugation and resuspended in 100 µl of PBS. 10 µl of samples were put on microscope slides and observed at 63x through epifluorescence microscope (Leica DMRE, Excitation filter BP450-490, Suppression filter LP 515).

Nile Red staining has also been used to monitor production of PHA microspheres and eventual polymer complexes, according to the following procedure:

Nile Red has been mixed to PHA nanoparticles solution at 1% (v/v) concentration. Samples were incubated in the dark at 30 °C for 30 min; then 10 ul of samples were put on microscope slides and observed at 100x through epifluorescence microscope (Leica DMRE, Excitation filter BP450-490, Suppression filter LP 515).

PHA extraction. Dried biomass was dissolved in 10 vol acetone (Jiang *et al*, 2006), and refluxed in Soxhlet extractor at boiling point (56 °C) for 6 h. The lipidic extract was then dried under vacuum by rotavapor until the weight was kept constant.

PHA physico-chemical characterization and co-monomer composition.
200 MHz ^{1}H NMR spectra of the samples were recorded at room temperature in a CDCl3 solution on a Bruker AC 200 spectrometer with a 4 s pulse repetition, a 2000 Hz spectral width, 16K data points and 256 scans accumulation. 1H decoupled 50 MHz ^{13}C NMR spectra were recorded on the same samples with 1.6 s acquisition time, 10,000 Hz spectral width, 32K data points and 30,000 scans accumulation.

Preparation of PHA microspheres. PHA micropheres were prepared by solvent displacement followed by polymer deposition. (Lerouеil-Le Verger *et al,* 1998; Giannavola *et al*, 2003) 13.2 mg of PHA were dissolved in acetone (20 ml). The organic phase was poured into 40 ml of PBS containing 0.5% (w/v) Tween 80, under magnetic stirring, obtaining a milky colloidal suspension. The organic solvent was then evaporated off under high vacuum at 40 °C. Sample was centrifuged at (15000 *xg*) for 1 h at 5 °C and pellets resuspended in water (50 ml). The last step was centrifuged using the same conditions described above. This operation was repeated 3 times. After washing, the microspheres were resuspended in 5 ml of filtered water (0.22 µm Sartorius membrane filters) and characterized for size distribution and surface chemistry.

Physical adsorption of P9b phage clone. 10 µl of P9b phage clone suspension, containing $1 \cdot 10^{11}$ PFU (Plaque Forming Units), were mixed with 990 µl of PBS containing PHA microspheres. P9b, labelled with FITC according to the procedure described in Chapter 3, was left to react with microspheres in rotator (8 rpm) at Room Temperature (RT) for 2h. After incubation, solution was centrifuged at 6000 ×*g* for 5 min. The supernatant was discarded and the pellet resuspended in 500 µL of PBS, then the solution was incubated again for 30 min in the dark on rotator, centrifuged at 6000 ×*g* for 5 min and the pellet was resuspended in 100 µl of PBS. 10 µl of samples were put on microscope slides and observed at 63x through epifluorescence microscope (Leica DMRE, Excitation filter BP450-490, Suppression filter LP 515).

Results and Discussions

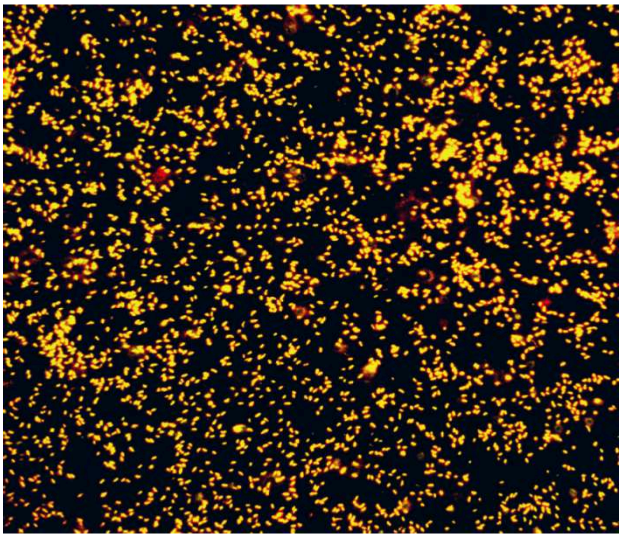

Figure 6.1 PHA granules in *Pseudomonas aeruginosa* Nile Red-stained cells.

Nile Red is a lipophilic stain used to mark intracellular lipid droplets. PHA-containing cells appear yellow-orange so Nile Red staining is used to monitor PHA accumulation over the time.

Table 6.1 shows results of yeilds and thermal properties of PHAs produced under different cultural conditions (carbon sources and metabolic stress).

PHA code	Bacterium	Carbon source	Stress	Tg (°C)	Tm (°C)	ΔH (J/g)	Mw ($x10^{-3}$)	Mn ($x10^{-3}$)	Yield (mg/L)
P35	*P.aeruginosa*	Ottanoic	-Mg	-36	58	11,6	316000	191000	30
P254	*P.mediterranea*	Ottanoic	N (8 mM)	-35	55	9,3	193595	122816	238
P251	*P.aeruginosa*	Ottanoic	N (16mM)	-34	61	24,7	92600	64900	31
P217	*P.aeruginosa*	Lauric	-Mg	-44	53	18,5	237339	119687	47
P233	*P.aeruginosa*	Lauric	-N	-48	54	23,4	77541	40361	44
P212	*P.aeruginosa*	Myristic	-Mg	-41	52	26,3	74260	44789	28
P234	*P.aeruginosa*	Myristic	-N	-43	58	31, 7	107175	63404	358
P235	*P.aeruginosa*	Stearic	-N	-55	44	17,2	117610	70917	351
P214	*P.aeruginosa*	Stearic	N (16mM)	-43	51	23,6	195131	85082	148

Table 6.1 Thermal properties (glass transition temperature (Tg), melting point temperature (Tm) and the enthalpy of fusion (ΔH)), molecular weights (weight average (Mw) and number average (Mn)) and yields of the PHAs obtained by varying the carbon source (octanoic, lauric, myristic and stearic acids) and the eventual imposition of a metabolic stress.

Obtained data suggest a dependence of the polymer chemical-physical properties and yield by stress conditions, regardless of the carbon source used. Limitation or absence of nitrogen is often associated with an increase in temperature Tm and a reduction of Mn. In this last case, an exception to the trend is given by the culture condition with myristic acid. Production yield of PHA is higher when nitrogen concentration is lower.

Table 6.2 relates variations of thermal properties with the monomer compositions obtained by means of ^{13}C-NMR analysis, while **Figure 6.2** shows chemical composition of each monomer.

PHA code	Bacterium	Carbon source	C	O	D	Δ	T	Tm (°C)
P35	*P.aeruginosa*	C8	9	87	4			58
P254	*P.mediterranea*	C8	12	86	2			55
P251	*P.aeruginosa*	C8	5	93	2			61
P217	*P.aeruginosa*	C12	4	52	33	11		53
P233	*P.aeruginosa*	C12	3	49	35	13		54
P212	*P.aeruginosa*	C14	4	53	31	9	3	52
P234	*P.aeruginosa*	C14	4	42	36	13	5	58
P235	*P.aeruginosa*	C18	4	46	35	11	14	44
P214	*P.aeruginosa*	C18	5	36	39	18	2	51

Table 6.2. Monomeric composition (% mol) of PHAs obtained by varying the carbon source (C8, octanoic; C12, lauric; C14, myristic; and C18, stearic acids) and the eventual imposition of a metabolic stress, as determined by means of ^{13}C-NMR analysis.

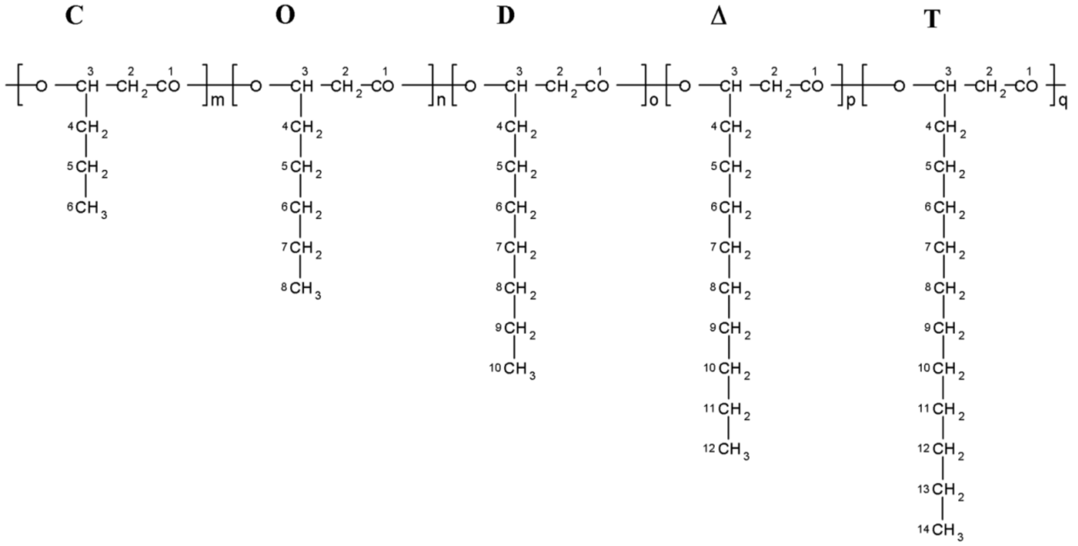

Figure 6.2 Chemical structure of monomer obtained from Pseudomonadaceae, varying the carbon source (octanoic, lauric, myristic and stearic acids) and the eventual imposition of a metabolic stress.

In this case, Tm of a PHA is higher when its composition is more rich in longer chain comonomers.

In order to verify the possible use of these polymers in drug delivery systems, a solvent displacement method for PHA microspheres production has been made. Cupri *et al.* showed results about polymer P254, that has been chosen as PHA model for production of nano-carriers loaded with pranoprofen, a non-steroidal anti-inflammatory drug used in ophthalmology. Obtained nanoparticles, with mean size 160-200 nm and a net negative Zeta potential (-17 mV), exhibited high encapsulation efficiency values for the drug and the ability to release the incorporated drug with a constant evolution up to 12 h. Due to their size, these carriers can be easily sterilized by membrane filtration with porosity of 0.22 μm.

An additional type of polymer has been obtained by fermentation process using another strain of *P. mediterranea,* namely 9.1*,* fed with glycerol.
This strain has been chosen for its high versatility to degrade different carbon sources, such as pure glycerol and myristic, erucic, stearic, linoleic and palmitic acids (**Table 6.3**).

Carbon source	**Biomass yield (mg/L)**	**PHA yield (mg/L)**
Pure glycerol (1% w/v)	1560	320
Miristic acid (10mM)	820	90
Erucic acid (10mM)	2050	130
Stearic acid (10mM)	1410	130
Linoleic acid (10mM)	980	>1
Palmitic acid (10mM)	930	90
Crude glycerol (1% w/v)	1810	570

Table 6.3 PHAs yields obtained using *P. mediterranea* 9.1 fed with different carbon sources. Data have been published in Chemical Engineering Transactions (Nicolò *et al*, 2015)

All fermentation conditions were carried out in limiting concentrations of nitrogen for a period of 72h. Data indicate a very high yield of product when glycerol was used as the only carbon source (pure glycerol) or in co-presence with other carbon sources (crude glycerol). PHA physico-chemical characterization and co-monomer composition has been carried out with the same methods described above. Particularly, the properties of the polymer produced using pure glycerol as carbon source are very interesting (**Table 6.4**).

Bacterium	**Carbon source**	**C**	**O**	**D**	**Δ**	**Δ: $1\Delta^6$**	**Δ: $1\Delta^5$**	**Tm (°C)**	**Tg (°C)**	**ΔH (J/g)**	**Mw ($x10^{-3}$)**
P.*mediterranea 9.1*	Glycerol	0	10.8	66.1	7.2	1.4	14.4	40.6	-46.6	9,4	≈60000

Table 6.1 Thermal properties (glass transition temperature (Tg), melting point temperature (Tm) and the enthalpy of fusion (ΔH)), molecular weights (weight average (Mw) and number average (Mn)) and yields of the PHAs obtained by varying the carbon source (octanoic, lauric, myristic and stearic acids) and the eventual imposition of a metabolic stress.

In fact, similarly to others mcl-PHAs produced by fatty acids, the presence in the copolymer of medium chains length monomers (C8, C10 and C12) keeps unchanged physico-chemical properties. Moreover, the unsaturated side chains, containing double bonds, offer the additional potential for improving the properties of the PHAs or extending their application.

In this regard, it has been tried a functionalization protocol of microspheres of PHA with phage P9B for a drug targeting systems.
On the basis of such results, the same solvent displacement method previously used for nanoparticles production has been carried out with the polymer derived by glycerol. **Figure 6.3** shows PHA microspheres stained with Nile Red.

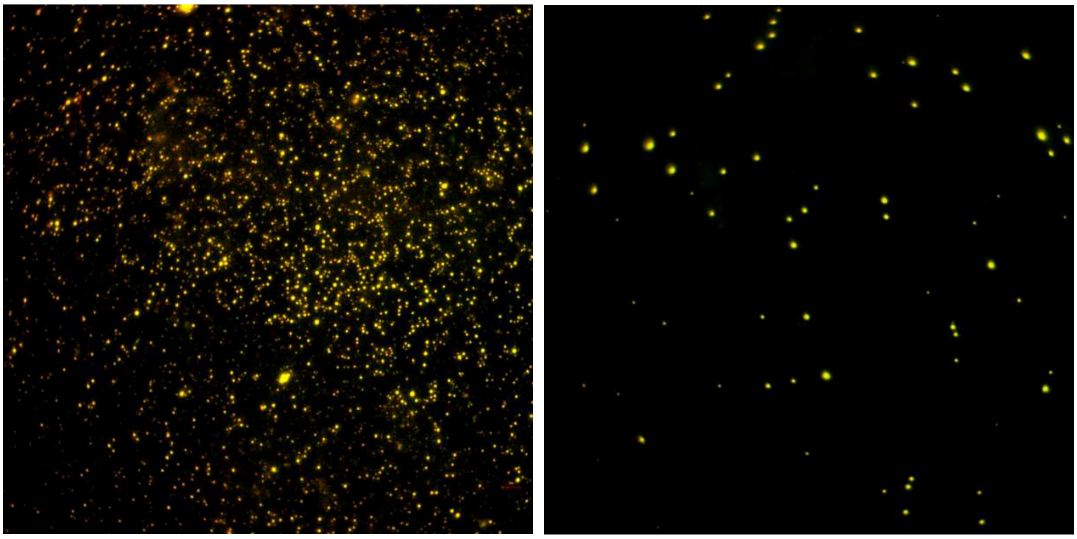

Figure 6.3 PHA microspheres stained with Nile Red.

Obtained microspheres exhibited an average size of 1-2 µm, which were compatible with a good and homogeneous distribution of phages on the microspheres surface. Therefore, a preliminary test of physical adsorption of FITC-labelled P9b phage clone was carried out. FITC-labelled P9b-functionalized PHA microspheres have been successfully obtained and observed under epifluorescence microscope (**Figure 6.4**).

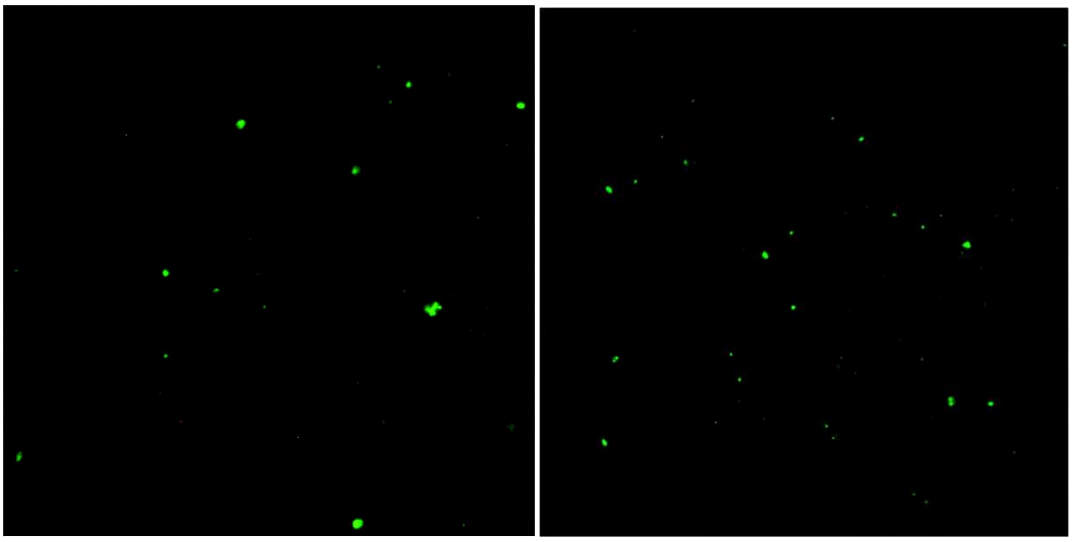

Figure 6.4 PHA microspheres functionalized with P9b FITC-labelled clone.

The presence of a green bright fluorescence indicates that P9b FITC-labelled clone was physically adsorbed on PHA microspheres surface.

These preliminary data are very promising for the development of an innovative drug targeting system, in which PHA is the drug carrier and phage clones are the targeting agents.

PHAs have excellent properties of biocompatibility and biodegradability, that can be modulated in several ways. The high variability of PHAs monomer composition, that can be appropriately designed, will allow the identification of other polymers potentially suitable as drug carriers. Moreover, phage display is a technique that can be easily used to obtain new peptides for the selective and specific recognition of a desired molecular or cellular target.

However, further studies are needed to explore the possibility of covalently binding both phage clones and drug to PHA microspheres.

Acknowledgements

This activity was partially funded by Italian Ministry of Education, University and Research (MIUR) by means of the national Program PON R&C 2007–2013, project project HIPPOCRATES – Development of Micro and Nano-Technologies and Advanced Systems for Human Health (PON02_00355_29641931) and project POLYBIOPLAST- Technologies and processes for the production of diversely functionalised sheets based on microbial biopolymers and biosurfactants- (PON01_01377).

This activity was carried out in collaboration with:

Professor A. Ballistreri Department of Drug Sciences, University of Catania, Italy.

Doctor G. Impallomeni Institute for Polymers, Composites and Biomaterials-CNR Catania, Italy.

Professor R. Pignatello NANO-i-Research Centre on Ocular Nanotechnology, Department of Drug Sciences, University of Catania, Italy.

Professor A. Catara Science and Technology Park of Sicily, Catania, Italy.

Bibliography

Byrom D. Polymer synthesis by microorganisms: technology and economics. 1987 Trends in Biotechnology 5, 246-50.

Brannon-Peppas L, Blanchette JO. Nanoparticle and targeted systems for cancer therapy. 2004. Adv Drug Delivery Rev. 56, 1649.

Cammas S, Bear MM, Moine L, Escalup R, Ponchel G, Kataoka K, Guérin P. Polymers of malic acid and 3-alkylmalic acid as synthetic PHAs in the design of biocompatible hydrolyzable devices. 1999. International Journal of Biological Macromolecules, 25, 273-82, 1999.

Duncan R. The dawning era of polymer therapeutics. 2003. Nat. Rev. Drug Discovery 2, 347-60

Giannavola C, Bucolo C, Maltese A, Paolino D, Randelli MA, Puglisi G, Lee VH, Fresta M. Influence of preparation conditions on acyclovir -loaded poly-d, l-lactic acid nanospheres and effect of PEG coating on ocular drug bioavailability. 2003. Pharm. Res. 20, 584-90

Goren D, Horowitz AT, Zalipsky S, Woodle MC, Yarden Y, Gabizon A. Targeting of stealth liposomes to erbB-2 (Her/2) receptor: in vitro and in vivo studies. 1996. Br. J. Cancer, 74, 1749-56.

Gradishar WJ, Albumin-bound paclitaxel: a next-generation taxane. 2006. Expert Opin. Pharmacother. 7, 1041-53

Harris JM, Chess RB. Effect of pegylation on pharmaceuticals. 2003. Nat. Rev.Drug Discovery 2, 214-21.

Jiang X, Ramsay JA, Ramsay BA. Acetone extraction of mcl-PHA from Pseudomonas putida KT2440. 2006. J. Microb. Meth. 67, 212-19.

Keshavarz T, Roy I. Polyhydroxyalkanoates: bioplastics with a green agenda. 2010 Current Opinion in Microbiology. 13, 321–26.

Leroueil-Le Verger M, Fluckiger L, Kim YI, Hoffman M, Maincent P. Preparation and characterization of nanoparticles containing an antihypertensive agent. 1998. Eur J Pharm Biopharm. 46,137-43

Nicolò M, Franco D, Camarda V, Gullace R, Rizzo MG, Fragala` M, Licciardello, Catara AF, Guglielmino SPP. Integrated microbial process for bioconversion of crude glycerol from biodiesel into biosurfactants and PHAs. 2014. Chem Eng Trans 38,187–92.

Park JW. Liposome-based drug delivery in breast cancer treatment. 2002 Breast Cancer Res. 4, 95.

Rizzo MG, Chines V, Franco D, Nicolò MS, Guglielmino SP. The role of glutamine in Pseudomonas mediterranea in biotechnological processes. 2016. N Biotechnol. S1871-6784(16)30009-7.

Sakamoto J, Annapragada A, Decuzzi P, Ferrari M. Antibiological barrier nanovector technology for cancer applications. 2007. Expert Opin. Drug Delivery 4, 359-69

Steinbuchel A, Fuchtenbusch B. Bacterial and other biological systems for polyester production. 1998Trends in Biotechnology 16, 419–27.

Steinbuchel A, Schlegel HG. Physiology and molecular genetics of poly(β-hydroxy-alkanoic acid) synthesis in Alcaligenes eutrophus. 1991. Molecular Microbiology 5, 535–42.

SUMMARY AND PERSPECTIVES

Theranostic nanomedicine is emerging as a promising tool to generate new conceptual and technical solutions which allow the coupling of therapy and diagnostic as one-step systems.

Micro- and nano-technologies and -materials, if adequately assembled, may perform both imaging and therapeutic functions. The resulting micro- and nanosystems, suitable for diagnosis, drug delivery and monitoring of therapeutic response, may play a pivotal role in the emerging era of personalized medicine, and several research efforts, by both private investors and public institutions, are actually addressed toward this goal.

The recent advances of nanotechnology have gratly increased the possibility to draw diagnosis and therapy closer.

On the other hand, several nanomaterials, which are imaging agents, can be implemented with therapeutic functions, so evolving to theranostic agents.

As an innovative contribution to theranostic nanomedicine, phage-display has a very broad potential for diagnosis and treatment of diseases, although many approaches have to be deeply investigated for its *in vivo* application.

In this work, I have provided an overview on some potential implications of M13 engineered clones in the area of nanomedical research and theranostics.

The technical combinations here presented of phage clones with fluorchromes, beads, noble metal nanoparticles, PHA microspheres demonstrate the importance of intersections among different fields of theoretical and applied science and the necessity of a common language among different professionals and research teams.

On this basis, phage clones can been employed as:

- Target agents for cell and/or molecular imaging, by Fluorescence microscopy;
- Target agents in immune capture system for pathogen detection by Fluorescence microscopy, Raman spectroscopy and PCR assay;
- Target agents and noble metal nanoparticles vectors in networks for cell and/or molecular imaging by Surface-enhanced Raman scattering and for responsive systems against diseases.
- Target agent for PHA-based drug targeting system.

However, the presented work needs further studies to:

- Extend the range of materials and approaches;
- Extend the number of targets that can be recognized;
- Extend the number of pathologies to be studied for early diagnosis and targeted therapy;
- Develop a series of trials for evaluating the *in vivo* efficiency of the proposed micro- and nano-platforms.